UNIVERSITY OF CALIFORNIA
RIVERSIDE

A Study of Singlet Fission and its Mechanism Within Crystalline Tetracene

A Dissertation submitted in partial satisfaction
of the requirements for the degree of

Doctor of Philosophy

in

Chemistry

by

Jonathan James Burdett

December 2012

Dissertation Committee:
Dr. Christopher J. Bardeen, Chairperson
Dr. Gregory Beran
Dr. Francisco Zaera

The Dissertation of Jonathan James Burdett is approved:

_____

_____

_____

Committee Chairperson

University of California, Riverside

ACKNOWLEDGEMENTS

No one goes through life alone, and graduate school is no exception. Without the encouragement and support of my wife, friends, family, and my advisor, I would not have succeeded or flourished in graduate school.

I would like to convey my deepest thanks to my advisor, Dr. Christopher Bardeen, for the direction he has given to me in my graduate career and the patience he has shown as I continue to learn. He has been a great mentor throughout graduate school, and I look forward to a continued relationship in the future.

I cannot talk about success without thinking of my parents. They taught me to always do my best, to never leave a job half-finished, and to strive for greater learning. Thank you for all that you have done to make me into who I am today.

Without labmates, the hours spent in lab can be mind-numbing. I'd like to thank Robert Dillon especially, for keeping things interesting, as well as for all the help in the lab. Many thanks as well to all my other labmates in the Bardeen group.

Last, but assuredly not least, I would like to thank Allison, my lovely wife, for her patience and understanding as I worked on my degree, and for always being willing to work with me when I need to meet deadlines. Without you, I'd be stuck in the lab and forgetting about all that life has to offer.

ABSTRACT OF THE DISSERTATION

A Study of Singlet Fission and its Mechanism
Within Crystalline Tetracene

by

Jonathan James Burdett

Doctor of Philosophy, Graduate Program in Chemistry
University of California, Riverside, December 2012
Dr. Christopher J. Bardeen, Chairperson

Singlet fission (SF) is a process in organic molecules that is able to create two triplet excitons from one initially excited singlet exciton. Beyond its interest as a unique photophysical process, SF is also worth studying due to its capability to enhance the overall efficiencies of photovoltaic cells beyond the Shockley-Queisser limit. In order to take advantage of this process, a more thorough understanding of how it occurs and how it can be enhanced is needed. Specifically, this work begins to answer some of the larger questions about SF within tetracene. SF was first observed in anthracene in 1965, and has since been found to occur in larger polyacenes and other conjugated organic molecules. This study focuses on crystalline tetracene for several reasons, most notably for its favorable energy levels for the study of the interaction between the singlet and triplet excitons, greater chemical stability, and large body of previous work. In this work, the electronic states of tetracene are characterized with time resolved photoluminescence

and transient absorption spectroscopies in order to determine the rate and mechanism of SF within crystalline tetracene, which have not been conclusively shown in prior studies. Using spectroscopy measurements, this work has determined that SF is occurring within crystalline tetracene with a formation time of 80±3 ps, which leads to a triplet yield of 200%. Additionally, the study of the temperature dependence of crystalline tetracene photoluminescence has shown that the fission of a singlet into two triplets may not be thermally activated, a finding which is unexpected based on previous work. Furthermore, observation of quantum beats within the delayed fluorescence of single crystals of tetracene strongly suggests that the singlet fissions directly into two triplets rather than proceeding through a charge-transfer intermediate. Overall, this work has shown that SF occurs with a high efficiency within tetracene, and that tetracene is a viable candidate for use as a SF sensitizer within a photovoltaic cell.

TABLE OF CONTENTS

LIST OF FIGURES

Page

CHAPTER 1

Introduction

1.1 Improving photovoltaic efficiencies

While fossil fuels are not in danger of running out in the immediate future, it is important to explore other avenues of more ecologically friendly energy sources. One plentiful source of energy is the sun, which supplies $3x10^{24}$ J/yr of energy to the earth, which is about 4 orders of magnitude more energy than the world uses in a year.[1] Harnessing this energy with photovoltaic cells has been a prolific research topic for more than 60 years,[2] but the application of this research has found a new urgency with the public awareness of global warming.

One of the largest problems with single junction solar cells, i.e. those with only one active layer, is a relatively low cap to their efficiencies, which was explained by the theoretical work of Shockley and Queisser.[3] In 1961, their calculations proved that the maximum efficiency of any single junction photovoltaic cell is only ~31% because the entire solar spectrum can not be efficiently exploited in order to generate electricity. Photons with energy that is equal to the band gap of the photovoltaic cell can be 100% efficient, but photons with energy less than the band gap are not absorbed at all while photons with energy greater than the band gap will lose any excess energy over the band gap as heat into the cell due to the fast relaxation time of higher energy states. From their work, they found that the maximum efficiency of the single junction cell requires a band gap between 1.0 and 1.5 eV.

While most of the photovoltaic cells in commercial use today use crystalline silicon as the active material due to its band gap at 1.1 eV, research continues to search for more efficient ways to harness solar energy due to the high cost associated with processing inorganic molecules.[4] One such method is by making use of organic molecules, polymers, and crystals as photoactive materials rather than crystalline inorganics. Organic molecules bring several advantages over inorganic molecules, such as lower processing cost and greater tunability through chemical modification.[4,5] Specifically, the larger polyacenes (anthracene, tetracene, pentacene) have long served as prototypical conjugated organic semiconductors, and coherent band-like charge transport has long been known to exist in highly purified polyacene crystals.[6] The combination of facile charge transport and exciton diffusion in the larger polyacenes suggests that these materials have the potential to generate high photocurrents. These advantages do have a downside, which is found in the lower photovoltaic efficiencies of organics in comparison to inorganic semiconductors.

In the pursuit of higher efficiency photovoltaic cells, new photophysical phenomena are being investigated in both inorganic and organic materials. One of the most promising ways to surpass the Shockley-Quiesser limit for single junction photovoltaic cells is to convert the excess energy in above-the-gap photons into more than one electron-hole pair, which is also known as downconversion.[7,8] Multiple exciton generation in inorganic semiconductor nanocrystals is one example of how new types of materials could make this possible.[9,10] Although the mechanism and overall efficiency of this process is still debated, recent results indicate that it can lead to photocurrent yields

in excess of 100%.[11,12] In organic molecular solids an analogous phenomenon called singlet fission (SF) has been known for almost 50 years.[13,14] Unlike intersystem crossing, where a singlet state is converted into one triplet state via a spin flip, SF is a 4-electron, spin-allowed process whereby an initially created singlet exciton spontaneously splits into a pair of triplet excitons. Conservation of energy requires that the energy of the triplet must be half that of the singlet, but theoretical surveys predict that large numbers of conjugated molecules could fulfill this requirement.[5] Heterojunction solar cells based on tetracene and pentacene have already displayed reasonably high (~2%) solar energy conversion efficiencies,[15-17] which could be due to the existence of SF within these molecules, although this has not been proven.

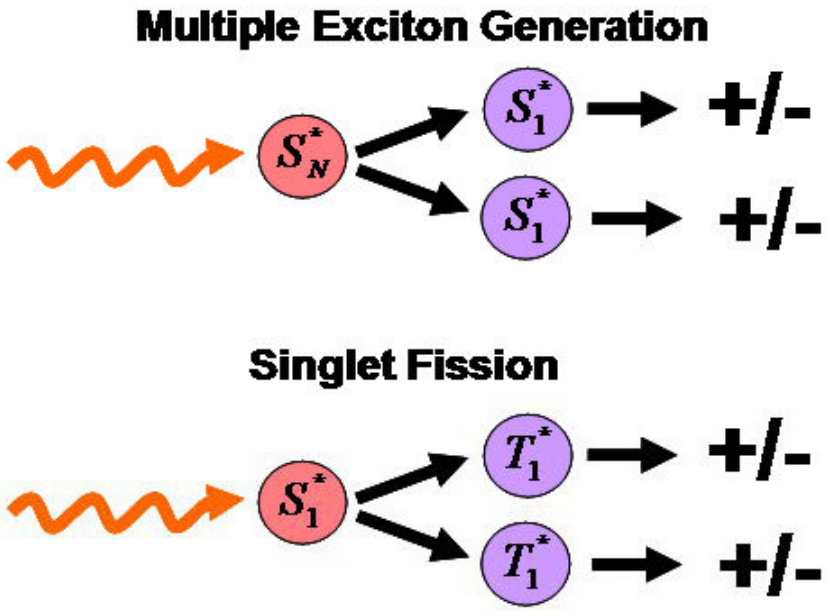

Figure 1.1. The top portion of the figure illustrates how MEG is capable of generating multiple excitons from one photon, where the created excitons are still singlet excitons. This is markedly different from SF's method of generating multiple excitons from one photon, which creates triplet excitons from the initially excited state.

1.2 Singlet fission in the literature

Originally observed in anthracene crystals in 1965,[13] SF has been postulated to play an important role in the excited state dynamics of tetracene[18] and pentacene[19], both of which fulfill the energetic requirement for efficient SF that the energy of the relaxed singlet state $E(S_1)$ must be at least twice that of the triplet energy $E(T_1)$, i.e. $E(S_1) \geq 2E(T_1)$[5]. In their work on anthracene single crystals, Singh et al. observed two different photoluminescence decay rates depending on the excitation wavelength that they used.[13] The standard photoluminescence they obtained by exciting the singlet state with 347 nm they labeled as the "prompt" photoluminescence, and the signal observed with excitation of the triplets with 678 nm they labeled as the "delayed" photoluminescence. They attributed the delayed fluorescence to triplet fusion in the crystals, which had already been established in the literature for anthracene,[20] but the mechanism for the large number of triplets observed in anthracene crystals was not known at the time. From their photoluminescence measurements, Singh et al.[13] postulated that the formation of triplets in anthracene could be due to the reverse process of triplet triplet annihilation to form a singlet, but they could not rule out other possible mechanisms for the temperature dependence of the delayed fluorescence. In 1967, Johnson et al.[21] studied the magnetic field dependence of the delayed fluorescence in anthracene crystals in order to confirm that this photoluminescence was due to the recombination of two triplets to form a singlet excited state. Swenberg and Stacy[18] also proposed SF as a reason for the temperature dependence of this prompt and delayed fluorescence in crystalline tetracene and concluded that SF is a thermally activated

process in tetracene based on the temperature dependent changes in the quantum yield. From calculations using a simple model and values from the literature, they estimate that the rate of SF as ~$10^{10} - 10^{12}$ s^{-1}, with the possibility of a charge–transfer intermediate in this process. In 1969, Merrifield et al.[22] concluded that singlet fission occurs within tetracene crystals based on the magnetic field dependence they observed in the photoluminescence intensity, and they used the following model to describe this dependence in crystalline tetracene:

$$S_1 + S_0 \underset{k_2}{\overset{k_{-2}}{\rightleftharpoons}} (T_1T_1) \underset{k_1}{\overset{k_{-1}}{\rightleftharpoons}} T_1 + T_1 \qquad (1.1)$$

where (T_1T_1) is a pair of interacting triplets and S_0, S_1, and T_1 are molecules in their ground, excited singlet, and triplet states, respectively, while $k_{\#}$ represents the rate to and from these states. In order to conserve spin, only triplet states with overall singlet character can annihilate to form a singlet excited state. This equation can be simplified to the following:

$$S_1 + S_0 \underset{\gamma}{\overset{\gamma'}{\rightleftharpoons}} T_1 + T_1 \qquad (1.2)$$

where γ and γ' are the overall rate constants for the triplet recombination and SF, respectively. Application of a magnetic field affects the triplet state energies since they are paramagnetic, and those energy level changes affect which triplet states are capable of annihilating to form a singlet and thus changes the rate of fission. Geacintov et al.[23] built on the work of Merrifield and conducted further experiments in to study the magnetic field effects on tetracene photoluminescence intensity, combining the magnetic field with

the polarization and temperature dependence of the photoluminescence intensity. They conclude that SF is occurring in tetracene and is correctly modeled by Merrifield's model due to the maxima in the photoluminescence intensity observed at polarizations where there is degeneracy within the triplets with singlet character. In a following paper from the same group, Pope et al.[23] calculated the rate of SF in tetracene to be $5x10^9$ s^{-1}, but they did not temporally and spectrally resolve their photoluminescence.

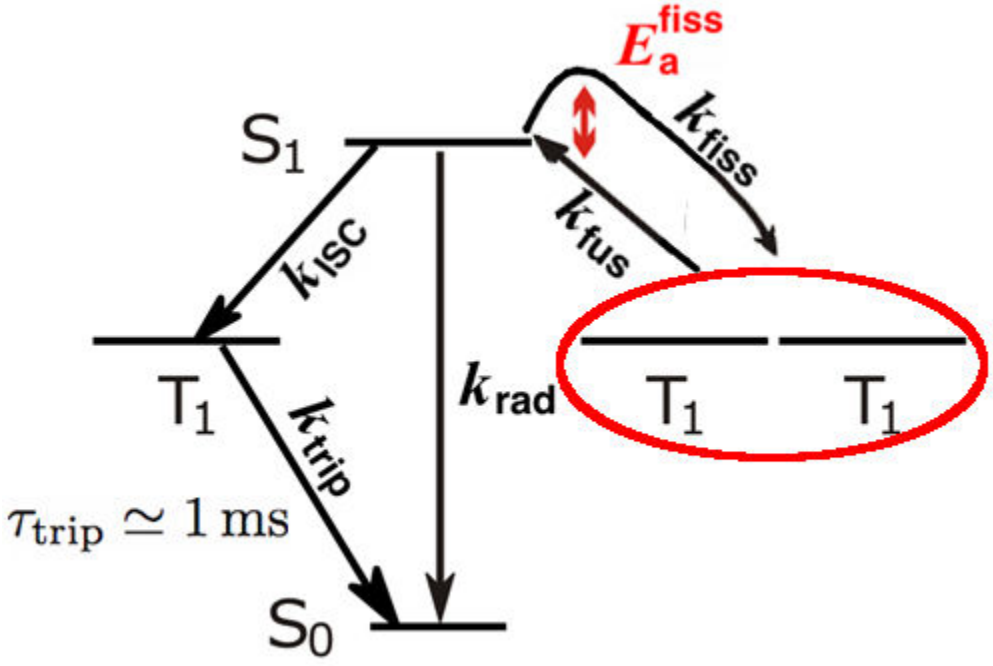

Figure 1.2 Typical mechanism that has been used to describe SF in crystalline tetracene, specifically illustrating the proposed energy barrier to SF.

Although there has been significant work done on the subject of SF in crystalline tetracene, there are some experimental problems with the previous work, as well as unanswered questions. Initial investigations of SF in tetracene have taken place in single crystals of varying thicknesses ranging from 10 μm to 1.5 mm. However, Hofberger et al. have since found that thicker evaporated films lead to changes in the absorption

spectrum and self-absorption, which can also change the observed kinetics.[24] Another problem is that any direct measurement of the photoluminescence rates in crystalline tetracene did not separate the contributions of the delayed fluorescence from the prompt fluorescence. To get an idea of rates involved in SF in tetracene, Pope et al. instead calculated these rates for SF based on steady state measurements. Additionally, measurements of the temperature dependence of the photoluminescence intensity were used to justify the conclusion that SF is a thermally activated process, but these measurements are unable to verify this conclusion since they do not completely separate the photoluminescence from the initially excited singlet from the photoluminescence due to triplet recombination. Instead, simultaneously resolving the photoluminescence in time and wavelength is required to accurately measure the changes in the prompt and delayed fluorescence due to temperature changes and applied magnetic fields. Furthermore, increased intensity at low temperatures in the photoluminescence of the singlet excitation in comparison to the photoluminescence of the triplet excitation does not prove that SF is an activated process since that increased photoluminescence could be due to less singlet fission or less delayed fluorescence. Due to these experimental problems, the rate of SF has not been accurately determined. Another problem is that there is no direct measurement of population transfer from the singlet to the triplet, although there have been several indirect measurements. This leads to the conflict in the literature over whether there is a charge-transfer intermediate in SF or if SF proceeds directly to the two triplets.

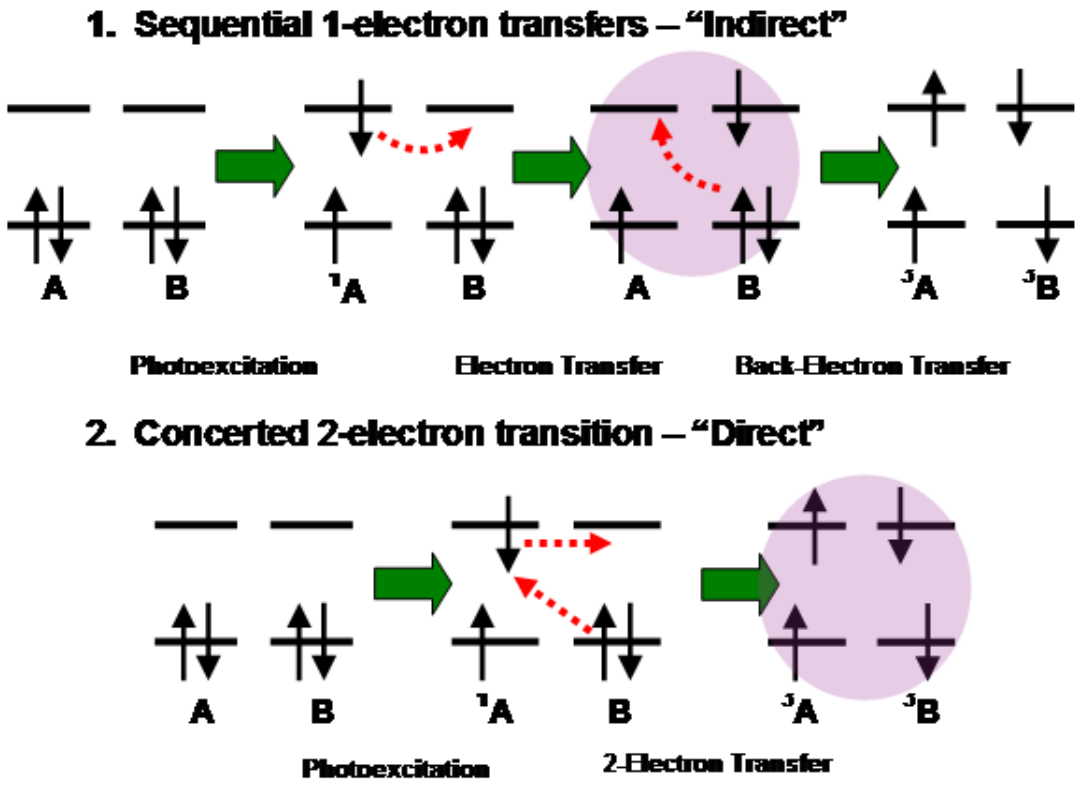

Figure 1.3 The indirect mechanism takes place through sequential transfer of electrons from each excitation site, creating a charge transfer intermediate before the final two triplets are created. The direct mechanism has a simultaneous transfer of electrons to form the two triplet states.

The study of SF has recently acquired a new urgency in the context of solar energy because this type of 1→2 multiple exciton generation scheme has the potential to raise the efficiency of a single junction solar cell by as much as 40%, assuming that the triplet excitons can be efficiently converted into electron-hole pairs.[7,8] Because of this interest in new photophysical properties for enhancing photovoltaic efficiencies, there has been an increased research focus on SF and how it occurs. However, the technological development of these materials seems to have outstripped the fundamental understanding

of their electronic states and how dynamic processes like relaxation and transport occur. For example, solid pentacene has recently been the subject of several investigations of SF with conflicting ideas of the photophysics in this system.[7, 25-26] Recent experiments on pentacene-based photodetectors suggest that SF enhances carrier generation in this molecular solid.[25] while transient absorption (TA) experiments[27-28] and theoretical work[29] have cast doubt on whether the initially created singlet exciton actually dissociates into two triplets in pentacene. Alternative pathways include the formation of charge-transfer excitons or bound triplet pair states after subpicosecond relaxation from the initially excited singlet state. Recent theoretical work is clarifying the conditions under which SF may be optimized[14], and experimental work in our group has demonstrated that SF can occur in covalent tetracene dimmers while other groups have investigated a variety of other organic materials.[14,30-38] Additionally, theoretical work has also clarified the distinction between the "direct" mechanism of SF, where the multiple exciton state is produced in a single step, and the "indirect" mechanism where sequential electron transfer events require the involvement of an intermediate charge-transfer state.[14,39,40] The difference between these two mechanisms is illustrated in Figure 1.3. At this point, it is an open question as to which mechanism is actually operative in a given molecular system. In order to design new materials that can lead to practical improvements in photovoltaic efficiencies, a better quantitative understanding of this phenomenon is needed, which is the goal of this work.

1.3 Furthering the understanding of singlet fission within tetracene

In order to optimize the SF process, an improved physical understanding of the process and its dependence on molecular structure is required. In tetracene specifically, the rate of SF and the mechanism through which SF occurs are two of the major questions to understanding SF in this system. This dissertation focuses on understanding the dynamics of SF in tetracene in order to precisely measure the rate of SF in tetracene and elucidate the mechanism through which SF occurs. Recent work in our group has centered on gaining a quantitative understanding of the delocalized singlet excitons in both anthracene and tetracene using time-resolved photoluminescence spectroscopy.[41,42] Crystalline tetracene has the advantage that multiple techniques have been used to study triplet formation and relaxation, including magnetic field effects, and electron spin resonance. [22,23,43-47] While tetracene is similar to pentacene in terms of its crystal structure and its solid-state absorption properties, tetracene has greater chemical stability and a large body of previous spectroscopic studies. Tetracene's energy levels are also favorable for studying the interaction of singlet and triplet excitons. In pentacene, $E(S_1)>2E(T_1)$ and once the triplets are formed, it is energetically impossible for them to recombine at a later time into a singlet state. In tetracene, $E(S_1)\cong 2E(T_1)$ which permits both singlet and triplet dynamics to be monitored via prompt and delayed fluorescence signals, respectively. The ability to easily detect both species via photoluminescence has allowed the extensive characterization of SF in crystalline tetracene, and the dependence of singlet versus triplet yield on magnetic field orientation has provided strong evidence that SF plays a dominant role in this system. [22,23,48,49] The established nature of SF in this

system makes tetracene an interesting system both for fundamental photophysical studies and as a potential SF material for photovoltaic applications.

Several different experimental methods are used to answer these questions about SF within crystalline tetracene, including various microscopies and steady state and time resolved spectroscopies. The specifics of the sample preparation, experimental methods, calculations, and simulations are described in detail Chapter 2. Solid samples are made using various techniques to explore how the preparation affects the physical and electronic characteristics of the samples. The physical structure and characteristics of the polycrystalline films are investigated with atomic force microscopy and XRD, while the single crystals are studied with polarizing microscopy. The electronic states of tetracene are characterized with time resolved photoluminescence and transient absorption spectroscopies. Simulations of the electronic energy levels and transition rates are conducted with Matlab, while data is fit using the analysis software Origin and FAST.

In Chapter 3, we determine the rate and efficiency of singlet fission within polycrystalline tetracene. In order to verify the effect of SF on polycrystalline tetracene, tetracene monomers in solution are first examined with picosecond photoluminescence and femtosecond TA. The femtosecond TA of the monomer in solution shows the ground state and bleach emissions that match with the 4.2 ns lifetime of the singlet measured by photoluminescence, which is consistent with the literature. However, there are also several unexpected excited state absorptions that overlap with the bleach and emission transitions that are occurring on the same timescale as the excited singlet, which may complicate the observation of the population transfer from the singlet to the triplet

manifold. Before turning to spectroscopy of the solid, we first confirm the expected triplet absorption with TA by increasing the probe beam path length to longer delays in order to minimize the excited singlet absorptions that we are not interested in. We observe a biexponential decay in the room temperature photoluminescence of the polycrystalline films, which is consistent with earlier models that take into account exciton-exciton annihilation and exciton fission, but we observe a reduced delayed fluorescence lifetime, ranging from 20-100 ns as opposed to 5 μs or longer in single crystals. Additionally, the solid tetracene photoluminescence spectrum is very different than the tetracene monomer due delocalization of the excited state leading to the superradiance of the $S_0 \rightarrow S_1$ transition of solid tetracene. Beyond the photoluminescence, the superradiance also affects the transient absorption spectrum of tetracene, so that the excited state absorptions which were dominant in the monomer are no longer larger the principal feature in the TA. In addition to the change in the TA due to superradiance, the kinetics of the stimulated emission in the TA no longer agree with the photoluminescence as they did in the monomer, while the triplet absorption is not observed at all. Our first explanation for this difference in the kinetics is that the transient absorption is observing the initially excited state while the photoluminescence is due to a different defect state. However, a more careful study with lower laser fluences as conducted in Chapter 4 has shown this difference to be due to exciton exciton annihilation in the broadband transient absorption. Further investigation into the crystal structure has also explained that the orientation of the triplet transition dipole moment is such that it cannot efficiently absorb the incident polarized light. This polarization effect in addition to the superradiance of

the singlet makes direct observation of the triplet via transient absorption problematic, which is consistent with the problems in clear observation and assignment of the triplet transition in the polyacenes.[19,26-28,50-52] In order to get around this problem, long delay transient absorption experiments monitoring the ground state bleach are conducted to verify that there are molecules not in the ground state, which we can then infer to be triplets based off of previous magnetic field studies confirming the presence of triplets in tetracene. [22,23,43] This chapter begins the work of combining photoluminescence and TA experiments with theoretical modeling in order to determine the mechanism and rate of SF in tetracene.

Building on the work of the previous chapter, Chapter 4 contains a closer investigation of the power dependence of the femtosecond TA in conjunction with picosecond photoluminescence, to verify whether exciton-exciton annihilation plays any role in the discrepancy between the broadband TA kinetics of 9.2 ps with the 80 ps kinetics observed in photoluminescence. Additionally, Chapter 4 also contains a study of the temperature dependence of the photoluminescence, where the SF relaxation channel is believed to become thermally inaccessible in tetracene. While the previous work compared the TA and photoluminescence, there was a discrepancy between the broadband transient absorption and what was observed in photoluminescence experiments seen previously, which could be due to the difference in the fluence of ~2 orders of magnitude used between the two experiments. In order to verify that this discrepancy is related to the fluence difference, high-sensitivity single channel transient absorption experiments are conducted, which allow us to compare the transient

absorption dynamics to the photoluminescence dynamics measured at identical laser fluences. Once the excitation densities are less than $2x10^{17}$ cm^{-3}, the decay from the stimulated emission in transient absorption matches with that obtained from the photoluminescence. From the power dependence of the TA and photoluminescence experiments, the rate of singlet exciton-exciton annihilation, $k_{ee,}$ is calculated to be $1x10^{-8}$ cm^3 s^{-1}, which is between the values found in the literature.[53,54] Since both experiments now agree on the rate of fission, the photoluminescent defect state is no longer needed to describe the room temperature photophysics of tetracene. While the work of the previous chapter does imply that SF is active in tetracene, there is still no direct confirmation that the faster decay of photoluminescence in the solid is due to singlet fission. To confirm that the singlet decay is due to singlet fission, the photoluminescence was measured at three temperatures: 298 K, 77 K, and 4 K. The 80 ps lifetime was observed at all three temperatures, but the delayed fluorescence, which indicated recombination of triplets to form a singlet, did not occur at the lower temperatures. Instead, as the temperature is decreased, the initial photoluminescence spectrum is replaced by emission from multiple low energy species. This data indicates that the traditional picture of SF in tetracene, which postulates that the SF channel effectively turns off at ~150 K, is not accurate. Additionally, as the wavelength of excitation was changed from 400 to 510 nm along with the temperature, the temperature dependence did not change in the photoluminescence, further suggesting that there is not an energy barrier for SF. The lack of delayed fluorescence also indicated that there is an intermediate state involved in SF

and in the formation of free triplets, which is consistent with the mechanism described in the literature to explain the magnetic field effects on the photoluminescence of tetracene.

Up to this point, the question of the mechanism of SF in tetracene has still not been resolved since there has been no direct measurement of the triplet appearance in tetracene. That is not to say that there is no evidence to help discern which mechanism more accurately describes SF in tetracene, which is the focus of Chapter 5. The work of Chabr et al.[55,56] on the photoluminescence of single crystals of tetracene gives an abundance of information by using photoluminescence experiments to monitoring the dynamics of the triplets. The photoluminescence signals in their experiments demonstrated direct evidence of the formation of triplet pairs in tetracene when they discerned quantum beats in the delayed fluorescence with frequencies that correspond to the zero-field splittings of the triplet pairs. These quantum beats provide confirmation of the direct mechanism, since the correlation between the zero field splittings and the beat frequencies show that the SF process creates triplet pair superposition states. While they observed these quantum beats, no other group has corroborated their work, and it was largely ignored by the field. In Chapter 5, we revisit and expand on the experiments of Chabr et al.[55,56] While they observed quantum beats, they focused on the changes in the samples' photoluminescence in high magnetic fields, but their relatively low signal-to-noise ratio made it difficult to claim anything more than the observation of the quantum beats and the frequency change in the magnetic fields. In order to fully understand what is occurring in the single crystals, we study the effects of sample morphology, excitation wavelength, and temperature upon the quantum beats and develop a new model using

density matrix theory to describe the fission of the singlet as well as the damping of the beats. Our photoluminescence experiments resolve three quantum beat frequencies of 1.06 ± 0.05, 1.82 ± 0.05, and 2.92 ± 0.06 GHz which are damped within 20 ns at room temperature. These quantum beats appear to be a general phenomenon within tetracene, existing within both single crystal and polycrystalline film samples, and are not due to any electronic coherence between the singlet and triplet pair states. While there is no coherence between the singlet and triplet pair states in our model, we assume that there is a direct coupling between the initially excited singlet and the triplet which is able to create a coherent superposition of three zero-field triplet pair states ($|xx\rangle$, $|yy\rangle$ and $|zz\rangle$) via an impulsive population transfer. This superposition of the three triplet pair states is what creates the three frequencies observed in the quantum beats. The damping of the quantum beats is attributed to two different mechanisms within the sample: pure dephasing between the triplet pair states in addition to the population exchange between the singlet and triplet pairs. As the temperature is lowered, the quantum beats disappear, similar to the delayed fluorescence as described in Chapter 4. A model is developed that assumes a direct coupling of the initially excited singlet exciton to the triplet pair manifold. There is no electronic coherence between the singlet and triplet pair states, but the rapid singlet decay time of ~200 ps in solution-grown single crystals provides the impulsive population transfer necessary to create a coherent superposition of three zero-field triplet pair states $|xx\rangle$, $|yy\rangle$ and $|zz\rangle$ with overall singlet character. This superposition of the three states gives rise to the three quantum beat frequencies seen in the experiment. Damping of the quantum beats results from both population exchange

between triplet and singlet manifolds and pure dephasing between the triplet pair states. By lowering the temperature and slowing the SF rate, the visibility of the oscillations decreases. There is no evidence of magnetic dipole-dipole coupling between the product triplets. Our model provides good overall agreement with the data, supporting the conclusion that singlet fission in tetracene proceeds through "direct" mechanism without strong electronic coupling between the singlet and triplet pair states. This chapter further explains the process of SF within tetracene, and creates a model which could be the basis for a more complete understanding of SF.

A brief summary of the research is presented in Chapter 6, along with ideas for further experiments and the continuation of this research project. Further experiments that study the spread of excitation within single crystals of tetracene and energy transfer from tetracene triplets to other molecules are also discussed in Chapter 6.

This dissertation has clarified k_{fiss}, the rate of SF, in polycrystalline tetracene to be 1.25×10^{10} s^{-1} and found that great care needs to be taken in tetracene and possibly other polyacenes in order to prevent exciton exciton annihilation from distorting the observed kinetics. Additionally, an explanation has been found for the lack of observation of a triplet absorption in previous broadband transient absorption experiments on both tetracene and pentacene samples. Both photoluminescence and transient absorption experiments have also been successfully modeled with Merrifield's model of SF. Revisiting the previous work of Chabr et al. has enabled us to detect the same quantum beats with much greater signal to noise in order to apply density matrix simulations to model the quantum beats. Analysis of the quantum beats also shows that the triplets

formed from SF are formed at least 6 Å apart, and that they are not interacting strongly with each other upon creation. The observation and successful analysis strongly suggests that the direct mechanism of SF accurately describes the mechanism of how SF occurs within crystalline tetracene.

CHAPTER 2

Experimental

The experimental and sample preparation methods used in this work are described in this chapter. First, the three different laser systems are described in section 2.1. This is followed by the various steady state experiments in section 2.2. The time-resolved experiments that utilize the laser systems from section 2.1 are then described in section 2.3. Section 2.4 details the apparatus used for the magnetic field dependence as well as the microscopy measurements while Section 2.5 discusses the preparation of all the samples used in these experiments. Section 2.6 concludes the chapter with specific information on the data workup and calculations used in these experiments.

2.1 Laser systems

2.1.1 40 kHz laser system

A Ti:sapphire regenerative amplifier (RGA) operating at 40 kHz provides the pulses used for excitation in the time-resolved photoluminescence experiments. This laser was used for photoluminescence due to the high repetition rate, which allows for faster collection of data and lower fluences upon the sample.

2.1.1.1 Oscillator

The RGA is seeded by a femtosecond Ti:sapphire oscillator (Kapteyn-Murnane Model TS laser kit), which is pumped by a diode-pumped Nd:VO_4 laser (Millenia,

Spectra Physics). The optical layout for the oscillator is shown in Figure 2.1. With 3.30 W of pump power, the average output of the oscillator at 800 nm is ~250 mW at 91 MHz, which corresponds to ~2.5 nJ per pulse.

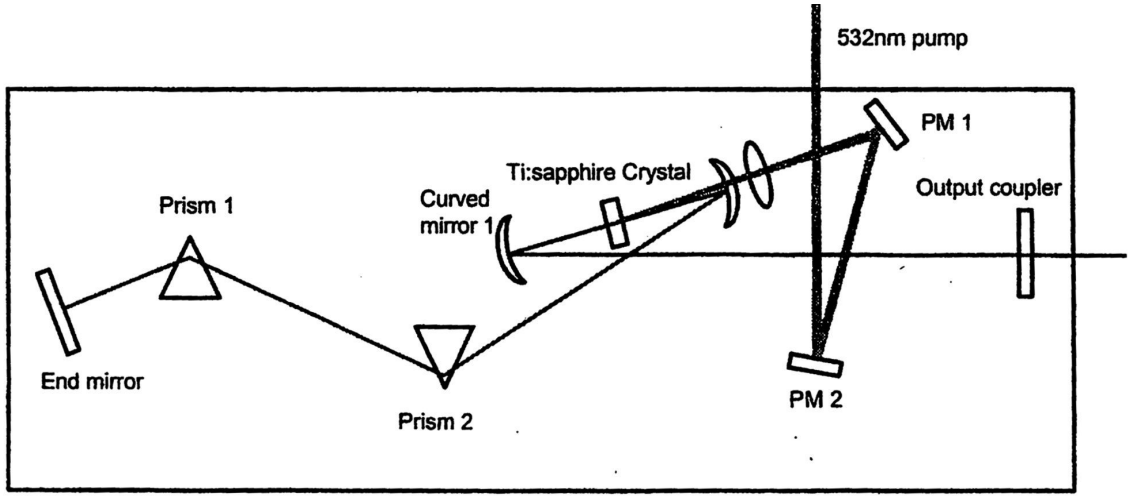

Figure 2.1 Optical layout for Kapteyn-Murnane Ti:sapphire oscillator, taken from the operations manual. [57]

2.1.1.2 Regenerative amplifier (RGA)

While the pulses from the oscillator are short enough to provide the necessary time resolution, the power from these pulses is not high enough to create the nonlinear processes used for generating the different excitation wavelengths. In order to generate these higher pulse powers, the oscillator pulses are amplified with a Ti:sapphire amplifier system (Spitfire-50, Spectra Physics). The optical layout for the amplifier is shown in Figure 2.2.

The RGA is pumped by a frequency doubled Q-switched Nd:YLF laser (Merlin-50, Spectra Physics), which outputs 532 nm with ~8 W of power at 40 kHz (~ 0.2 mJ per pulse). The pump beam does not typically need to be aligned, although it does need

realignment after a new lamp is installed in the pump laser. The output of the RGA is typically 200-250 mW, so that the pulses are approximately 5-6 μJ at 40 kHz. The output of the RGA is used in one of two non-linear processes to generate the excitation wavelength for experiments. The first is frequency doubling in a beta barium borate (BBO) crystal to take the 800 nm output and turn it into 400 nm light. The 800 nm light is then filtered out with dielectric mirrors and color filters before the 400 nm light is used as an excitation source. The second is continuum generation in a sapphire plate, where the 800 nm is converted into a broad spectrum from 450 – 800 nm. Small bandwidths can then be selected from this beam by use of interference filters.

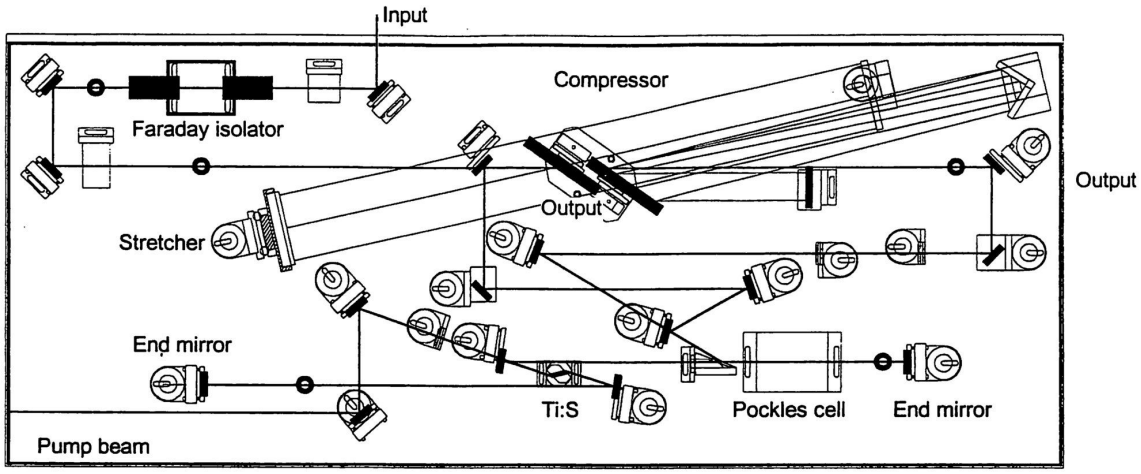

Figure 2.2 Optical layout for Spitfire-50, copied from the operational manual. [58]

2.1.2 1 kHz laser systems

A Ti:sapphire RGA operating at 1 kHz provides the pulses used for excitation in the transient absorption experiments. This laser was used for the transient absorption experiments since the lower repetition rate allowed for longer time windows in the

transient absorption experiments. Additionally, the higher power of this laser system is better able to power the nonlinear processes that are operative in the Palitra optical parametric amplifier (OPA), which created the tunable pump pulse used in the broadband transient absorption experiments. Two different RGA's were used for the broadband and single channel transient absorption experiments. In both experiments, the probe pulse was provided by white light continuum generated in either a sapphire plate or in a 1 cm cuvette filled with Millipore H_2O. The pump pulse for the single channel experiments was created by frequency doubling the 800 nm output of the RGA in a β-barium borate (BBO) crystal to change the wavelength to 400 nm. The probe pulse for these experiments was provided by white light continuum generated in a sapphire plate, which created a broad spectrum from 450-750 nm with low powers, typically < 0.1 μJ.

2.1.2.1. Spectra-Physics MaiTai oscillator and Quantronix Integra 1 kHz RGA

The Quantronix RGA (Integra-C, Quantronix) is seeded by a closed box Ti:sapphire oscillator (Maitai, Spectra Physics). This computer operated laser outputs 1.5-2.0 W at an 80 MHz repetition rate, corresponding to 19-25 μJ per pulse. The Quantronix RGA is pumped by a 1 kHz repetition rate diode-pumped Nd:YLF laser (Darwin), which typically outputs 9-10 W of 532 nm light at an operating current of 28.6 A, corresponding to 9-10 mJ per pulse. The layout for the Quantronix RGA is shown in Figure 2.3. The pump alignment needs to be adjusted daily, unlike in the 40 kHz RGA, and this can easily be done by optimizing the pump alignment on the first pass as well as the alignment on the second pass through the crystal, which are found in the second and

fourth mirrors after the Darwin pump laser, respectively. The RGA typically outputs 1.0-1.2 W at 790 nm, corresponding to 1.0-1.2 mJ per pulse.

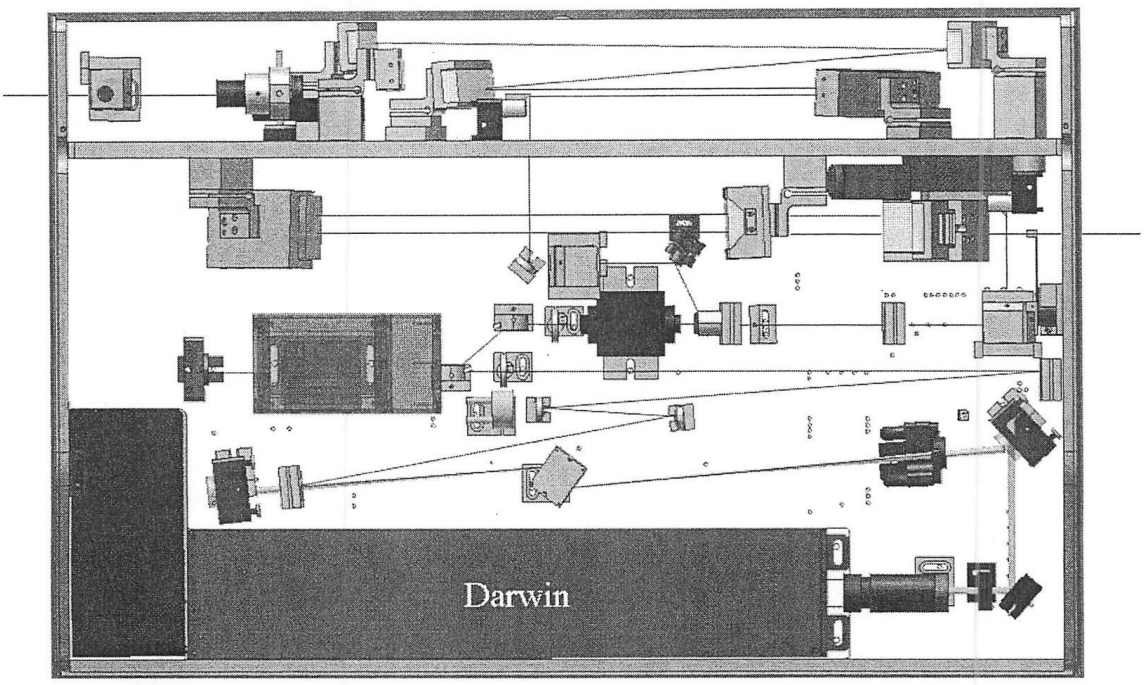

Figure 2.3 Optical layout for Quantronix Integra RGA, copied from operational manual. [59]

2.1.2.2 Palitra optical parametric amplifier (OPA)

For most applications, the short, intense pulses from the RGA would typically be sufficient to serve as the excitation source or to generate the probe source via continuum generation. However, the emission and absorption bands of interest do not always conveniently overlap with the output or the frequency doubled output of the RGA. This problem can be solved by use of an OPA. The Palitra OPA used in these experiments was commercially purchased from Quantronix. The wavelength range of the OPA

output is 270-1400 nm, with temporal pulsewidths > 100 fs and a bandwidth of 10-20nm. The optical layout for the Palitra OPA is shown in Figure 2.4. A pair of parallel dielectric mirrors is used to filter the beam to the desired wavelength, with several different pairs able to be switched into the setup for ease of operation, depending on which wavelength is being used.

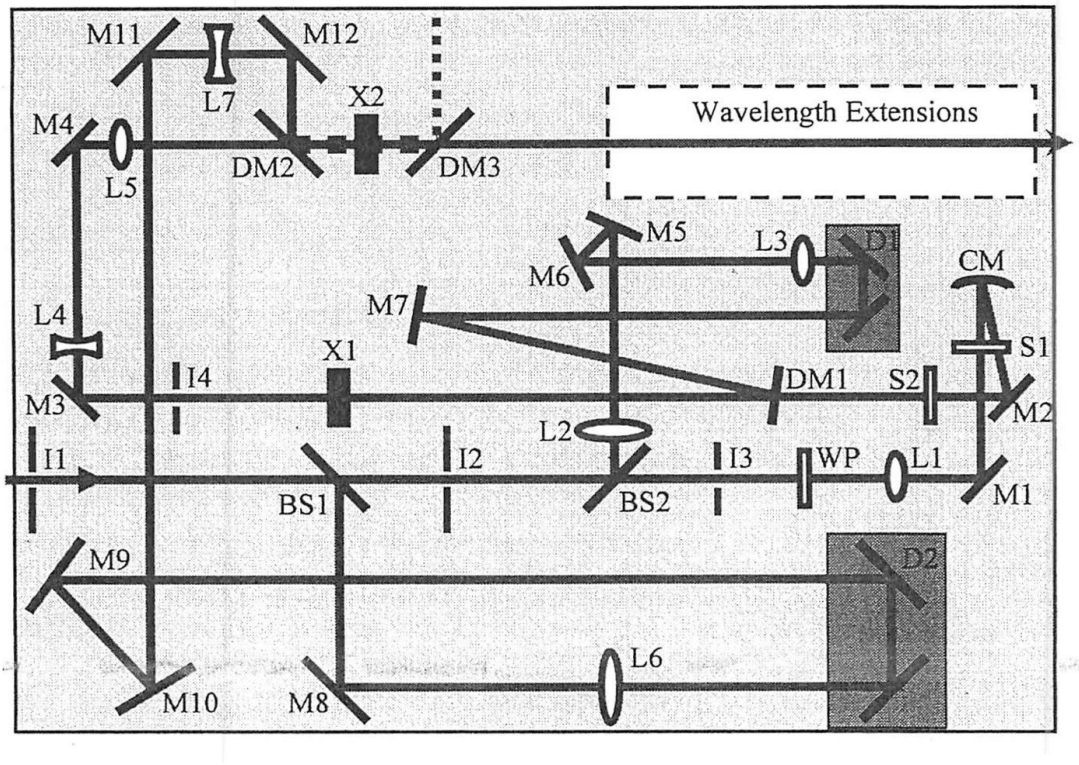

Figure 2.4 Optical layout for Palitra OPA, copied from the operational manual. [60]

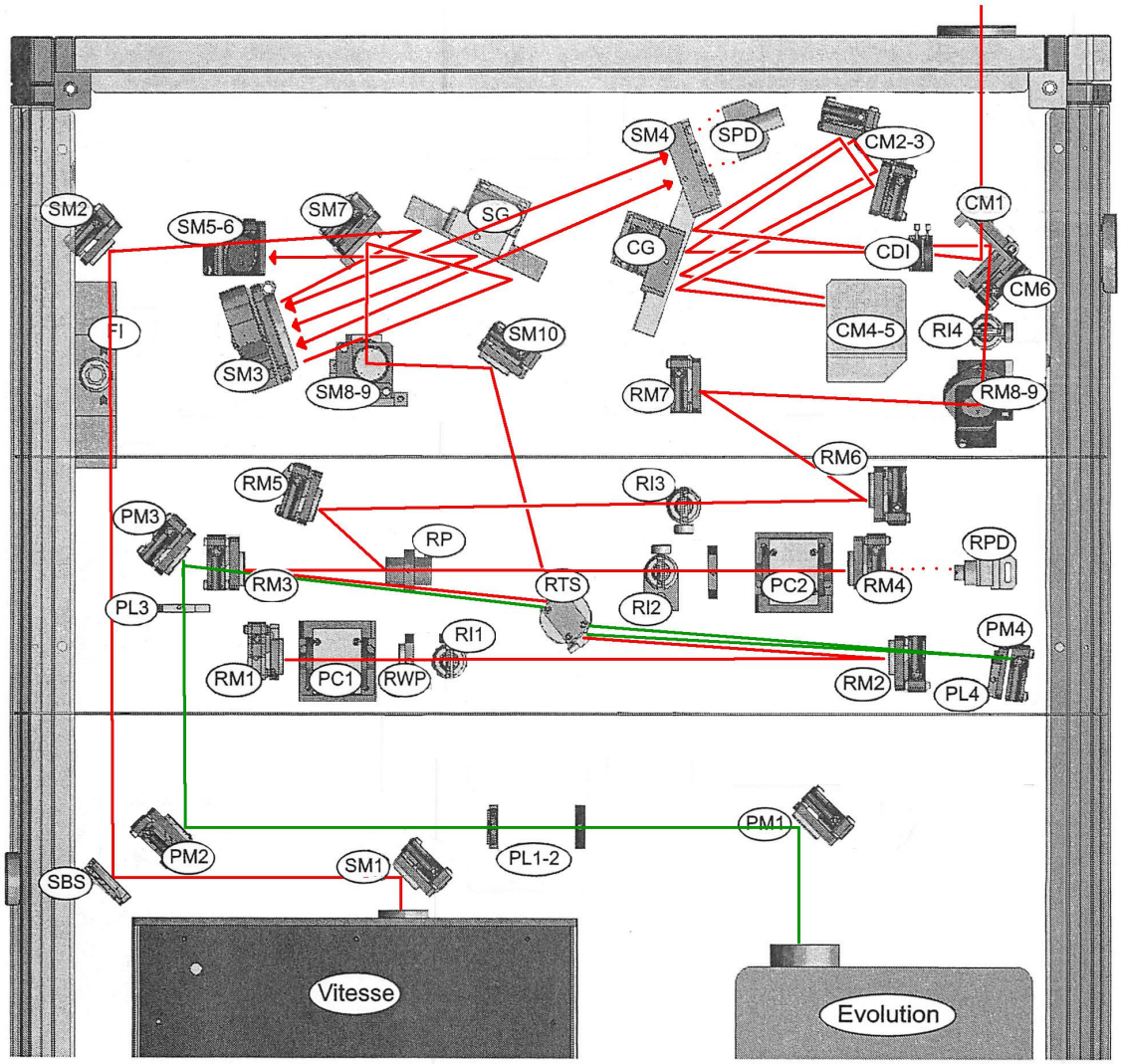

Figure 2.5 Optical layout for Coherent Libra RGA, copied from the operational manual with the beam path added. [61]

2.1.2.3 Coherent Libra 1 kHz RGA

The Coherent RGA (more specifically the Libra Femto HE 1K, Coherent) has a closed box Ti:sapphire oscillator built in (Vitesse, Coherent), which cannot be physically adjusted without breaking the hermitic seals. The oscillator can be manually aligned by

adjusting the peizo voltages on the oscillator control box front panel, but it is automatically optimized for the maximum output and modelocked. The output of the oscillator is 870-890 mW at an 80 MHz repetition rate, corresponding to 10-11 nJ per pulse. The Coherent RGA is pumped by a 1 kHz repetition rate diode-pumped, intra-cavity doubled, Q-switched Nd:YLF laser, which typically outputs 18 W of 527 nm light with a 1 kHz repetition rate and operating current of 20.6 A, corresponding to 18 mJ per pulse. The output of the RGA is 3.8-4.0 W at 1 kHz, corresponding to 3.8-4.0 mJ per pulse. The layout for the Coherent RGA is shown in Figure 2.5.

2.2 Steady state experiments

2.2.1 Steady state absorption using a Cary 50 spectrometer

Solution absorptions were obtained in a quartz cuvette by taking measurements in a Cary 50 spectrometer. The typical integration time was 1.0 s, and the wavelength steps were 1.0 nm.

2.2.2 Steady state absorption using an Ocean-Optics SD2000 spectrometer

Steady state absorption spectra of the solid samples were taken under vacuum in a Janis ST100 cryostat using an Ocean Optics SD2000 spectrometer. The light for these measurements was provided by a Analytical Instrument Systems, Inc. AIS DT1000 lamp, which created a broadband light source by focusing a tungsten and a mercury lamp into a fiberoptic cable. The light from this fiberoptic was collimated before being focused into a second fiberoptic which directed the light onto the CCD. After maximizing the light

hitting the CCD, the Ocean Optics software can be changed to absorption mode and a sample put between the two fibers. The typical integration time for absorption measurements was 100 ms, and 200 individual spectra were averaged to get the final absorption spectrum.

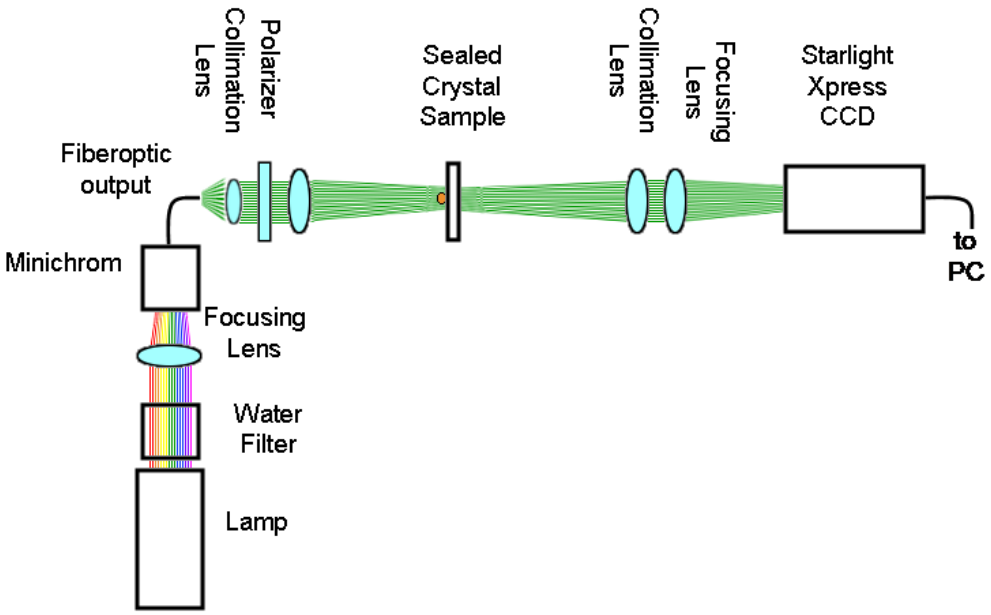

Figure 2.6 The experimental setup for the steady state single crystal polarized absorption. The lamp puts out white light, which the monochrometer is capable of filtering to the desired wavelength.

2.2.3 Steady state single crystal polarized absorption with CCD detection

Since the faces of the single crystals vary in size from several hundred microns to a 1 mm^2, the typical absorption spectrometer is not capable of determining an accurate absorption. To resolve this issue, a single crystal absorption spectrometer was created using a Xenon lamp, a Minichrom monochrometer and fiberoptic cable, focusing and collection optics, and a Starlight Xpress MX716 high sensitivity monochrome CCD. The setup for this spectrometer is shown in Figure 2.6.

The samples were mounted in one of two ways. The first method is when the sample was mounted inside the Janis ST-100 cryostat which was evacuated to $< 1x10^{-3}$ Torr. The second method for holding the sample is when the glass slide was sealed with a coverslip and torrseal under an Argon atmosphere in a glove bag. The glass slide was then mounted on a rotation stage with removable putty. The slide axis was then marked on the edge and the rotation stage polarization was noted so that the crystal axes could then be determined.

Using the Starlight Xpress CCD, images could be taken of the crystals, although the camera has no inherent wavelength discrimination. The monochrometer gives the wavelength resolution needed in order to create an absorption spectrum, while the polarizer allows for the determination of the crystal axes. The entrance to the monochrometer was a 1x4 mm slit, allowing for 10 nm resolution. Additionally, the monochrometer was calibrated with the Ocean Optics CCD described in Section 2.2.2 and found that the actual wavelength was 5 nm greater than the monochrometer indicated (i.e. 550 nm reading on the monochrometer actually corresponds to 555 nm).

Images were taken for each wavelength with a clean glass slide before the actual sample since the fiberoptic cable from the monochrometer created spatial variations in the intensity of the lamp. These were then used to correct the background in the actual crystal image files. The typical exposure time for the images ranged from 0.15 – 0.5 seconds.

The files from the Starlight Xpress software were saved as .fit files, which had to be converted to a usable format. To get the image data out, the .fit files were individually

opened in Intel Array Viewer. In the data tab, the individual pixel values can be copied from the program to paste them into Notepad to remove all the extraneous file markers. Once the file is pasted into Notepad, each file begins with

```
<?xml version="1.0"?>
<AvDataset Name="data" Class="SDS">
<AvSimpleType Type="Float"/>
<AvDataspace Rank="2">
<Dim Extent="376"/>
<Dim Extent="290"/>
</AvDataspace>
<Data Encoding="Formatted">
<Dim2>
```

and ends with

```
</Dim2>
</Data>
</AvDataset>
```

which can just be selected and deleted. Each line also begins with "<Dim1>" and ends with "</Dim1>", which can be easily found and deleted by using the "Replace" function in Notepad, accessed by pressing "CTL+h", and replacing them with a blank. This file can now be saved as a tab-delimited text file, which can then be imported into the Matlab work space.

In Matlab, the image files were first background corrected by subtracting off the appropriate wavelength blank file. The image files for each wavelength and polarization were then plotted as a 3-dimensional "Mesh" figure and examined in the X-Y orientation. From each image, the pixels for the area of the crystal and the transmitted light were found using the data reader. The absorption was calculated using Beer's law

$$A = -\log_{10}\left(\frac{I}{I_0}\right) \tag{2.1}$$

where I is the average value for the pixels of the crystal and I_0 is the average value of the background near the crystal (i.e. the transmitted light).

2.2.4 Steady state photoluminescence using a Fluorolog 3 spectrofluorimeter

Steady state photoluminescence spectra were measured with a Fluorolog 3 spectrofluorimeter with 400 nm excitation and front face detection. Samples were placed inside the Janis ST-100 cryostat, which was evacuated to < 1.0×10^{-3} Torr. The cryostat was bolted to a custom fabricated aluminum plate, which was mounted inside the spectrofluorimeter. The excitation and emission slits were always set to 2.0 nm, while the typical integration time was 1.0 ns with 1.0 nm per point.

2.3 Time resolved experiments

2.3.1 40 kHz photoluminescence

Photoluminescence lifetimes were taken using front face detection with a Hamamatsu C4334 Streakscope picosecond streak camera. The 400 nm excitation was generated by frequency doubling the 800 nm pulse from a 40 kHz Spectra-Physics Spitfire Ti:Sapphire regenerative amplifier. Scattered pump light was removed by placing a 450 nm long wave pass filter and 420 nm color filter on the input lens before the streak camera. The photoluminescence was detected at magic angle (54.7^{o}) relative to the pump to eliminate rotational diffusion effects. A power dependence on the

samples was done in order to determine the fluences where exciton-exciton annihilation became a factor. For tetracene thin films, the onset of singlet-singlet annihilation was observed at 4.05×10^{-5} J cm^{-2}, and triplet-triplet annihilation started at 1.22×10^{-5} J cm^{-2}. All the photoluminescence lifetimes were measured at fluences of 4.0×10^{-6} J cm^{-2} or below. No sample damage was observed at any of these fluences.

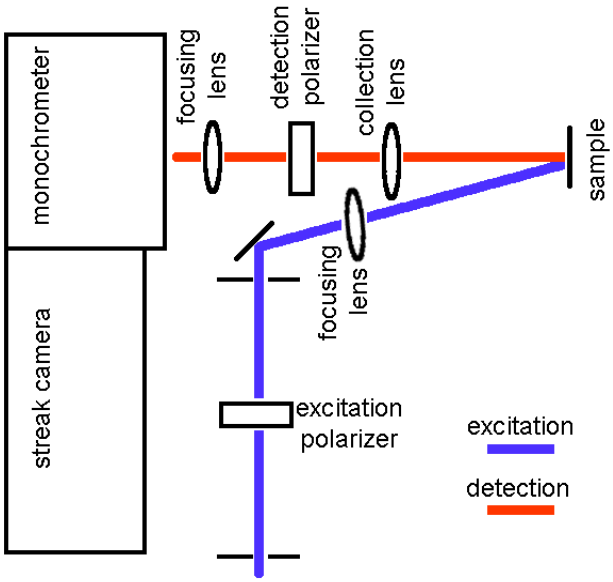

Figure 2.7 Experimental setup used for front face detection in time resolved photoluminescence.

Time resolved photoluminescence experiments on solutions, single crystals, and polycrystalline films were conducted in the setup shown in Figure 2.7, using front face detection with a Hamamatsu C4334 Streakscope picosecond streak camera with varied wavelength excitations. The 400 nm excitation was provided by frequency doubling the 800 nm output of a 40 kHz Spectra-Physics Spitfire Ti:Sapphire regenerative amplifier in

a BBO crystal. In order to prevent scattering of the 400 nm excitation light into the streak camera, a 450 nm long wave pass filter and a 420 nm color filter were placed before the streak camera. White light continuum (WLC) generation in a 3 mm sapphire plate served as the source for all other excitation wavelengths. Specific wavelengths were selected from the WLC using bandpass filters with 10 nm bandwidth or a Minichrom monochromator with 10 nm bandwidth, while a 514 nm cutoff filter was used to prevent scattered excitation from reaching the streak camera. The detection was polarized at magic angle relative to the excitation wavelength for all photoluminescence experiments. The photoluminescence decays were integrated from 500 – 640 nm unless otherwise noted. Multiple wavelength global analysis of the photoluminescence decays was performed using a commercial program (FAST, Edinburgh Instruments). Most photoluminescence measurements on solid samples were taken with the films or crystals mounted inside of an evacuated cryostat with pressures of $1x10^{-3}$ Torr or less. Alternatively, measurements were taken with samples under an argon atmosphere, achieved by gluing a cover slip to the glass slide with Torrseal epoxy.

2.3.2 1 kHz single channel transient absorption (TA)

Single-channel pump probe experiments were done with the probe beam at the magic angle relative to the pump beam. Both the pump and probe beams were provided by a 1 kHz Coherent Libra Ti:sapphire regenerative amplifier system operating at 800 nm. The pump beam at 400 nm was created by frequency doubling the 800 nm light in a BBO crystal. WLC generated in a 3 mm sapphire plate was the source for the probe

beam. The WLC was split into the probe beam and a reference beam, and both were directed to balanced photodiodes. These signals were subtracted in a lockin amplifier and normalized by the probe power in order to get the ΔT/T signal. These values are converted to units of ΔA using the relation $\frac{\Delta T}{T} = -2.303\Delta A$ which is correct as long as ΔA is less than $1x10^{-3}$.

Two different methods were used to acquire the single channel data. The first method selected the probe wavelength by using a pair of Andover 10 nm bandpass 532 nm interference filters placed immediately before the photodiodes. The second method, which allowed us to adjust the wavelength of the probe continuously, involved sending the probe and reference beams at different beam heights through a long focal length fused silica lens. Immediately after the lens, a SF10 prism was used to refract the beams onto an adjustable slit on a translation stage. After the slit, the probe and reference beams were then focused onto their respective photodiodes. The slit width and position were then adjusted to be to give ~10 nm bandwidth at 528 nm for the 77 K measurements.

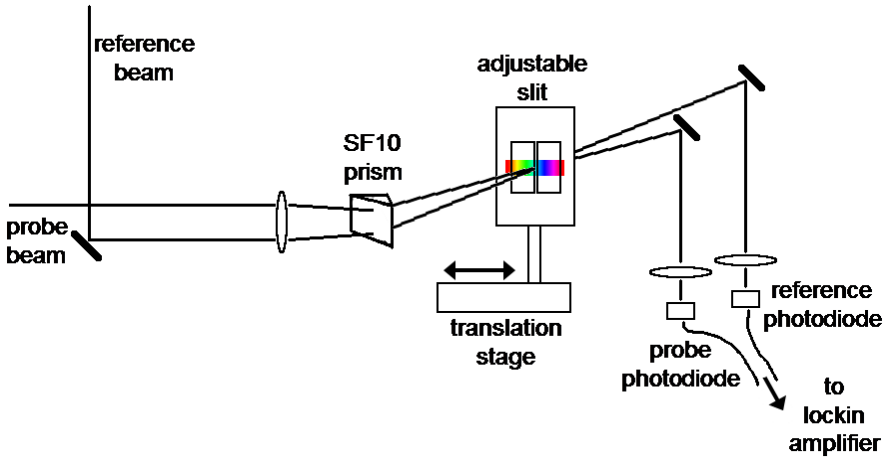

Figure 2.8 The experimental setup that was used for single channel TA.

2.3.3 1 kHz long delay single channel TA

For the long delay transient absorption experiments, the pump and probe were polarized parallel to each other. The probe and a reference beam were directed to balanced photodiodes with 10 nm bandpass 532 nm interference filters. The two signals were fed into a lockin amplifier and subtraction was used to obtain the ΔT signal. The first 2 ns of delay were achieved using the same stage used in the broadband transient absorption experiments, and longer delays were achieved by increasing the distance the probe beam traveled before generating continuum. For this purpose, two gold-coated mirrors were set up parallel to one another with a separation of 2 m, forming a cavity. The 800 nm pulse was directed into this cavity so that it bounced back and forth between the two mirrors, undergoing multiple round trips. The beam was picked off on different passes in this setup to extend the delay from 0 to 87 ns. After going through this delay, the beam was then used to generate continuum in the sapphire plate for use as the probe pulse. The transient absorption signal was then averaged with and without the probe in order to calculate ΔT/T signal levels. Each point was normalized according to pump power before being plotted.

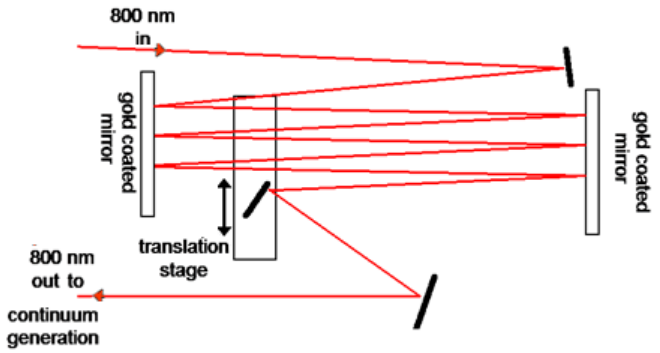

Figure 2.9 The experimental setup used to create the long delay before the single channel TA.

2.3.4 1 kHz broadband TA

Broadband transient absorption data was taken with an Ultrafast Systems Helios transient absorption spectrometer, both at Argonne National Labs and at UC Riverside. At Argonne National Labs, a Spectra-Physics (SP) Tsunami Ti:sapphire 75 MHz oscillator was used to seed a 1.66 kHz SP Spit-Fire Pro regenerative amplifier with 150 fs pulsewidth. 95% of the output from the amplifier is used to pump a Topas optical parametric amplifier, which is used to provide the pump beam in the Helios transient absorption setup. The remaining 5% of the amplifier is focused onto a sapphire crystal to create white light continuum to serve as the probe beam. The pump beam was depolarized and chopped at 833 Hz and both pump and probe beams were overlapped in the sample. The probe beam is then focused onto an optical fiber to direct the beam to the spectrometer. At UC Riverside, both pump and probe pulses were generated by a Quantronix Integra Ti:sapphire regenerative amplifier, operating at 1kHz with 1 mJ output at 790 nm, which was seeded by a Spectra-Physics MaiTai Ti:sapphire oscillator operating at 80MHz. The pump pulse at 400 nm was created by pumping a Quantronix Palitra optical parametric amplifier with 99% of the pump power. The probe beam was generated by taking 1% of the power to generate white light continuum in a sapphire plate. The pump beam was chopped at 100 Hz before the two beams were overlapped in the sample, and the probe beam went on to focus into an optical fiber which directed the beam to the CCD of the spectrometer. The time resolution of the TA systems was determined to be 250-300 fs by the width of the cross-correlation peak in the pure solvent. Solid samples were kept in the Janis ST100 cryostat under vacuum ($<5x10^{-4}$

torr). Solution samples ($7x10^{-4}$ M in toluene) were flowed through a 0.5mm path length cell, with a replacement rate of 3 mL/s. All samples were excited using pump fluences of $1.5x10^{-3}$ J cm^{-2} or less, and repeated scans showed no sample damage over the course of 30 minute scans.

2.4 Other experimental apparatus

2.4.1 Permanent magnet stage for variable strength magnetic fields

In order to conduct the magnetic field experiments on the polycrystalline films and single crystals, some mechanism for applying and controlling a variable magnetic field needed to be created. Electromagnet systems were examined, but using permanent magnets better fit our needs. Two cylinder shaped Neodymium permanent magnets (catalog #: DY0Y0-N50) with 2" diameter and 2" length were purchased from K & J Magnetics. The UCR machine shop was then able to make a non-magnetic mount for each magnet as well as a stage to control the position of the mounts out of a combination of aluminum, Teflon, and brass parts that was able to keep the magnets at a specific distance despite their strong attractive forces. The position of the magnets are adjusted by rotating the brass handles at either end of the stage, which twists a threaded rod, forcing the magnet mounts either closer or farther away. The magnetic field stage is shown in Figure 2.10.

This stage allows us to adjust the strength of the magnetic field upon the sample by varying the distance between the magnets. The field can be varied from ~ 300 G to 10 kG as shown in Figure 2.11, although the inclusion of the sample limits the magnets

separation to 16 mm and ~7 kG. The magnetic fields were measured with a Lakeshore Model 410 gaussmeter using the model HT 4658 transverse probe. In order to get true zero-field measurements, the magnet mounts were removed from the stage and placed in well separated areas of the room in order to prevent any danger from the magnets colliding. The samples for the magnetic field experiments were either mounted inside the brass cryostat or sealed under Argon and mounted on a xyz translation stage.

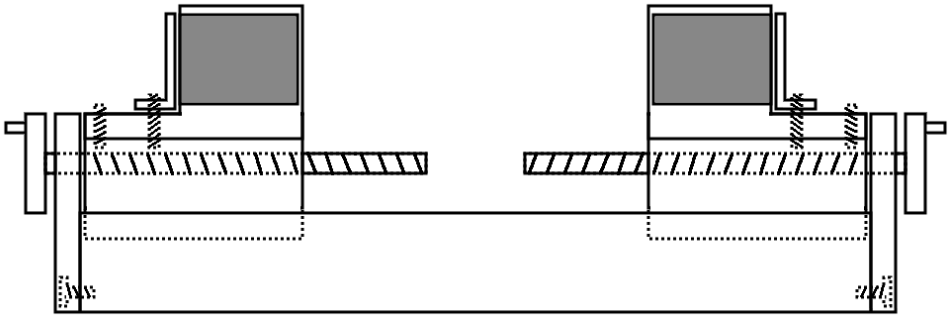

Figure 2.10 Illustration of the permanent magnet stage used to create variable strength magnetic fields. The dark gray area represents the position of the magnets while the diagonal lines indicate threads.

After running several photoluminescence experiments with streak camera detection on the 40 kHz laser setup, a small effect was noticed on the timing of the streak camera when the magnets were placed on the table. Specifically, the time of the excitation shifted by ~10 ps in a 1 ns time window. Measuring the magnetic fields with the magnet stage surrounding the usual sample position for photoluminescence (the magnet stage was 14.25" inside edge of the stage to the inside edge of the streak camera), the streak camera experienced a residual 2.0 G field due to the magnets. To alleviate this problem, the magnet stage and photoluminescence sample position were moved to be 27" away from the streak camera, where the field from the magnet stage was

indistinguishable from the background magnetic field near the streak camera (1.0 G). Once the sample and magnet stage were moved farther away, there was no effect upon the timing of the streak camera.

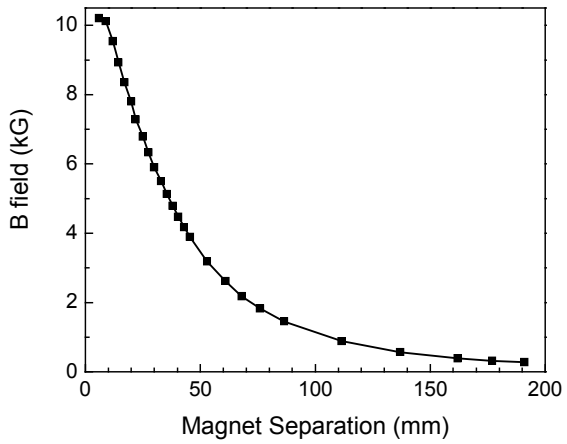

Figure 2.11 The magnetic field dependence upon the distance between the two permanent magnets.

2.4.2 Brass cryostat

In addition to the custom magnet stage, a custom cryostat was made by the UCR machine shop in order to conduct the B-field experiments. To conduct the magnetic field experiments, the cryostat needed to fulfill two distinct requirements. First of all, it needed to be made of a non-magnetic medium, which could hold a vacuum of at least $1x10^{-3}$ Torr. Second, it needed to be of a sufficiently small size to allow the magnets to generate a magnetic field of at least 4.5 kG (30 mm separation), but being able to access greater fields would be ideal. The machine shop was able to fabricate a cryostat with a width less than 13 mm, which allows for fields of ~7 kG inside the cryostat, shown in Figure 2.12.

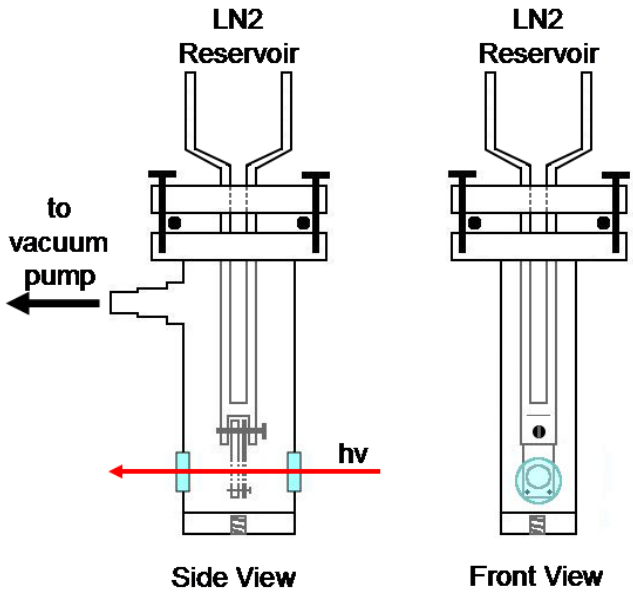

Figure 2.12 An illustration of the design of the brass cryostat used for the magnetic field measurements. The black circle between the top and bottom portions indicates the Viton o-ring while the red arrow indicates the path of excitation.

Two quartz windows were affixed to the cryostat with Torrseal to create a good seal, while the top portion was held to the bottom with 8-32" screws. These screws were always hand tightened to compress a Viton o-ring between the two brass plates and enable the brass cryostat to be evacuated. Using a 1/4" inner diameter rubber vacuum hose attached to a molecular drag pump, the lowest pressure achieved was 1.0×10^{-4} Torr without any cryogen and 5×10^{-5} Torr with liquid nitrogen. The temperature of the cryostat with liquid nitrogen was calibrated with amorphous rubrene photoluminescence lifetime and comparing it the photoluminescence lifetime at known temperatures taken in the Janis ST100 cryostat with a calibrated thermocouple. The temperature of the sample in the brass cryostat is confirmed by these measurements to be < 100 K.

The cryostat was attached to a square aluminum rod which was also bolted onto a xyz-translation stage to allow for fine control of the spatial position of the sample inside the cryostat. The thin rod also allowed for the cryostat to be placed above the rail in the magnetic stage, so that the sample inside experienced the maximum magnetic field possible.

2.4.3 Atomic force microscopy

Atomic force microscopy measurements were carried out with the help of Julia Lingyun Zhu. The measurements were conducted on a Novascan atomic force microscope in tapping mode. The scan resolution was set to 400, and scans were done over 80 μm x 80 μm squares. For a more detailed discussion of the theory of atomic force microscopy, refer to Julia Lingyun Zhu's thesis.

2.4.4 Polarizing microscopy

Polarizing microscopy measurements were conducted by adding thin film polarizers around the sample in a standard microscope. Additionally, a 550 LWP filter was used in order to minimize photoxidation damage. The first thin film polarizer was placed above the tungsten lamp, along with the filter. An Olympus UPlanFl 4x with 0.15 numerical aperature was used to view the crystals, and it allowed the viewing of several crystals simultaneously. The second thin film polarizer was taped to the bottom of this objective. In order to have crossed polarizers, the first polarizer was adjusted until the background was dark and the crystals were bright. The best single crystals had ~1 mm^2

surface area, and were well separated from other crystals. These crystals were noted by drawing an arrow to them with a Sharpie permanent marker to ensure the correct crystal is studied.

2.4.5 X-ray diffraction

Powder X-ray diffraction data were collected on a Bruker D8 Advance X-ray powder diffractometer (CuK radiation, λ = 1.5418 Å, 40KV/40mA power) at 296 K. Vacuum evaporated polycrystalline films of tetracene of ~100 nm on microscope slides were used in order to have sufficient signal to noise. For further information on this experiment, refer to Lingyun Zhu's dissertation.

2.5 Sample preparation

Tetracene from two different sources was used for these experiments and gave identical results. Tetracene purchased from TCI was purified via sublimation prior to use, while tetracene purchased from Aldrich (sold as Benz[b]anthracene sublimed grade, 99.99% trace metals basis) was used as received. The tetracene vials and all samples were wrapped in foil and kept in an evacuated dessicator with Drie-Rite in order to limit any photoxidation.

2.5.1 Sublimation purification

Tetracene can be purified by sublimation, and this has to be done on the tetracene purchase from TCI due to an oxidation impurity in their sample. To do this, ~10 mg are

of TCI tetracene are placed in a microsublimer. The sublimer is then clamped above an oil bath on a labjack, and the water and vacuum hose is connected to the vacuum line shown in Figure 2.13. The mechanical pump is then turned on, and the vacuum is opened to the sample to pump down to < 10 mTorr before placing a dewar full of liquid Nitrogen around the trap. The pressures typically reach ~1 mTorr after the cryogen is added. The oil bath is then heated to 140-160^{o} C. While the sublimation at the lower end of this range takes longer, it can typically purify the tetracene in one sublimation rather than two. Once the temperature of the oil bath has stabilized, the cooling water for the sublimer is turned on, and the oil bath is raised up to immerse the sublimer. The sublimer is then left in the oil bath for 6-10 hours, until the cold finger is covered in a dark orange film. In order to minimize light exposure, the oil bath and sublimer are covered with tin foil during the sublimation process.

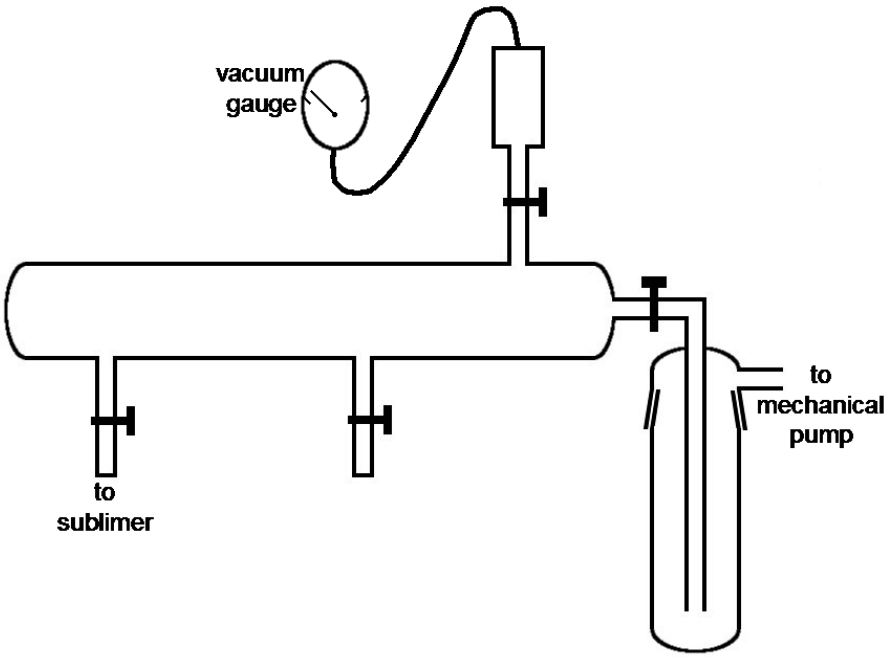

Figure 2.13 Diagram of the vacuum system used for the sublimation purification of tetracene.

When the sublimation is done, the heat is turned off and the sublimer removed from the heat. Once the sublimer is cool to the touch, the cooling water is turned off and the vacuum and cooling water hoses are removed. The sublimer is then carefully separated into its two pieces, and the purified tetracene is then removed from the cold finger with a new razor blade. The typical yield from the sublimation is < 50%, although repeated sublimations will have higher yields.

2.5.2 Tetracene solutions

Monomer samples of tetracene for the TA experiments were made by dissolving ~3 mg of tetracene into ~10 mL of toluene and sonicated for 10 minutes. The solutions were then filtered through Whatman Qualitative 1 filters to remove any undissolved tetracene crystals. The product of this was a saturated solution of 0.7 mM tetracene in toluene.

2.5.3 Vacuum evaporated polycrystalline tetracene films

For the polycrystalline films, glass slides were cut into ~1 cm by 3 cm pieces and cleaned in tetrahydrofuran before being placed in a base bath. After the base bath, the substrates were rinsed with deionized H_2O and dried in an oven at 200º C. In order to grow the polycrystalline films, ~ 1 mg of tetracene was placed into the sample boat inside the Pelco vacuum evaporator and substrates placed on the stage ~3" below the sample boat. The sample chamber was then pumped down over the next 4 hours with the built in diffusion pump. Once the pressure inside the sample chamber was 1.5×10^{-5} Torr or less,

the evaporating current was turned on in 7 second increments, waiting ~1 minute in between to monitor the growth of the film. When the film was a very light yellow (indicative of < 0.3 peak absorption), no more current was applied. The diffusion pump was then closed and the film removed for spectroscopic investigation.

2.5.4 Tetracene single crystal growths

Using three different methods, we could grow single crystals with areas of up to 1 mm^2. Thin crystals are necessary to prevent self-absorption distortions of the photoluminescence spectrum. Single crystals were identified using polarizing microscopy with light > 550 nm in order to minimize photoxidation.

2.5.4.1 Solution grown tetracene single crystals

Single crystals of tetracene were formed on glass slides and cover slips by solvent evaporation from a saturated tetracene solution in toluene with a concentration of $7x10^{-4}$ M. Substrates were covered with tin foil or a cardboard box in order to minimize light exposure to the samples and prevent photooxidation. Using this method, we could grow single ultrathin (<100 nm) single crystals with areas of up to 1 mm^2. These thin crystals are necessary to prevent self-absorption distortions of the photoluminescence spectrum. Single crystals were identified using polarizing microscopy with light > 550 nm in order to minimize photoxidation.

2.5.4.2 Sublimation grown tetracene single crystals

The crystals with the longest delayed fluorescence lifetime were grown by sublimation in a microsublimer. This process is very similar to the purification by sublimation, with a few key differences. The first difference is that a much smaller amount of tetracene was used. Additionally, the single crystal growth is a much slower sublimation due to the higher pressure since the house vacuum was used. Finally, a sand bath is used instead of an oil bath to try and minimize temperature fluctuations. After placing ~1 mg of tetracene into the sublimer, it is held in a clamp above the sand bath and pumped on with the house vacuum. The sand bath is then heated up to 170^{o}. Once the temperature of the sand bath has stabilized, the cooling water for the sublimer is turned on, and the sublimer is placed in the sand bath. The sublimer is then left in the sand bath form 12-24 hours, until large area crystals are seen growing from the cold finger. In order to minimize light exposure, the sand bath and sublimer are covered with tin foil during the sublimation process. After the crystals are grown, the heat is turned off and the sublimer removed from the heat. Once the sublimer is cool to the touch, the vacuum and cooling water are removed. The sublimer is then carefully separated into its two pieces, and the crystals on the cold finger are then removed by tapping the sublimer on the counter over a glass microscope slide. The crystals are then examined via polarizing microscopy to identify the single crystals. A pair of tweezers with a very fine tip can be used to separate the crystals, as well as to push the crystal onto a small amount of vacuum grease to affix it to the slide.

2.5.4.3 Physical vapor grown tetracene single crystals

The method for the physical vapor growth of tetracene films and crystals was adopted from a method successfully used on other organic semiconductors.[62] Thin films and single crystals were also grown under flowing argon by horizontal physical vapor growth, with a source temperature of 180º C, and a deposition temperature ranging from 140-160º C, as measured by an infrared thermometer. The source tube and gas inlet attachments shown in Figure 2.14 were custom-fabricated in the glass shop to correspond to what has been previously used in the field to grow large area single crystals of various organic molecules, from α-thiophene to pentacene.[62] The source tube was wrapped in two heating tapes with separate controllers in order to better control the temperature in the tube. The heating tape was wound closer together at the starting end of the tube in order to achieve the higher temperature needed to sublime the tetracene, while the winding spread out the farther the tape was from the high temperature end. Argon was used as the carrier gas for this crystal growth, and an oxygen/H_2O trap was placed in the gas line before it got to the crystal growth tube to maximize the crystal purity. Additionally, a bubbler was placed after the gas outlet to minimize any oxygen from the atmosphere flowing back into the tube. Glass substrates were cut to fit inside the tube, and then placed along different sections of the tube to try and maximize the amount of crystals collected. The tetracene was then placed inside a smaller tube, which was positioned just after the position with the highest density of heating tape on the outer tube. After everything was placed in the tube, the gas flow was turned on so that there were approximately 2-3 bubbles / s. Once the proper gas flow was assured, the whole

tube was covered in tin foil to minimize light exposure and temperature gradients due to air currents. At this point, the voltage was turned on to the heating tapes, with periodic monitoring of the temperature, gas flow, and crystal growth.

After approximately 4 hours, several slides should have crystals growing on both sides. Since the tube is round, the bottom of each slide does not have contact with the tube, allowing crystals to grow on either side. The heat is turned off, and the tube is allowed to cool down for approximately 30 minutes while the gas is still flowing. When the tube is safe to touch, the gas flow is turned off, and the glass slides are removed. One side of the slides is wiped off with acetone on a kimwipe so that only one side has crystals on it. Then the slides are examined using polarizing microscopy to identify the single crystals.

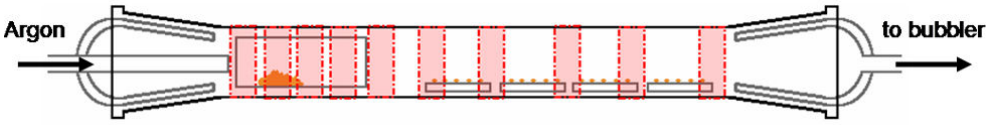

Figure 2.14 The experimental setup for the physical vapor growth of tetracene crystals. The red squares indicate the heating tape wrapped around the outside tube. The tube containing the source material was placed on the side with the incoming carrier gas, where the heating tape was wrapped more densely. The oxygen/H_2O trap and bubbler are not pictured here.

2.5.5 Tetracene nanocrystal suspension in water

Another method for creating crystalline tetracene was by repricipitation in water, which was used previously in our lab.[63] A 1.0 mM solution of tetracene in spectroscopic grade tetrahydrofuan was made, according to the same procedure described in section

2.5.1. 10 mL of water from a MilliQ filtration system (Millipore) was rapidly stirred in a scintillation vial before 100 μL of the tetracene/THF solution was injected with a microsyringe, with the needle placed underneath the surface of the water before injecting to ensure prompt dispersal of the tetracene throughout the water. The solution was covered in foil and allowed to stir for an additional 10 minutes before any spectroscopic measurements were made.

2.6 Calculations and methods for data workup

2.6.1 Excitation density calculation

In order to calculate the excitation density, the absorption of the sample at the excitation wavelength is combined with the number of incident photons (determined by a power measurement) in order to determine the number of photons absorbed, which is the equivalent to the number of excitations. This can also be calculated by measuring the power before and the power after, but with fluences < 1 μJ, this becomes inaccurate due to the limitations of the power meter. The volume of excitation was then calculated from the sample thickness and the area of the laser spot. The thickness of the samples was calculated from the absorption using Beer's Law, which atomic force microscopy experiments confirmed to be reliable. The spot size of each laser was measured independently by translating a razor blade through the laser focus.

2.6.2 Time resolved photoluminescence data workup

Files were saved as image and data files, *.img and *.dat respectively, after collection on the streak camera, with the x-axis (640 pixels) providing the wavelength and the y-axis (480 pixels) providing the time. The *.img files could be reopened later using the streak camera control software (HPD-TA 7.1.0), but extracting photoluminescence spectra and decays from this filetype was not convenient. Loading the *.dat files as a matrix into Matlab by dragging it into the workspace enabled easy extraction of the photoluminescence spectra and decays using prewritten programs already found in our lab, the full code of which can be found in Appendix I. In order to correct the drift in the streak camera timing, a separate Matlab program called SCshift2 was used to correct this error

SCshift2(SCdata,b)

where *SCdata* equals the input photoluminescence matrix and *b* equals the slope of the offset to apply to fix the streak camera problem, which is typically 0.02 in 1 and 20 ns windows. Extraction of the photoluminescence decays were achieved with the timewindow program in Matlab

timewindow(data, w_ini, w_window)

where *data* is the input photoluminescence matrix, *w_ini* is the wavelength pixel (x-axis pixel) to start integrating from, *w_window* is the width of the integration window in pixels. The program then sums up the counts for all of those columns to create the decay. The swindow program is very similar is just like the timewindow program except that the

window start and width are chosen along the y-axis so that the rows rather than the columns are summed.

2.6.3 Oscillation extraction

In order to isolate the oscillations on top of the background decay, the photoluminescence decay was fit with either with a double or triple exponential with an offset. This fit was then subtracted from the decay, leaving the oscillations centered on zero, with between 390 and 450 time pixels. Fourier transforms were performed in Matlab using the built-in fast Fourier transform function. Simulated oscillation data was created in by analytically solving the later described theoretical model with tetracene's parameters and varying the rates to achieve the best agreement with the experimental data. In order to accurately compare the simulated data with experiment, it was convolved with the instrument response along with adding an offset to account for the delayed fluorescence. The simulated data was 1001 points long, and the Fourier transforms were conducted on the simulated data with zero-filling out to 1024 points using the fast Fourier transform function in Matlab.

2.6.4 Global analysis

Before the global analysis can be conducted on the photoluminescence data using FAST by Edinburgh Instruments, our data needs to be formatted to be accepted by the program. The following table illustrates the format of the data files created in Excel,

Time (ns)	IRF (counts)	Signal (counts)
0	#	#
…	#	#

where the first column is the time axis generated by the streak camera, the second column is the instrument response function, and the third column is the signal for a specific set of wavelengths. However, the file cannot have the headings shown in the example table above. To create the Signal column, the photoluminescence *.dat file is loaded into Matlab and corrected, and then 10 kinetic traces of 64 pixel width are created using the timewindow program in order to have sufficient signal to noise to enable accurate fitting with the following command:

```
sum(data(:,"start":"end"),2);
```

The created columns are then put into 10 separate files as the "Signal". It is important to note that normalized decays will not be fit by the FAST software because it only uses whole numbers or counts for the y-axis. An instrument response function (IRF) is also created using the timewindow function from a measurement with the streak camera monitoring the scattered excitation pulse. Once all the columns are appropriately filled, each file can be saved as a text tab delimited file. After the file is saved, the filetype can be changed from *.txt to *.fst to enable the FAST software to open it. All 10 traces are loaded into FAST, then selected by shift-clicking each before starting the Global Analysis function. Reconvolution and Advanced Global Fit are selected, and the fitting is set to 1 to -1 to fit the whole decay. If this fitting area needs to be adjusted, it is important to note that the values used are in pixels rather than units of the x-axis (i.e. ns).

The number of components is then set to 2 (or 3 as needed), and all the lifetimes are linked so that they are the same for all the different decays. Additionally, the longer lifetimes were sometimes fixed in the 1 ns window fits based on fits in 20 and 100 ns windows. After all the parameters for fitting were set, the global analysis was calculated. The fits can be viewed all together or separately based on how many traces are currently selected. The content of each window can be saved by right-clicking and exporting as a text file. However, each window, such as the data with the fit, the residuals of the fit, and the fit parameters, needs to be exported separately so that no information is lost. Data from the text file can then be copy/pasted into Origin to make better plots.

CHAPTER 3

Excited State Dynamics in Solid and Monomeric Tetracene

3.1 Introduction

In this chapter, we study the excited state dynamics in polycrystalline thin films of tetracene using both picosecond photoluminescence and femtosecond transient absorption. We compare our solid-state results with those obtained for monomeric tetracene in dilute solution. Our room temperature photoluminescence decay data are consistent with earlier models that take into account a range of processes, including exciton-exciton annihilation (both singlet and triplet) and SF. The main difference between our data and earlier data on single crystals is a drastically reduced triplet lifetime in the polycrystalline films, a phenomenon that may have implications for devices based on evaporated thin films. Femtosecond TA measurements on the monomer in solution reveal several excited state absorption features that overlap the ground state bleach and stimulated emission signals on the picosecond timescale. On longer timescales, the initially excited singlet state completely decays due to intersystem crossing, and the triplet state absorption superimposed on the bleach is observed, consistent with earlier flash photolysis experiments.[64] In the solid-state, the TA dynamics are completely different from those of the monomer, with a dominant stimulated emission signal that decays on a 10 ps timescale superimposed on weak excited state absorption features. We attribute this unexpectedly large signal to a superradiant $S_0 \rightarrow S_1$ transition. The enhanced absorption strength of the $S_0 \rightarrow S_1$ transition, along with the partially oriented nature of

our polycrystalline films, makes it difficult to unambiguously observe the weaker $T_1 \rightarrow T_N$ absorption features in the solid film. In order to confirm that triplets are the dominant excited state species after photoexcitation, we simultaneously measure the delayed fluorescence (due to triplets) and ground state bleach decay. The fact that they decay on identical timescales is consistent with the picture that the excited state dynamics are dominated by SF followed by triplet diffusion and recombination. Our experimental results clarify some of the complexities inherent in the spectroscopy of large polyacenes in the solid state, including the roles of superradiant excitons and defect states. We find no evidence, however, that the overall picture of solid-state tetracene photodynamics being dominated by SF and triplet recombination requires significant revision.

3.2 Results and discussion

3.2.1 Film morphology and steady state properties

In order to facilitate comparison with our solid tetracene data, the solution-phase absorption and photoluminescence spectra of monomeric tetracene, along with its molecular structure, are shown in Figure 3.1. Figure 3.2a shows a typical AFM image of an 80 nm thick tetracene film prepared using thermal evaporation under a 10^{-5} Torr vacuum. Most of the film consists of submicron tetracene crystallites evenly distributed across the substrate. As the film thickness is increased, either by extending the deposition time or by using a larger amount of tetracene in the evaporation boat, the density of the crystallites increases and larger crystallites begin to appear.

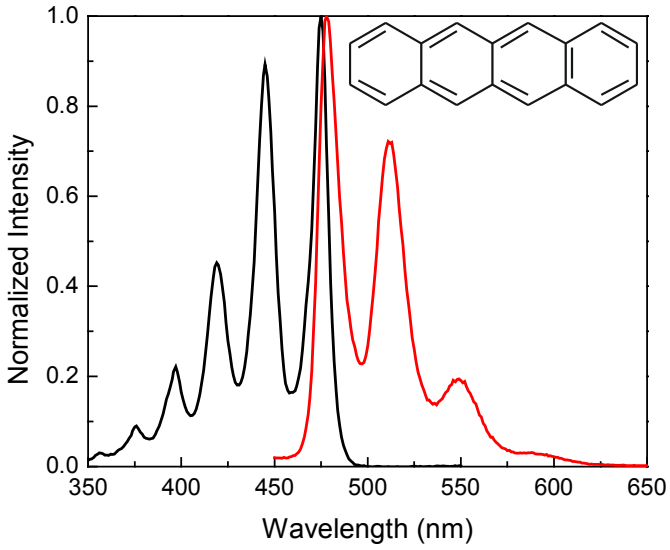

Figure 3.1 Normalized steady state absorption (black) overlapped with the steady state photoluminescence (red) of the tetracene monomer in toluene illustrating the vibronic structure and small Stokes shift of monomeric tetracene.

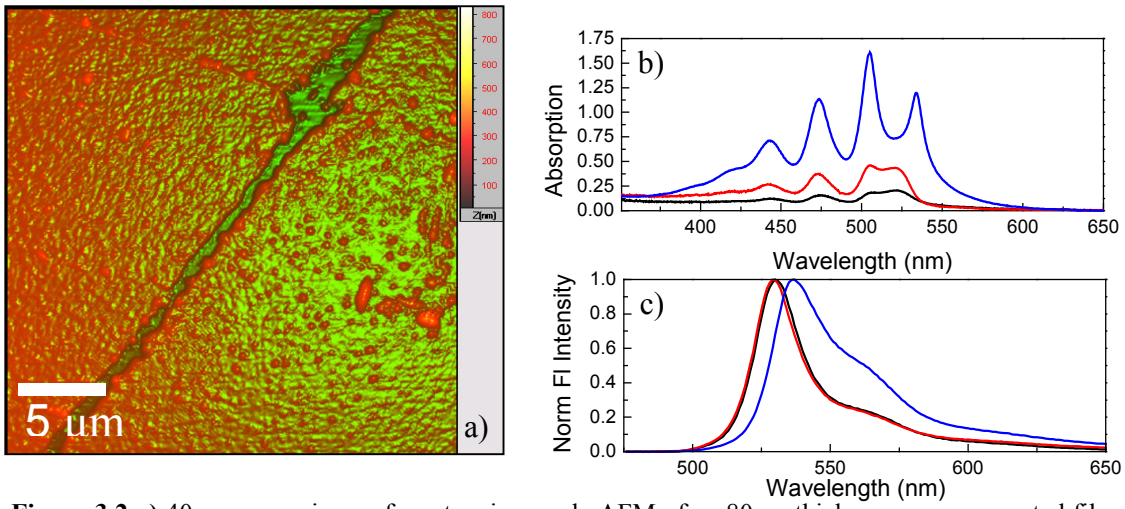

Figure 3.2 a) 40um square image from tapping mode AFM of an 80nm thick vacuum evaporated film. **b)** The absorption spectra of 40nm (black), 80nm (red) and 215nm (blue) thick vacuum evaporated films, showing shape changes due to optical effects. **c)** The normalized photoluminescence spectra of the same films.

The crystallites tend to align with their ***ab*** planes parallel to the substrate surface, and this fact, along with the large Davydov splitting in tetracene, has a strong influence on the optical properties of the thin films. Hofberger showed that the changes in optical lineshape observed with increasing film thickness, could be understood in terms of

differential absorption of the ***a*** and ***b*** Davydov components of microcrystallites randomly oriented in the ***ab*** plane, combined with scattering.[24,65] We observe the same phenomena in our evaporated thin films, as shown in Figure 3.2b. The increased intensity of the high energy ***b*** Davydov peak and sharpening of the absorption features are both purely optical effects and should not be mistaken for changes in electronic states. The other important effect of increasing film thickness is to distort the photoluminescence spectrum due to self-absorption. While peak absorption values up to ~0.5 appear to give rise to undistorted photoluminescence spectra, higher absorptions lead to an apparent redshift of the photoluminescence peak as well as enhancing the 0-1 and lower energy vibronic peaks in the photoluminescence spectrum, as shown in Figure 3.2c. This distortion of the true photoluminescence spectrum by self-absorption is a significant concern when the lineshape is used as an indicator of exciton coherence length. For all our photoluminescence measurements, the peak optical density was 0.2 or less, resulting in undistorted emission spectra. The two undistorted spectra clearly demonstrate the enhanced 0-0 peak that is a signature of the J-type delocalized exciton in the crystalline state.[66] The lack of long-range crystallinity and relatively broad absorption lineshapes (i.e. short T_2 dephasing times) means that refractive index effects, like polariton formation, are not a concern. Our physical picture of the films is that they consist of crystalline aggregates, with the ***ab*** plane parallel to the substrate, but otherwise behaving independently, much as they would if isolated as a dilute suspension in an inert liquid like water.

3.2.2 Time-resolved photoluminescence

The photoluminescence decays of monomeric and polycrystalline tetracene show dramatic differences. In Figure 3.3a, the photoluminescence decay of tetracene in toluene solution is a single exponential with a time constant τ_{fl} = 4.2 ns, similar to what has been observed for tetracene in other solvents.[67,68] The solid film, on the other hand, exhibits a biexponential decay with ~90% of the photoluminescence decaying with a τ_{prompt} = 80 ps and a second, much longer-lived component with $\tau_{delayed}$ = 55 ns. In previous work, the subnanosecond decay of the prompt fluorescence is usually assumed to result from rapid SF, while the longer-lived component arises from delayed fluorescence (DF) arising from triplet-triplet recombination that repopulates the emissive singlet state. Thus the DF lifetime reflects the triplet exciton lifetime and is expected to depend sensitively on sample morphology. In Figure 3.3b, we compare the photoluminescence dynamics of a vacuum evaporated thin film with those of a single crystal. The crystal DF is essentially flat in this time window, and we estimate its lifetime to be 5-10 μs. This value places it within the range of other measurements in single crystal tetracene but below the longest measured DF lifetimes of 5 μs or greater.[69-73] The inset in Figure 3.3b compares the transient photoluminescence spectra for early time (0-1 ns) and late times (100 ns – 1 μs) for the evaporated film, confirming that the DF originates from the same singlet state as the prompt fluorescence.

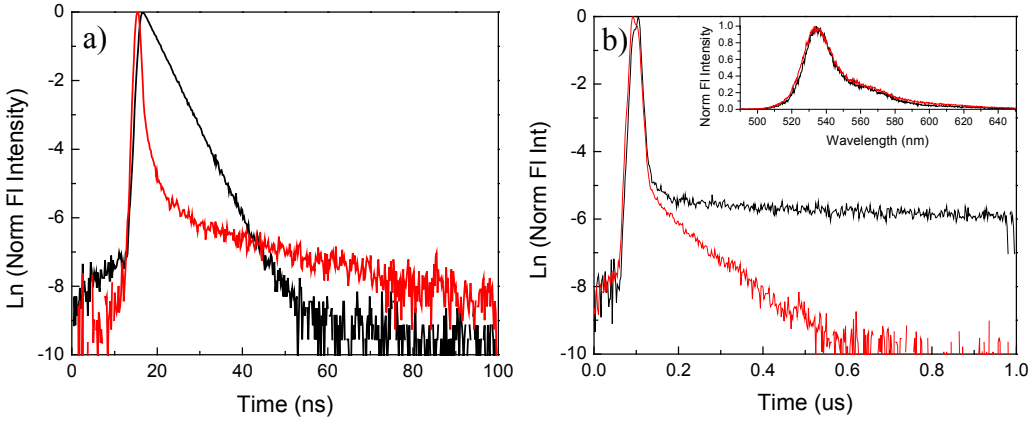

Figure 3.3 a) The normalized photoluminescence decays of monomeric tetracene in toluene (black), which gives rise to a single exponential decay, and a 60 nm thick vacuum evaporated polycrystalline film (red) which exhibits prompt and delayed fluorescence decays. **b)** Comparison of the decays of a sublimation grown single crystal (black) and the 60nm thick vacuum evaporated polycrystalline film (red). Inset in **b)**: the spectra of the film at early (0-2 ns) and late (500-1000ns) times during the decay.

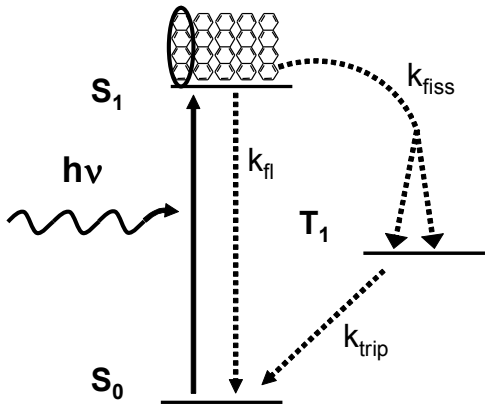

Figure 3.4 Schematic illustration of simple 3-level kinetic system used by previous workers to analyze photoluminescence dynamics in crystalline tetracene. Note the singlet state is localized on a single tetracene molecule. Only the dominant kinetic processes are shown.

The dependence of triplet lifetime on crystal quality has been noted by earlier workers, but the 55 ns lifetime of the DF decay in polycrystalline films is much shorter than the shortest lifetime (2 μs) reported for single crystal samples. We have found that

the lifetime of the DF ranges from 20-100 ns for polycrystalline samples prepared by reprecipitation in water as well as for thick versus thin films grown by either evaporation method. Hence this drastic shortening of the triplet lifetime appears to be a general feature of polycrystalline tetracene grown by random, nonequilibrium assembly.

To further examine the photoluminescence dynamics, and also to make contact with previous kinetic models for tetracene photoluminescence, we examine the intensity dependent dynamics and quantitatively model them using the kinetic scheme shown in Figure 3.4. For tetracene solid, there are a variety of processes that affect the population of the singlet excited state, which is what is monitored by our photoluminescence measurements. We consider both the triplet and singlet populations:

$$\frac{dN_{S1}}{dt} = -(k_{rad} + k_{ic} + k_{isc} + k_{fiss})N_{S1} + k_{TS}N_{T1}^2 \tag{3.1a}$$

$$\frac{dN_{T1}}{dt} = -k_{trip}N_{T1} - k_{TS}N_{T1}^2 - k_{TT}N_{T1}^2 + (k_{isc} + 2k_{fiss})N_{S1} \tag{3.1b}$$

where k_{rad} is the radiative decay rate, k_{isc} is the intersystem crossing rate, k_{ic} is the internal conversion rate, k_{fiss} is the fission rate, k_{trip} is the triplet decay rate for an isolated triple, and k_{TT} and k_{TS} are the triplet-triplet annihilation rates to form higher energy triplet or singlet states, respectively. Using this model, we can reproduce the intensity-dependent photoluminescence decays in thin tetracene films shown in Figure 3.5a for excitation densities of $4.5\text{x}10^2$ μm^{-3}, $5.4\ \text{x}10^3$ μm^{-3}, and $3.0\text{x}10^4$ μm^{-3}. To model this data, we numerically solve the coupled differential equations (1a,b) with Matlab using the parameters $k_{trip} = 6.7\text{x}10^6$ s^{-1}, $k_{fiss} = 9.3\text{x}10^9$ s^{-1} [48,53,73-75], $k_{rad} = 1.2\text{x}10^8$ s^{-1} [42], $k_{TT} = 2.0\text{x}10^{-10}$ cm^3s^{-1}, $k_{TS} = 5.0\text{x}10^{-10}$ ns^{-1}, and $k_{ee} = 1.0\text{x}10^{-8}$ cm^3s^{-1}, while assuming that k_{ic}, and k_{isc}

are negligible (see Appendix I for the Matlab program used). We note that the literature values for the exciton-exciton annihilation rates (k_{ee}, k_{TS}, k_{TT}) [53,54,69,70,72,76,77] vary by at least an order of magnitude, and our values are within the middle of these ranges for all three parameters. In accordance with the work of Pope and coworkers[23], we found it necessary to have a non-zero k_{TT} in order to reproduce the trends with intensity. We also convoluted the decays with a Gaussian instrument response function with a 1/e time of 12 ps. The traces shown in Figure 3.5b reproduce the qualitative trends in the data, but we did not attempt to quantitatively overlap the simulations with the data for the following reasons. First, there is considerable uncertainty in the actual excitation density, perhaps as much as a factor of 2, due to the difficulty of measuring the absorption of such thin films accurately. Second, as mentioned above, many of the parameters of this model have not been independently measured to high precision, making it difficult to find a unique solution for this multidimensional problem. The main point of this exercise is to demonstrate that our measurements are consistent with previous work that modeled the photoluminescence dynamics under the assumption that the excited state relaxation is dominated by SF. The results in Figure 3.5 should not be taken as validation for the simple model in Figure 3.4, but rather as a consistency check to show that our photoluminescence data can be parameterized in the same way as previous single crystal data, indicating that there is no large discrepancy between the physical behaviors of the two systems.

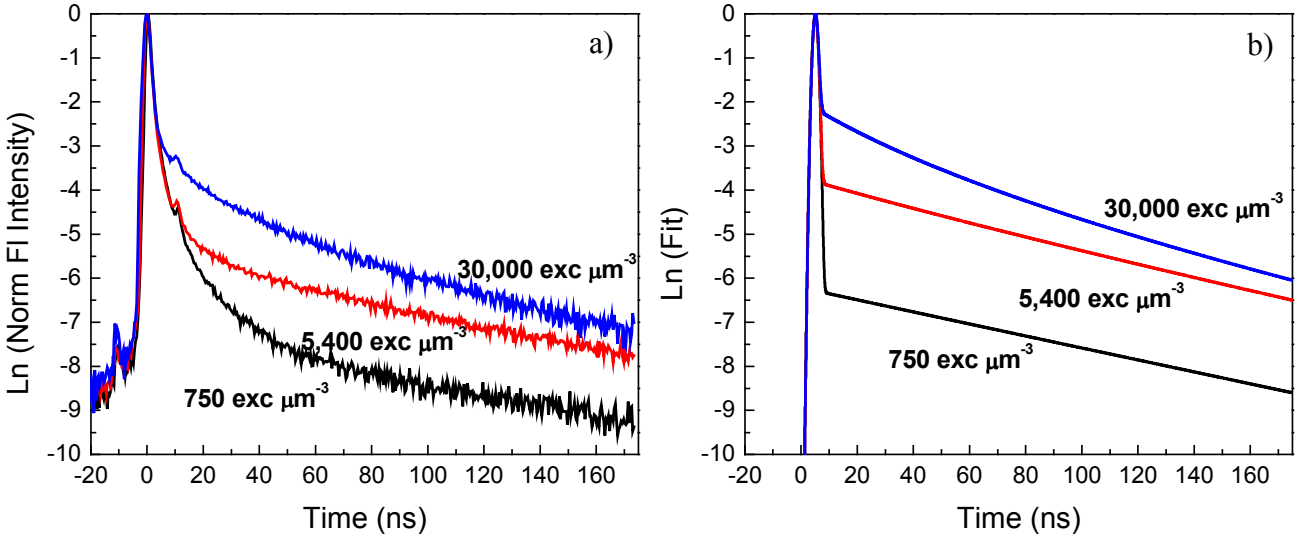

Figure 3.5 a) The photoluminescence decays from an evaporated tetracene thin film at three different excitation densities: 750 (black), 5400 (red) and 30000 (blue) exc μm^{-3}. As the excitation density increases, the delayed fluorescence becomes a larger fraction of the decay, but at the highest intensities triplet-triplet annihilation accelerates the decay of the delayed fluorescence. **b)** Simulated photoluminescence decays generated by using Equations (1a,b) and the experimental excitation densities. The parameters for the model are $k_r = 1.2 \times 10^8\ s^{-1}$, $k_{ic} = k_{isc} = 0\ s^{-1}$, $k_{trip} = 6.7 \times 10^6\ s^{-1}$, $k_{ee} = 1.0 \times 10^{-8}\ cm^3\ s^{-1}$, $k_{fiss} = 9.3 \times 10^9\ s^{-1}$, $k_{TT} = 2.0 \times 10^{-10}\ cm^3\ s^{-1}$ and $k_{TS} = 5.0 \times 10^{-10}\ cm^3\ s^{-1}$.

The DF lifetime deserves special mention, since it is at least a factor of 10 shorter than what has been reported for macroscopic single crystals. Given the simple three-state model outlined in Figure 3.4, one would expect the decay of the DF to be exactly twice as rapid as the triplet decay, since at any point in the triplet decay, the singlets and triplets are in quasi-equilibrium and we can set $\frac{dN_{T1}}{dt} = 0$ and show

$$N_{S1} \propto N_{T1}^2 \propto \exp[-2k_{trip}t] \tag{3.2}$$

Thus the DF decay time is half the triplet lifetime, i.e. the triplets survive for only 40-200 ns in the thin films. This shortened lifetime is probably due to rapid diffusion of the triplets to the crystallite boundaries, where they are expected to encounter a high density

of structural defects that can act as quenching sites. We can calculate a three-dimensional diffusion length

$$L_D^{trip} = \sqrt{6D\tau_{delayed}} \tag{3.3}$$

Given a diffusion constant D = 1x10^{-4} cm^2/s, taken as an average of literature values[69,76,78-80], and $\tau_{delayed}$ = 55 ns, we can calculate L_D^{trip} = 140 nm. This distance is greater than the thickness of the evaporated films and consistent with the crystallite size in the evaporated film as seen in Figure 3.2a. As mentioned before, this shortened lifetime appears to be a general feature of our polycrystalline samples, and this feature may have implications for organic photovoltaic devices based on evaporated polycrystalline films.

3.2.3 Transient absorption measurements in solution

We now turn to the femtosecond transient absorption experiments, which should provide a more direct way to monitor the triplet population and confirm the role of SF. We begin by examining the spectroscopy of tetracene monomer in toluene solution. Figure 3.6 shows the TA spectrum 300 fs after excitation at 410 nm. The signal is positive for all probe wavelengths, signifying that excited state absorption plays an important role. Notable features include a large peak at 450 nm and broad, weaker peaks at 650 nm and 1190 nm.

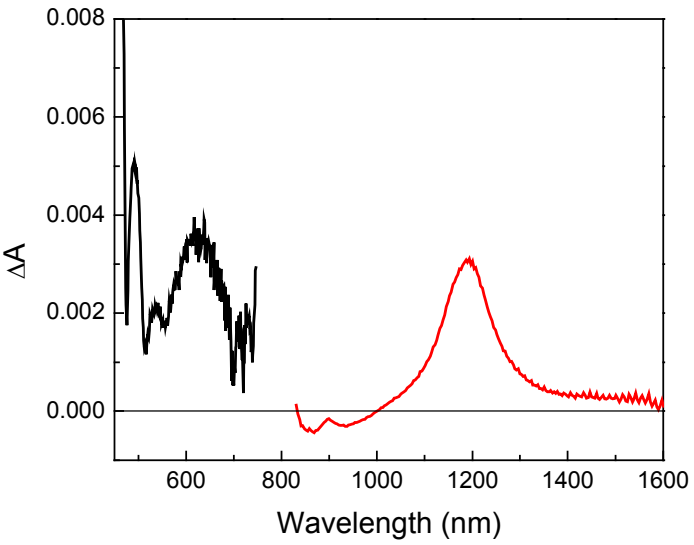

Figure 3.6 The transient absorption spectrum of tetracene monomer in toluene ($7x10^{-3}$ M) 300 fs after excitation. The bleach and stimulated emission peaks at 480-560 nm are on top of three excited state absorptions centered approximately at 450 nm, 650 nm, and 1200 nm.

Based on selection rules and theoretical calculations of tetracene's electronic state energies[81-84], we can tentatively assign the last two transitions as the ${}^1B_{2u}^+ \rightarrow {}^1A_{1g}^-$ and ${}^1B_{2u}^+ \rightarrow {}^1B_{1g}^-$ transitions, respectively. The decays of the lower energy peaks at 650 nm and 1190 nm exactly parallel that of the photoluminescence decay in toluene, at least to the 50% level at 2 ns delay, which was the limit of our delay stage. The evolution of the spectral region from 450-600 nm is more complicated. The bleach ($S_0 \rightarrow S_1$ peak at 475 nm) and stimulated emission ($S_1 \rightarrow S_0$ peaks at 477, 515 and 554 nm) are all negative features that are clearly visible, but they are superimposed on top of the positive absorption features centered at 450 nm and 650 nm. Note that the bleach and stimulated emission peaks appear as a single large peak due to the small Stokes shift in tetracene. At all wavelengths, the dynamics can be fit in terms of a single relaxation time τ_{fl} = 4.2 ns

using a function of the form $Ae^{-t/\tau_{fl}} + y_0$. Note that the amplitude A and offset y_0 can be positive or negative. This form for the decays is what is predicted by a simple model where the dynamics are governed by a single relaxation process, in this case the photoluminescence decay due to intersystem crossing to the T_1 state.

At longer times, intersystem crossing should leave approximately 60-80% of the molecules in their triplet state, based on previous measurements in room temperature solution.[67,68] Thus after the S_1 state has completely decayed, we expect to see two features remaining in the TA spectrum: a ground state bleach signal and a feature corresponding to the strong $T_1 \rightarrow T_N$ absorption centered at 465 nm. Although many $T_1 \rightarrow T_N$ absorption features have been identified in tetracene, the peak at 465 nm is the strongest, with a peak absorption coefficient $\varepsilon(T_1 \rightarrow T_N)$ ranging from $3x10^4$ $M^{-1}cm^{-1}$ to $9x10^4$ $M^{-1}cm^{-1}$ according to literature values[64], as compared to the peak absorption for the $S_0 \rightarrow S_1$ transition $\varepsilon(S_0 \rightarrow S_1)=10700$ $M^{-1}cm^{-1}$. We have measured the TA spectrum at a delay of 20 ns, where we expect the singlet population to be negligible. This spectrum is shown in Figure 3.7a, where it appears as a single broad peak with a dip at 475 nm corresponding to the negative bleach signal. When the scaled linear absorption is subtracted from the TA signal, we obtain the spectrum shown in Figure 3.7b, which is in good agreement with the $T_1 \rightarrow T_N$ absorption measured by flash photolysis experiments in a variety of different solvents and glasses.[64] In order to subtract the ground state bleach, we had to scale the spectra by assuming that the $T_1 \rightarrow T_N$ peak absorption coefficient is 2.76 times larger than that of the ground state $S_0 \rightarrow S_1$ absorption. Given $\varepsilon(S_0 \rightarrow S_1)=10700$ $M^{-1}cm^{-1}$, this results in an estimate for the triplet absorption

$\varepsilon(T_1 \rightarrow T_N)=2.9x10^4\ M^{-1}cm^{-1}$. This is close to the value of 31200 $M^{-1}cm^{-1}$ that was measured in flash photolysis experiments on monomeric tetracene dissolved in benzene.[85] Thus the long-time (20 ns) behavior of tetracene in solution is consistent with previous flash photolysis experiments: a weak negative bleach superimposed on a strong $T_1 \rightarrow T_N$ excited state absorption. The only surprise in the TA spectroscopy of monomeric tetracene is the preponderance of $S_1 \rightarrow S_N$ excited state absorption features at early times that outweigh the ground state bleach and stimulated emission contributions.

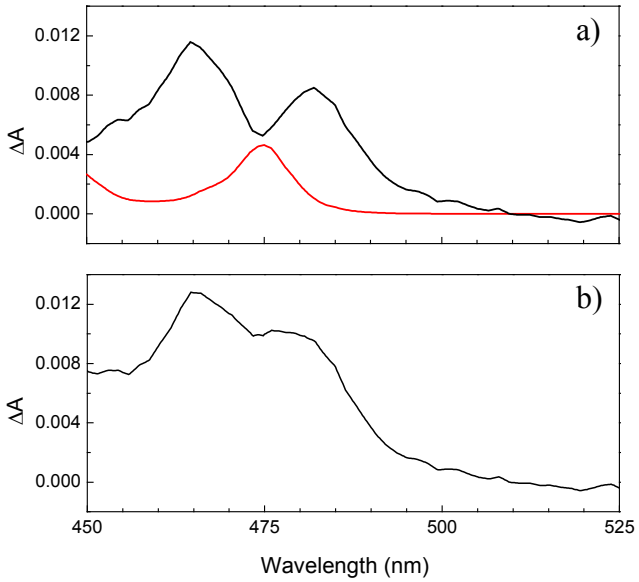

Figure 3.7 a) Transient absorption spectra of the tetracene monomer in toluene (0.7 mM) 20 ns after excitation (black), after the initially excited singlet state has relaxed. Also shown is the steady state absorption spectrum (red) in this wavelength region. **b)** The triplet absorption of tetracene monomer, obtained by adding the steady state spectrum to the 20 ns transient absorption spectrum.

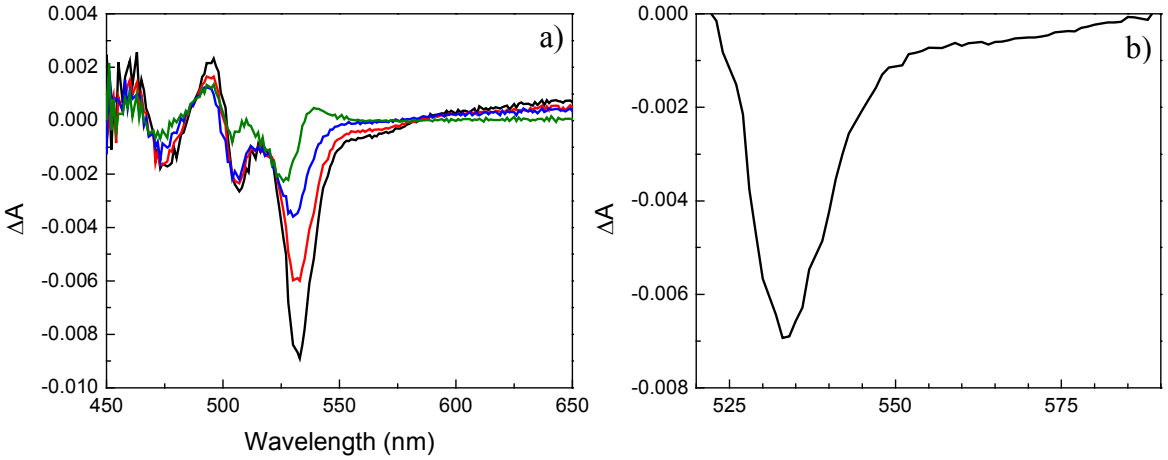

Figure 3.8 a) Transient Absorption spectra data from a 35nm thick vacuum evaporated tetracene with a fluence of $7x10^{-4}$ J/cm^2 at 300 fs (black) , 5 ps (red), 15 ps (blue) and 1950 ps (green) delays, illustrating the fast decay of the stimulated emission within 15 ps of excitation. **b)** The spectrum of the short-lived stimulated emission from the tetracene film, obtained by subtracting the 1950 ps spectrum from the 300 fs spectrum.

3.2.4 Transient absorption measurements in solid film

Based on our results for the photoluminescence of solid tetracene, which are consistent with rapid SF occurring on a 100 ps timescale, and the observation of a strong $T_1 \rightarrow T_N$ absorption in the monomer, one would naively expect the TA experiment on the solid film to show a transition from bleach/stimulated emission signals at early times to a dominant $T_1 \rightarrow T_N$ absorption within 100 ps. This is not what is observed, however, as the data in Figure 3.8a show. The signal is dominated by an intense negative peak centered at 533 nm that decays within 15 ps. The high energy Davydov peak at 505 nm does not change at all during this time, while the blue-shifted vibronic peaks in the bleach show much smaller changes. The spectrum of the short-lived species can be obtained by subtracting the spectrum at long delay (1950 ps) from the 300 fs spectrum. The result is shown in Figure 3.8b and looks similar to the photoluminescence spectra seen in Figure

3.2c and Figure 3.5, but with a strongly enhanced 0-0 peak at 533 nm. The decay of this species depends on laser intensity, but at lower pump fluences (< $3.5x10^{-4}$ J/cm^2), the decays initally appeared to be independent of pump intensity in the broadband TA experiments. Based on these results, we fit the decay to single exponential in the TA to a relaxation time of 9.2 ps, as shown in Figure 3.9a. The 533 nm peak most likely corresponds to stimulated emission, since it has a very small Stokes shift, but its decay is much more rapid than the 80 ps decay observed in the photoluminescence experiments. It should be noted, however, that the time resolution of the streak camera used in those measurements was limited to 20 ps, and it would not have been able to resolve the 9.2 ps decay evident in Figure 3.9a. The rapid decay of the bleach/stimulated emission signal is accompanied by a slight increase in absorption in the region around 475 nm that occurs on the same timescale, as shown in Figure 3.9b. This is close to the wavelength where we would expect to see the $T_1 \rightarrow T_N$ absorption, according to the results in Figure 3.7, but its amplitude is much weaker than in the monomer. In Figure 3.9c, the decay of a low amplitude induced absorption at 650 nm which corresponds to the same wavelength where the $S_1 \rightarrow S_N$ absorption was observed in the monomer (Figure 3.6). This feature also decays on the same 9.2 ps timescale as the stimulated emission at 533 nm. All these data are consistent with an initially excited singlet state that disappears within 10 ps. After the initial 9 ps decay, the dynamics at all wavelengths are completely flat on a 2 ns timescale – all the interesting spectral dynamics occur very early, within the first 15 ps or so after excitation. Our TA data in tetracene is qualitatively similar to what has been observed in thin films of pentacene[27,28,51], but the singlet decay is not consistent with our

photoluminescence lifetime data, which leads us to expect a singlet state that decays an order of magnitude slower, ~100 ps instead of ~ 10 ps. The discrepancy between the initial fluorescence and TA dynamics led us to postulate the existence of a defect state, but the experiments in Chapter 4 show that this is not needed to explain the dynamics.

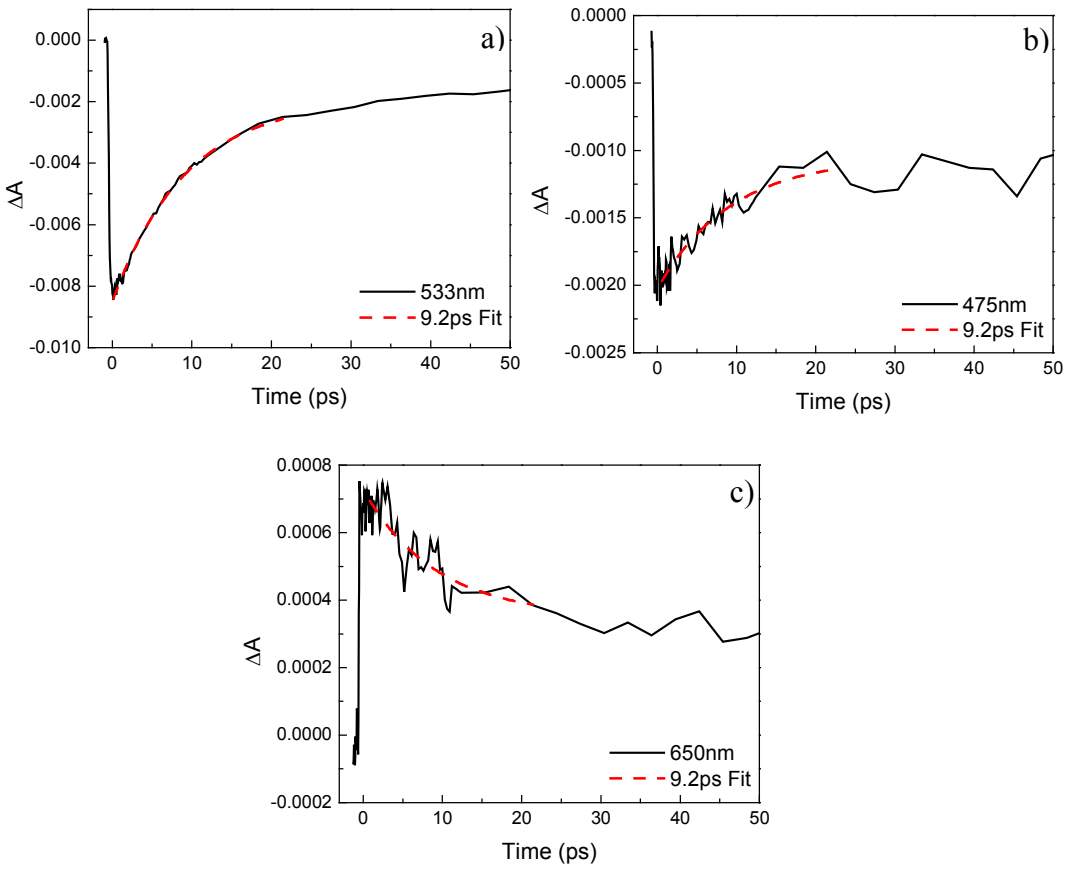

Figure 3.9 Transient absorption kinetic traces from the 35 nm thick vacuum evaporated tetracene film with a fluence of $7x10^{-4}$ J cm^{-2}, along with single exponential fits of the rapid initial dynamics using a 9.2 ps time constant. **a)** 533 nm TA signal (black) with 9.2 ps fit (red dashed). **b)** 475 nm TA signal (black) with 9.2 ps fit (red-dashed). **c)** 650 nm TA signal (black) with 9.2 ps fit (red dashed).

For completeness, we briefly compare our data to previous measurements on tetracene single crystals.[51,86] Comparison of the two sample types is complicated by the very high optical density of the single crystals which makes it difficult to analyze spectral

information due to attenuation effects. In neither of these studies was an attempt made to reconcile their data with parallel photoluminescence measurements, nor was the crystal orientation specified. In both previous experiments on single crystals, the small initial bleach signal disappeared within a few hundred picoseconds, and the signal was dominated by a very broad induced absorption centered at around 700 nm that appeared within a few hundred femtoseconds and survived for more than a nanosecond. Frolov et al. assigned this feature to trapped singlet excitons, while Thormsolle et al. assigned it to the $T_1 \rightarrow T_N$ absorption, despite the fact that no $T_1 \rightarrow T_N$ features are observed at this wavelength in the isolated molecule. Thormsolle et al. concluded that after 400 nm excitation, SF occurs via two channels: a direct 300 fs relaxation from the photoexcited S_N state and via a thermally activated pathway from the relaxed S_1 state on a timescale of 50 ps, significantly longer than the 9.2 ps decay that we observe. A possible physical reason for any discrepancies is the fact that the packing of tetracene molecules on a SiO_2 surface may be different from that in a single crystal (see discussion below). At this time, however, we cannot fully explain the discrepancies between our transient absorption data from thin films and the data on the single crystals, although similar differences observed by Thormsolle in their comparison of pentacene thin film and single crystal were ascribed to the complete absence of SF in the thin films.[51]

3.2.5 Comparison of photoluminescence and transient absorption results

Comparison of the femtosecond TA data with the picosecond luminescence data raises two obvious questions regarding the physical interpretation of the data. First, why

is the decay of the singlet state so much more rapid in the TA data than in our photoluminescence data, and why is the 80 ps PL decay not observed in the TA data? Second, why is a strong $T_1 \rightarrow T_N$ absorption not observed in the solid samples, given that there is expected to be an even greater yield of triplets than in solution, where the $T_1 \rightarrow T_N$ absorption was easily observed? Below we address both of these questions in an attempt to develop a self-consistent physical picture for tetracene's solid state photodynamics.

Our initial explanation for the apparent discrepancy between the picosecond photoluminescence data and the femtosecond TA data is that the 80 ps decay observed in the streak camera experiments does not originate from the initially excited S_1 state seen in the TA data, but instead is due to a superradiant defect state that can be populated both by the initial excitation pulse and through triplet-triplet recombination. The existence of such a defect state in tetracene would be consistent with our previous results in anthracene[41], a closely related molecular crystal. Additionally, a detailed analysis of the temperature-dependent photoluminescence of tetracene films on graphite by Voigt et al. has provided evidence for the participation of several emissive states that are very close in energy but which can be resolved at lower temperatures.[87] However, as the work in Chapter 4 shows, exciton exciton annihilation accounts for all of the differences between the singlet decay monitored through TA and photoluminescence.

The rapidly decaying emission seen in the TA experiments should correspond to a more delocalized initial state, possibly an intrinsic two-dimensional exciton that can exist within the herringbone crystal lattice. Several experimental observations suggest that the initial species seen in the TA data is indeed more delocalized than that seen in the

photoluminescence. First, the spectral shape of the short-lived component is consistent with a more delocalized state than seen in the photoluminescence. Previous theoretical and experimental work has shown that in J-type aggregates like crystalline tetracene, the ratio of the 0-0 and 0-1 vibronic peaks in the emission provides a sensitive measure of the exciton coherence length.[66] By fitting the 9.2 ps spectrum (from Figure 3.8b) and 80 ps spectrum (from the inset to Figure 3.5b) to a sum of two Gaussian lineshapes, we find that the 00/01 peak ratio for the 9.2 ps species is 2.3 times larger than that of the 80 ps spectrum. Thus we estimate that the short-lived species is about twice as delocalized as the average size of the 80 ps PL species, or delocalized over about 4.6 molecules at room temperature. A second indication that the species observed in the TA experiments has a higher degree of delocalization is its higher apparent emission/absorption cross section, which scales as N_{coh}, the number of molecules participating in the coherent exciton wavefunction. In the limit of low absorption samples, we can consider both the linear and nonlinear absorption properties. We define n_{mon} as the density of monomers in the crystal, with ε_{mon} being the absorption coefficient of the monomer. If the solid possesses excitons with a coherence length N_{coh}, we can estimate n_{ex}, the density of the delocalized absorbing excitons and their cross section

$$n_{ex} = \frac{n_{mon}}{N_{coh}} \tag{3.4a}$$

$$\varepsilon_{ex} = N_{coh}\varepsilon_{mon} \tag{3.4b}$$

If L is the sample thickness, we find that the absorption, a linear optical measurement, does not depend on N_{coh}:

$$A = n_{ex}\sigma_{ex}L = \left(\frac{n_{mon}}{N_{coh}}\right)\left(N_{coh}\sigma_{mon}\right)L = n_{mon}\sigma_{mon}L \tag{3.5}$$

It is straightforward to show, however, that the nonlinear pump-probe signal does reflect N_{coh}:

$$\Delta A = \sigma_{ex}^{pu}\sigma_{ex}^{pr}n_{ex}L = N_{coh}\sigma_{mon}^{pr}N_{coh}\sigma_{mon}^{pu}\frac{n_{mon}}{N_{coh}}L = N_{coh}\left(\Delta A\right)_{mon} \tag{3.6}$$

One way to think about this result is that the nonlinear ΔA signal level for the solid is higher than expected because we are probing a state with a large cross section due to superradiant enhancement of the transition dipole moment. We can estimate N_{coh} by comparing the peak ΔA signals of the monomer and solid, scaled by the pump fluence and absorption at the pump wavelength. Using Equation (6), we can derive an expression for the ratio of the ΔA signals for the solution and solid:

$$\frac{\varepsilon_{solid}}{\varepsilon_{monomer}} = \frac{\left(\Delta A\right)_{solid}}{\left(\Delta A\right)_{monomer}} \times \frac{A_{monomer}}{A_{solid}} \times \frac{I_{monomer}^{pump}}{I_{solid}^{pump}} \tag{3.7}$$

Plugging in values for the solution (peak ΔA=0.005 at 480 nm, absorption at 400 nm = 0.10, fluence = $1.5\text{x}10^{-3}$ J/cm^2) and for the solid film ((peak ΔA =0.01 at 530 nm, absorption at 400 nm = 0.05, fluence = $7\text{x}10^{-4}$ J/cm^2), we find that the ratio $\varepsilon_{solid}/\varepsilon_{monomer}$ is ~6, in reasonable agreement with the estimation of 4.6 based on the emission lineshape. It is important to emphasize that both estimates for N_{coh} are quite crude, and more precise estimates will require a more detailed theoretical analysis of the intrinsic 2-dimensional exciton states in tetracene. It is encouraging, however, that our two estimates, based on independent observables, are in decent agreement. This agreement

indicates that our picture is at least qualitatively self-consistent, even if its quantitative estimates of N_{coh} may need to be revised. Finally, a recent analysis of the absorption lineshape of tetracene single crystals, which is determined by the initially excited species observed in the TA data, suggests that there exist larger exciton delocalization lengths than what was observed in our photoluminescence experiments.[88]

While the $S_0 \rightarrow S_1$ transition can experience a superradiant enhancement in the solid state, the $S_1 \rightarrow S_N$ transitions may experience no enhancement at all. This would appear to be the case for the excited state absorption features observed in the monomer but barely visible in the solid film TA data. Since most of these transitions are expected to be polarized parallel to tetracene's long axis, they should be less susceptible to exciton coupling than the short-axis polarized transitions like $S_0 \rightarrow S_1$. Another absorption feature that would not be expected to experience superradiant enhancement in the solid is the $T_1 \rightarrow T_N$ triplet absorption. Tetracene's triplet exciton bandwidth is estimated to be on the order of 30 cm^{-1} [89], as compared to the value of ~650 cm^{-1} Davydov splitting for tetracene's singlet exciton state.[90] The weak interactions between triplet excitons means that they are localized on individual molecules at room temperature, and thus their spectroscopic properties in the crystal should be similar to those observed for isolated molecules in solution. The lack of superradiant enhancement for the triplet states is one reason why this species would be difficult to observe in the TA experiments. Its peak ε = 29,500 M^{-1} cm^{-1} has to compete with the enhanced $S_0 \rightarrow S_1$ transition, which gives rise to the dominant bleach signal.

A second, perhaps more important factor that can affect the visibility of the triplet $T_1 \rightarrow T_N$ absorption feature is the orientation of the tetracene molecules on the substrate surface. Many studies of evaporated tetracene thin films have shown that the crystallites prefer to lie with their ***ab*** plane parallel to the substrate surface. Our films are no exception, and the thickness effects on the absorption lineshape in Figure 3.2b are a direct consequence of this preferential orientation of the crystallites. This orientation problem has previously been recognized in the TA spectroscopy of pentacene thin films, but its effect on the relative magnitudes of the short-axis polarized $S_0 \rightarrow S_1$ versus the long-axis polarized $T_1 \rightarrow T_N$ signals was not quantified.[27,28] Given a transition dipole μ tilted at an angle ϕ relative to the surface normal, as shown in Figure 3.10, but which are randomly oriented in the x-y plane, one can calculate the total excitation probability assuming a dipole-field interaction:

$$P_{abs} = \frac{1-\cos(\phi)^2}{2}\mu^2 E^2 \tag{3.8}$$

If we neglect differences in line-broadening and conservatively assume that $\mu_{S0->S1} \approx \mu_{T1->TN}$ (i.e. a factor of 3 superradiant enhancement of the $S_0 \rightarrow S_1$ transition), we can use the literature value of $\phi = 21^o$ for the angle that the long axis of the tetracene molecule makes with the ***ab*** plane of the crystal[91,92], we find that

$$\frac{P_{S0->S1}}{P_{T1->TN}} = \frac{1-\cos(90^0)^2}{1-\cos(21^0)^2}\frac{\mu^2_{S0->S1}}{\mu^2_{T1->TN}} \cong 8 \tag{3.9}$$

In other words, for normal incidence light, the $T_1 \rightarrow T_N$ absorption signal is expected to be almost one order of magnitude smaller than the $S_0 \rightarrow S_1$ signal. This is probably an

optimistic estimation, since we have assumed that the angle φ in our thin films is exactly the same as that in the bulk crystal.

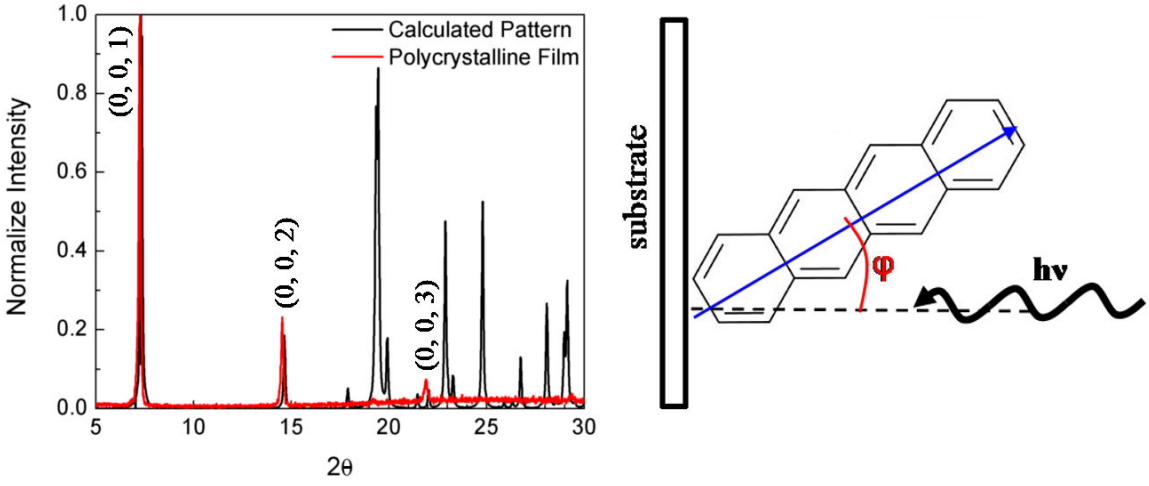

Figure 3.10 The powder XRD of a polycrystalline film (red) in comparison to the calculated powder XRD (black). The peaks in the XRD of the film correspond to the peaks in the calculated pattern that are from planes parallel to the ab plane, which means that our polycrystalline films grow with the *ab* plane parallel to the substrate and with the individual molecules aligned to be 21° (φ) from normal from the *ab* plane as shown by the literature. [92] The transition dipole moment of the triplet absorption (arrow) lies along the long molecular axis, which will interact with the excitation beam significantly less than the singlet, whose dipole moment is aligned along the short molecular axis.

In reality, the molecules on the SiO_2 surface are probably tilted even more vertically than in the bulk crystal, since it is known that the presence of a surface tends to affect the orientation of molecules within crystalline thin films. In pentacene, for example, the tilt angle can change from 19° in the bulk crystal to 5° or less for ultrathin films on a SiO_2 surface.[27,93] Similar effects have been observed for tetracene thin films on SiO_2 surfaces, although the angle φ has not been directly measured.[94-96] If we change φ from 21° to 10°, less than what is observed in pentacene, then the ratio in Equation (9) becomes 60, and the $T_1 \rightarrow T_N$ transition will be barely discernible within the experimental noise.

3.2.6 Long-delay transient absorption measurements of bleach recovery

Taken together, the superradiant enhancement of the $S_0 \rightarrow S_1$ transition and the near-normal alignment of the $T_1 \rightarrow T_N$ transition dipole serve to obscure the signature $T_1 \rightarrow T_N$ absorption. Nevertheless, it is possible to discern a rapid rise in the signal in the region around 475 nm that may reflect the population rise in the triplet state due to SF. But even if we are not able to directly observe the triplets via their excited state absorption, examination of the pump-probe signal at very long delays provides evidence for their role in the excited state dynamics. Previous work on the magnetic dependence of the DF has established that it arises mainly from triplet-triplet recombination.[48] If we assume that the DF reflects the triplet population decay, we can ask whether these triplets make up the bulk of the excited states after photoexcitation. If they do, then the decay of the bleach signal in the TA data should mirror that of the delayed fluorescence. The same samples and pump intensities were used to check this correspondence. Figure 3.11 compares the long-time decay dynamics of the bleach signal at 532 nm measured in the TA experiment and the delayed fluorescence decay measured in the PL experiments. The two decays mirror each other over the first decade of decay, with a time constant of 33 +/- 3 ns for this sample.

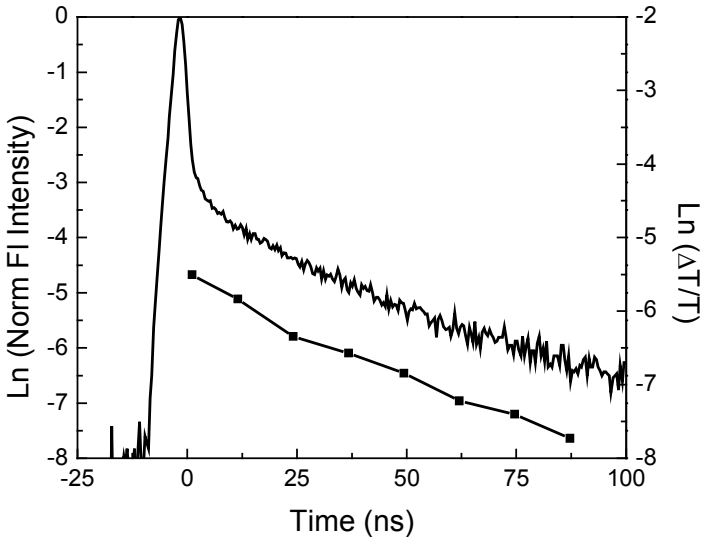

Figure 3.11 The photoluminescence decay of a 300nm thick film (solid), compared to the long time nanosecond decayof the ground state bleach (squares) of the same sample, showing a consistent time-scale for the decay between the two measurements. The fluences were 7.1×10^{-5} J cm^{-2} and 7.9×10^{-5} J cm^{-2}, respectively.

From Equation (2), we would expect the lifetime of the DF (which is proportional to N_{SI}) to be exactly half that of the bleach recovery (which is proportional to N_{TI}). However, that analysis is only valid in the absence of traps. Previous workers have shown that when the delayed fluorescence is mediated by trapping events, the simple relation in Equation (2) can break down. In the limit where traps are saturated, for example, the DF becomes quasi-first order in N_{T1} and mirrors the triplet lifetime exactly. This situation has been shown to hold for DF in both amorphous polyvinylcarbazole[97,98] and in single crystals of n-isopropylcarbazole.[99] In tetracene, Equation (2) is usually assumed to be valid but has not been experimentally confirmed. In anthracene, the closest analog to tetracene, the role of traps in DF was recognized early on.[100] However, comparison of the DF and phosphorescence lifetimes in anthracene have yielded mixed

results, with early workers seeing that Equation (2) was valid,[101] while later workers concluded that the role of trapping in DF always leads to deviations from Equation (2).[102] This would not be too surprising, since the concentration of such defects is expected to be relatively high in our evaporated films as compared to slowly grown single crystals. Since parameters like defect density, trapping rates, and triplet diffusion constants are not precisely known, we do not attempt to construct a quantitative model for these processes. Based on our results, however, it is clear that the kinetic scheme in Figure 3.4 should be modified in order to provide a consistent description of both the photoluminescence and TA data. Our modified scheme is presented in Figure 3.12.

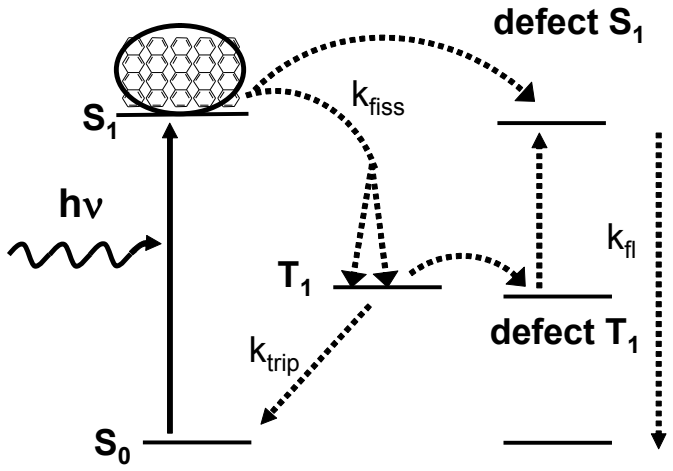

Figure 3.12 Schematic illustration of a multi-level kinetic system that includes effects of delocalization and defect sites and that is consistent with our experimental data. Note the singlet state is now delocalized over multiple molecules. Only the dominant kinetic processes are shown.

Based on the assumption that exciton-exciton annihilation is not occurring, we now postulate the existence of two distinct singlet states. The first is a highly delocalized

initial state that partitions between SF and a luminescent singlet defect within 10 ps after photoexcitation. The defect state, which is likely a minor product, then goes on to decay within 100 ps. The major product of the decay of the initial state are triplet pairs, whose lifetime can be monitored either via delayed fluorescence of the defect state or by the bleach recovery in the TA. Finally, if we take the 9.2 ps to be the formation time of the triplet pair, and the intrinsic decay time of tetracene in the absence of fission to be the solution value of 4.2 ns, we would estimate a fission yield close to 200%. After taking into exciton-exciton annihilation into account, the 80 ps formation time of the triplet pair still gives a fission yield that is very close to 200%. However, the work conducted in Chapter 4 shows that the 9.2 ps time is due to exciton-exciton annihilation, and the true formation time of triplets in tetracene is 80 ps.

3.3 Conclusion

This work begins a comprehensive study of the dynamics of tetracene at room temperature. By comparing the dynamics of monomeric tetracene to those of evaporated polycrystalline thin films, we confirm that the triplet state is produced in solution, and that it can be easily observed at long delays after the interfering singlet excited state absorption features have decayed away. In the solid state, we find that the photoluminescence decays of our evaporated thin films are well-described by previous kinetic models that were developed for single crystal tetracene. The major difference is that the triplet lifetime, as measured from the delayed fluorescence decay, is at least an order of magnitude shorter in the evaporated films than in the single crystal samples.

When broadband TA experiments are performed on the solid films, the S_1 species decays within 10 ps. The excited state $S_1 \rightarrow S_N$ and $T_1 \rightarrow T_N$ transitions seen in solution are obscured by both the superradiant enhancement of the $S_0 \rightarrow S_1$ transition and by the orientation of the crystallites which diminishes the visibility of transitions polarized along the long molecular axis. The fact that the bleach recovery parallels the delayed fluorescence decay indicates that triplets are the majority species formed by the decay of the initially excited state. Overall, our results are largely consistent with the traditional picture of SF as the dominant process in the excited state of tetracene, but show that complications like exciton delocalization, exciton annihilation, and luminescent defects must be taken into account. Attempts to use monomer spectral properties, in particular absorption coefficients, to interpret nonlinear spectroscopy measurements on strongly coupled aggregate systems must be viewed with caution. Finally, since our data is consistent with the presence of rapid SF in room temperature polycrystalline tetracene, this material may be viewed as a viable candidate for harnessing this phenomenon to increase the efficiency of organic solar cells.

CHAPTER 4

The Dependence of Singlet Exciton Relaxation on Excitation Density and Temperature in Polycrystalline Tetracene Thin Films

4.1 Introduction

In an effort to better understand the kinetics of SF in the crystalline solid, we compared the time-resolved photoluminescence and transient absorption (TA) experiments on isolated tetracene molecules in solution to those on polycrystalline thin films at room temperature in Chapter 3.[103] In that chapter, we found that the $T_1 \rightarrow T_N$ absorption that is easily observed in solution is almost unobservable in thin films. Nevertheless, we could confirm that triplets are the predominant species produced by singlet relaxation by comparing the long-time bleach recovery in the TA to the decay of the delayed fluorescence due to triplet recombination. A second issue was that the decay time of the stimulated emission in the pump-probe signal (~10 ps) was much more rapid than the decay of the photoluminescence signal (~100 ps). We attributed this discrepancy to the rapid relaxation of the initially excited singlet exciton through two channels, namely SF (major channel) and also into a luminescent defect site (minor channel), in analogy to what we had observed earlier in polycrystalline anthracene, a closely related system.[41]

The present chapter represents an effort to update our earlier conclusions and extend our measurements to lower temperatures, where the SF relaxation channel is believed to become thermally inaccessible in tetracene. There are two main goals of the

work presented in this chapter. The first goal is to examine the intensity dependence of the singlet decay, as measured by both photoluminescence and TA, in order to see if exciton-exciton annihilation provides a better explanation for the discrepancy between the two measurements seen in Chapter 3. Indeed, once we use a more sensitive technique to measure the TA dynamics over several orders of magnitude in pump pulse energy, we find that there is a strong dependence on pump fluence. The photoluminescence and TA decays are identical at excitation densities of $2x10^{17}$ cm^{-3} or less, where exciton-exciton annihilation is negligible. Thus there is no longer a need to invoke a separate photoluminescent defect site to explain the room temperature photophysics of tetracene thin films – a single species is responsible for both the photoluminescence decay and the bleach/stimulated emission signal seen in the visible region of the TA data. A second question we wanted to answer was whether the decay of the singlet is due entirely to SF. The traditional picture of SF in tetracene postulates that there exists a barrier of 1000-2000 cm^{-1} for the creation of the triplet pair state, resulting in the SF channel effectively turning off at ~150 K. We find that the rapid initial decay of the singlet persists at 77 K and 4 K, but that the delayed fluorescence disappears at lower temperatures, replaced by emission from multiple low energy species that have longer lifetimes and lead to increased "prompt" photoluminescence. Measuring the initial photoluminescence decay for different excitation wavelengths at both 298 K and 77 K provides no evidence for an energy threshold for the rapid decay at either temperature. Our results suggest that the initial decay of the singlet exciton is not thermally activated, and that an intermediate state is involved in the formation of the free triplets observed at room temperature. The

observations in this chapter extend and correct some of the conclusions of Chapter 3 and provide more detailed information on the complicated photophysics of this prototypical organic semiconductor.

4.2 Results and discussion

4.2.1 Low excitation density comparison of photoluminescence and transient absorption at room temperature

At room temperature, we first examined the intensity dependence of both the photoluminescence and TA decays. Photoluminescence is such a sensitive technique that we could easily detect the signal at very low pump fluencies, but our signal-to-noise on the spectrally resolved TA set-up limited us to measuring signals with a peak absorbance change ΔA on the order of 10^{-3} or greater in order to resolve both the short time and long time components of the signal. In Chapter 3, we analyzed data obtained using the highest fluence where the decay appeared to become independent of pump power but where the signal-to-noise was still acceptable. This approach resulted in the pulse energies used for the TA experiments being significantly higher than those used for the photoluminescence experiments. In Chapter 3, the photoluminescence decays were measured at excitation densities on the order of 10^{16} cm^{-3}, while the TA data was taken using an excitation density of $2.2x10^{19}$ cm^{-3}. It turns out that this approach was overly optimistic. In the current set of experiments, we chose a wavelength (532 nm) near the peak of the emission and then did single channel pump-probe experiments using lock-in detection and probe subtraction. This single wavelength measurement allowed us to achieve higher

signal-to-noise ratios and vary the pump pulse energy over more than 2 orders of magnitude. Figures 4.1a and 4.1b show the power-dependent singlet decays measured using both picosecond time-resolved photoluminescence and femtosecond pump-probe experiments.

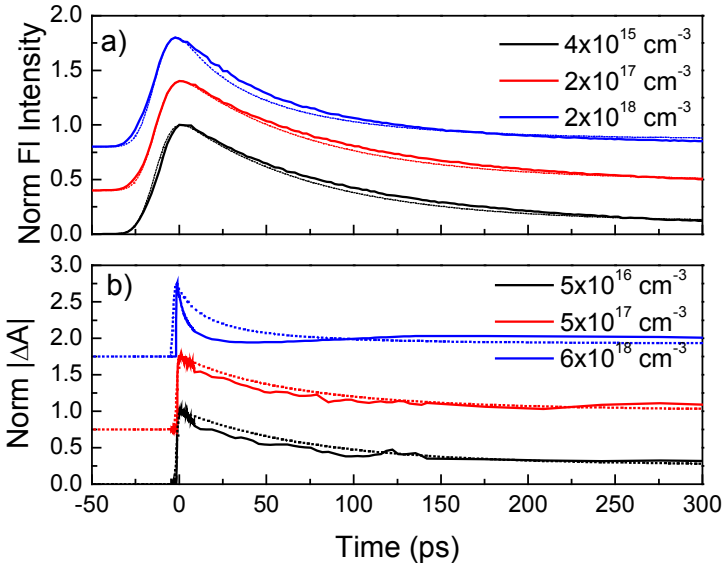

Figure 4.1 a) The time-resolved photoluminescence (solid lines) of a vacuum evaporated thin film with 400 nm excitation at $4x10^{15}$ cm^{-3} (black), $2x10^{17}$ cm^{-3} (red), $2x10^{18}$ cm^{-3} (blue) overlaid with the simulations (dashed lines) using Equation (1) in the text. The offset $y_0 = 0.05$. **b)** The intensity dependence of the single channel transient absorption (solid lines) with 400 nm excitation at $5x10^{16}$ cm^{-3} (black), $5x10^{17}$ cm^{-3} (red), $6x10^{18}$ cm^{-3} (blue) overlaid with the simulations (dashed lines) using Equation (1) in the text. The offset $y_0 = 0.3$. The kinetics become intensity independent when the excitation density is less than $2x10^{17}$ cm^{-3}. In both fits, $k_{ee} = 10$ nm^3 ps^{-1} and $k_{fiss} = 1.25x10^{-2}$ ps^{-1}. The TA signal was normalized after taking the absolute value in order to more easily compare it to the photoluminescence signal.

Both sets of data exhibit decay rates that increase as the excitation density increases, although the effect is less pronounced in the photoluminescence data in Figure 4.1a because a different laser system with lower pulse energies was used. The pump-probe data in Figure 4.1b clearly shows the effect of pulse fluence on the initial decay time, which changes from approximately 100 ps to 5 ps as the excitation density

increases from $5x10^{16}$ cm^{-3} to $6x10^{18}$ cm^{-3}. At the highest pump energies, we also observed highly damped oscillations in the signal, which we ascribe to acoustic modes in the thin film excited by the sudden heat input due to rapid exciton-exciton annihilation. In order to describe the intensity dependence of the signal over the first 300 ps, we use the expression[54,104]

$$S(t) = \left[-\frac{k_{ee}}{k_{fl}} + \left(\frac{1}{n(0)} + \frac{k_{ee}}{k_{fl}} \right) \exp\left[-k_{fl} t \right] \right]^{-1} + y_0 \qquad (4.1)$$

where $1/k_{fiss}$ = 80 ps is the intrinsic decay time of the photoluminescence which we assume is due to SF, and the exciton-exciton annihilation rate $k_{ee} = 1x10^{-8}$ cm^3 s^{-1}. These values are the same as those given in Chapter 3. The y_0 offset is necessary to take the residual TA bleach signal into account, since the ground state bleach is present even after the singlet exciton has decayed. In the photoluminescence data, the y_0 offset is necessary to take the residual delayed fluorescence signal into account. For the photoluminescence data, the decay is convolved with a Gaussian instrument response function with a full-width half-maximum of 18 ps. For the TA data, the decay is convolved with a Gaussian instrument response function with a full-width half-maximum of 300 fs. Note that this model is simpler than the multiparameter model used in Chapter 3, since we are only considering the initial decay and not the long-time dynamics of the triplets. The simulated data in Figures 4.1a and 4.1b (dashed lines) are in semi-quantitative agreement with the experimental data. This value of k_{ee} slightly overestimates the intensity dependence of the photoluminescence decay, which is better fit by $k_{ee} = 5x10^{-9}$ cm^3s^{-1}, but slightly underestimates the power dependence of the pump-probe signal. As a

compromise, we set k_{ee} = 10^{-8} cm^3s^{-1} but emphasize that this value of k_{ee} has an uncertainty factor of at least 2, mainly due to uncertainties in the calculation of the initial excitation density. This k_{ee} value is close to that measured by Fleming et al. using time-resolved photoluminescence (k_{ee} = $5x10^{-9}$ cm^3 s^{-1})[53] but a factor of 10 smaller than that obtained by Swenberg and coworkers using photoluminescence saturation.[54]

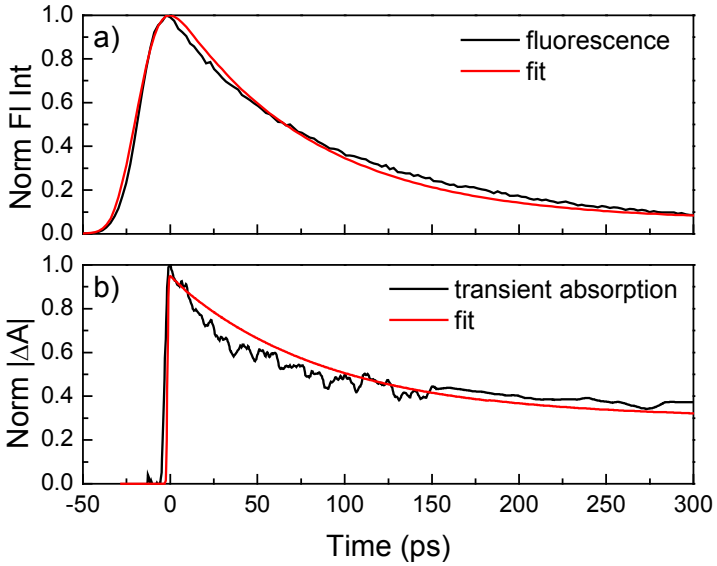

Figure 4.2 a) Time resolved photoluminescence at 298 K and an exponential fit (red) with τ_{fiss} = 80.0 ps and y_0 = 0.05. **b)** Single channel pump-probe at 532 nm and an exponential fit (red) with τ_{fiss} = 80.0 ps and y_0 = 0.3. Both experiments were done using 400 nm excitation at $3x10^{-6}$ J cm^{-2} for an excitation density of $1x10^{17}$ cm^{-3}. The TA signal was normalized after taking the absolute value in order to more easily compare to photoluminescence signal.

From a practical standpoint, only when the 400 nm pump fluence drops to $6x10^{-6}$ J cm^{-2} or below, corresponding to an excitation density of $2x10^{17}$ cm^{-1}, does the initial decay become independent of pulse energy. In Chapter 3, the TA experiments were done at 10^{-4} J cm^{-2}, which is 2 orders of magnitude higher than the fluence where exciton-exciton annihilation begins to affect the initial decay. This lower fluence corresponds to a peak ΔA signal of $5x10^{-5}$, which is below the level that can be monitored using our CCD-

based spectrally resolved TA system. It should be pointed out that in pentacene, where the SF reaction occurs within 100 fs [19,26], it is likely that exciton-exciton annihilation is not competitive with the SF rate even at high excitation densities. In tetracene, once the effect of k_{ee} is eliminated by using low excitation fluences, the photoluminescence and pump-probe decays become consistent with each other. To emphasize this fact, Figure 4.2a shows the normalized photoluminescence decay at an excitation density of 1.2×10^{17} cm^{-3}, overlaid with the signal calculated using an exponential fit with a 80 ps decay time and a y_0 offset of 0.05. Figure 4.2b shows the experimental low power pump-probe signal overlaid with the same calculated exponential decay with an offset $y_0 = 0.3$. Note that the much higher time resolution of the pump-probe experiment leads to the sharper rising edge, but the two decays after time zero are quite similar. The single exponential fit does not quite capture the earliest rapid decay of the pump-probe signal. We do not think there is residual exciton-exciton annihilation at this low fluence since varying the pump fluence within this range did not change the shape of the decay, as shown in Figure 4.3.[105]

One explanation for the more rapid decay in the TA data could be a slight shifting of the emission in the narrow pump-probe detection window that leads to a more rapid apparent decay. A variable-wavelength study of low power pump-probe spectroscopy of these tetracene films would be desirable but is beyond the scope of this paper. For the sake of simplicity, we have not introduced a biexponential fit, which would provide better agreement with the data at the expense of introducing extra parameters into the kinetic model. The main point is that the good correspondence between the low power

photoluminescence decay and the pump-probe signal at 532 nm suggests that the room temperature photodynamics are simpler than what was presented in Chapter 3. First, it is clear that a single species is responsible for both the photoluminescence decay and the visible pump-probe signal; there is no longer any reason to invoke defect photoluminescence. Second, these results demonstrate that the quantitative analysis of the photophysics requires that we take into account all the relevant processes, and that accurate determination of the singlet exciton relaxation rate requires low excitation densities (2 x 10^{17} cm^{-3} or less).

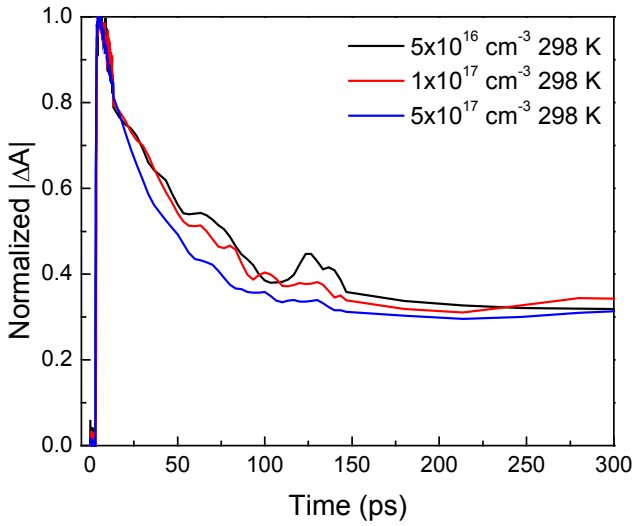

Figure 4.3 The intensity dependence of the single channel transient absorption (solid lines) with 400 nm excitation at 5x10^{16} cm^{-3} (black), 1x10^{17} cm^{-3} (red), 5x10^{17} cm^{-3} (blue). The kinetics become intensity independent when the excitation density is less than 2x10^{17} cm^{-3}. The TA signal was normalized after taking the absolute value.

4.2.2 Low temperature photoluminescence

One important question concerning the initially excited singlet is whether its relaxation pathway is dominated by the SF channel. If it is, then the yield of triplet

excitons in this material should be close to 200% as described in Chapter 3.[103] The formation of free triplets in tetracene is known to depend on temperature. Several previous workers showed that when the temperature is lowered in single crystals of tetracene, the magnetic field effect on the photoluminescence decreases, while the relative photoluminescence quantum yield increases.[23,74] These results were interpreted in terms of an activated fission rate k_{fiss}. If k_{fiss} decreases at lower temperatures, the total photoluminescence yield should increase since SF no longer competes with the radiative decay. Similarly, the sensitivity of k_{fiss} to an applied magnetic field becomes less of a factor in changing the amount of detected photoluminescence. According to this interpretation, the initial rapid decay of the singlet should disappear around 150 K. Several workers measured the photoluminescence decay of tetracene crystals at 77K, however, and found that even at this temperature, where there was no measurable magnetic field effect, a significant component of the photoluminescence still decayed on a subnanosecond timescale.[54,106,107] In light of this discrepancy, we decided to revisit these low temperature measurements in order to clarify the origin of the rapid singlet decay. Previous workers have emphasized the temperature dependence of the photoluminescence spectrum in crystalline tetracene as a way to probe exciton delocalization[42,87,108], and Voigt have analyzed the kinetics of the sub-nanosecond shifting of the initial emission at 4 K in detail.[87] None of these papers attempt to analyze their time-resolved data in terms of the SF process, which is assumed to be the dominant relaxation pathway at room temperature. A comprehensive study of the

photoluminescence dynamics on both short and long timescales, along with its implications for SF, has not been reported and is one of the main goals of this work.

We examined the spectral and temporal properties of the photoluminescence decay at different temperatures, keeping the excitation fluence well below the threshold for exciton-exciton annihilation.

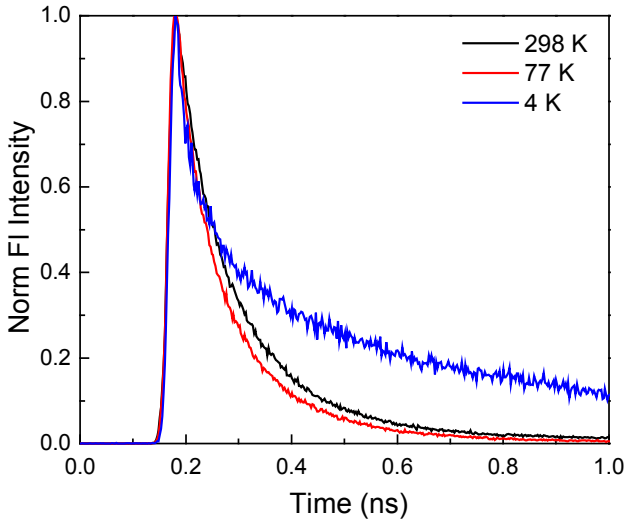

Figure 4.4 Time resolved photoluminescence of a vacuum evaporated tetracene film at 298 K (black), 77 K (red) and 4 K (blue), exhibiting a fast initial decay at all temperatures.

Figure 4.4 shows the decay of the integrated photoluminescence signal for 298 K, 77 K, and 4 K in the first nanosecond after photoexcitation. Clearly there is a rapidly decaying component (~100 ps) present at all three temperatures. After this initial decay, there is a long-lived component that persists on the order of 100 ns. The decays on longer timescales are shown in Figure 4.5 along with the biexponential fits to the decay excluding the first 10 ns. At all temperatures, the long-time decays deviate slightly from pure single exponentials, so we fit them with biexponential functions. Once the

biexponential parameters are fixed by the long time window fitting, we then fit the short time window data in Figure 4.4. The results of these fits are summarized in Table 4.1, giving a tri-exponential decay that describes the overall decay on the different timescales. The values in Table 4.1 should be taken as a parameterization of the total photoluminescence decay, and not as representing distinct physical processes.

Table 4.1

$$y = A_1 * e^{-t/\tau_1} + A_2 * e^{-t/\tau_2} + A_3 * e^{-t/\tau_3}$$

	A_1	τ_1 (ns)	A_2	τ_2 (ns)	A_3	τ_3 (ns)	% τ_1
298 K	1.00	8.00×10^{-2}	9.09×10^{-3}	1.40	1.18×10^{-2}	18.3	34.9 %
77 K	1.00	8.20×10^{-2}	1.48×10^{-2}	3.24	3.22×10^{-2}	13.3	17.2 %
4 K	1.00	1.00×10^{-1}	5.36×10^{-1}	3.64	4.87×10^{-1}	12.3	12.5 %

Table 4.1 All values have been normalized to $A_1 = 1$ in order to emphasize the relationship between the different lifetimes. τ_2 and τ_3 were fixed from the fits in Figure 4.4, and A_2 and A_3 were fixed at the ratios from those fits. τ_1 was fixed from the single exponential fits. The tri-exponential fits for these parameters can be found in Figure 4.6.

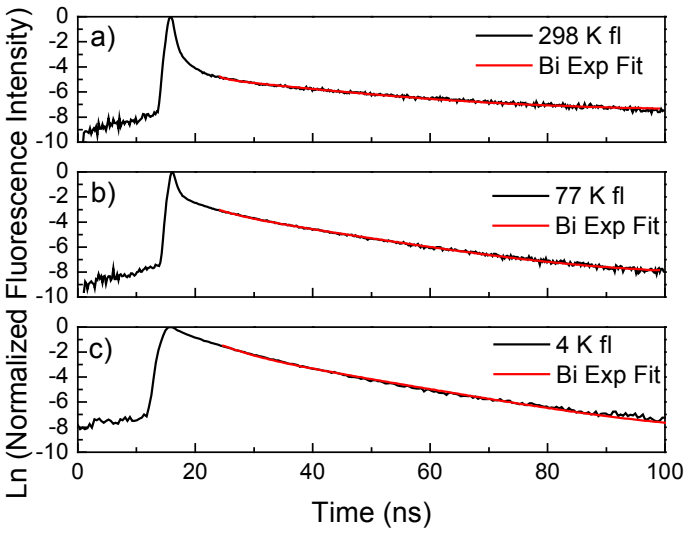

Figure 4.5 a) Time resolved photoluminescence of a vacuum evaporated tetracene film at 298 K (black) with a bi-exponential fit (red) starting 10 ns after the peak, with $\tau_1 = 1.40$ ns and $\tau_2 = 18.3$ ns. The ratio of τ_1 to $\tau_2 = 0.786$. **b)** Time resolved photoluminescence at 77 K (black) with a bi-exponential fit (red) starting 10 ns after the peak, , with $\tau_1 = 3.24$ ns and $\tau_2 = 13.3$ ns. The ratio of τ_1 to $\tau_2 = 0.459$. **c)** Time resolved photoluminescence at 4 K (black) with a bi-exponential fit (red) starting 10 ns after the peak, with $\tau_1 = 3.64$ ns and $\tau_2 = 12.34$ ns. The ratio of τ_1 to $\tau_2 = 1.10$.

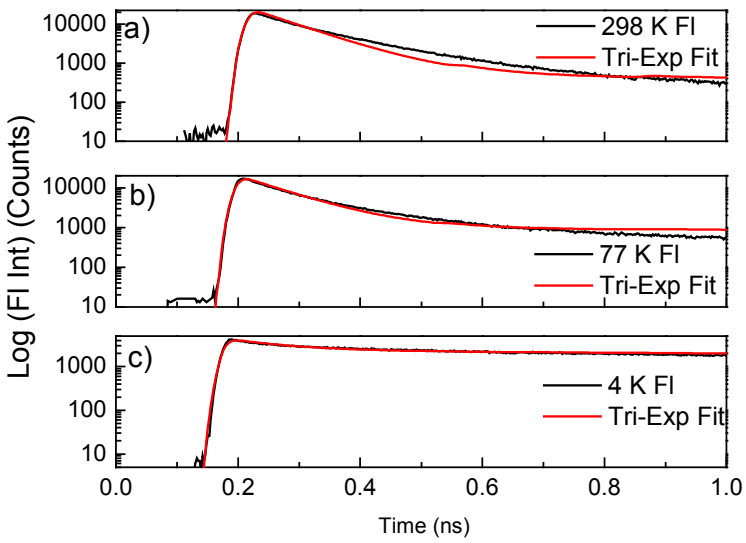

Figure 4.6 a) Tri-exponential fit (red) of 298 K integrated photoluminescence decay (black) using the values found in Table 4.1. **b)** Tri-exponential fit (red) of 77 K integrated photoluminescence decay (black) using the values found in Table 4.1. **c)** Tri-exponential fit (red) of 4 K integrated photoluminescence decay (black) using the values found in Table 4.1.

Two important observations can be taken from the data in Table 4.1. First, the persistence of the ~100 ps decay component at all temperatures, and second the increasing contribution of the long-time emission to the total photoluminescence at lower temperatures. Although it is tempting to ascribe the long-lived component of the photoluminescence decay to delayed fluorescence from the initially excited singlet, analysis of the shape of the photoluminescence spectra in different time windows shows that this is the case only at 298 K. The evolution of the room temperature emission spectra shown in Figure 4.7a for the time windows: 0-100 ps, 5-10 ns, and 50-100 ns. The normalized spectra at 298 K are indistinguishable in all three windows, despite the fact that overall decay, shown in Figure 4.5a, is clearly not a single exponential. This room temperature data was analyzed in Chapter 3, with the same conclusion as previous workers that the long-time component reflects the delayed fluorescence, where the

initially excited singlet state is regenerated by fusion of two triplets. At 77 K and 4 K, the spectral behavior is more complicated. Note that tetracene undergoes a phase transition at ~140 K[109-111] to a polymorph with slightly different angles between the molecules in the herringbone lattice. It is likely that the crystal packing at 77 K and 4 K may have a higher amount of defects than the room temperature sample but the packing motifs in the high and low temperature phases are similar enough that the overall J-type aggregate behavior is expected to dominate in both.[110,111] At 77 K, there are two dominant emitting species, shown in Figure 7b. The first, which is most pronounced in the 0-100 ps window, corresponds to the J-type aggregate emission analyzed in earlier papers.

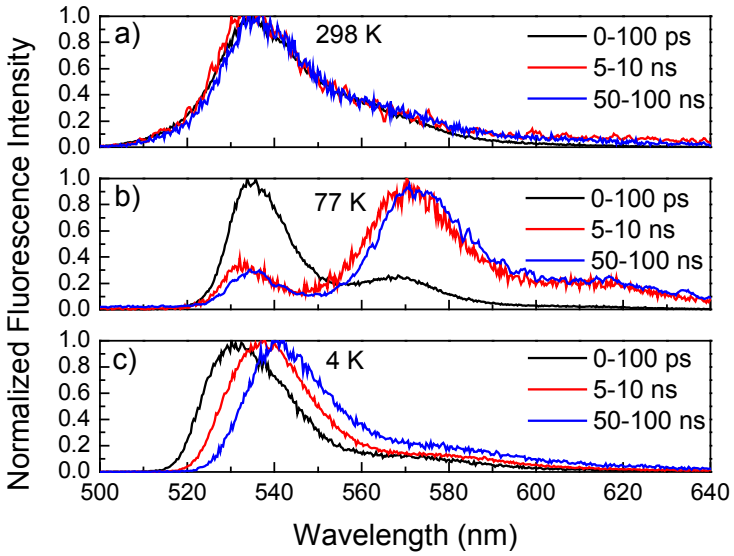

Figure 4.7 a) The photoluminescence spectra of a vacuum evaporated tetracene film at 298 K from 0-100 ps (black), 5-10 ns (red), and 50-100 ns (blue). **b)** Photoluminescence spectra at 77 K from 0-100 ps (black), 5-10 ns (red), and 50-100 ns (blue). **c)** Photoluminescence spectra at 4 K from 0-100 ps (black), 5-10 ns (red), and 50-100 ns (blue). All spectra have been normalized to the high energy 0-0 peak except for two of the 77 K spectra, which have been normalized to the 0-1 peak.

The major change in this time window is the increase of the 0-0/0-1 vibronic peak ratio, which can be attributed to an increase in the singlet exciton coherence length at lower temperatures.[66] The emission spectrum in the later time windows has a much different spectral shape, where the 0-0 peak is much smaller than the 0-1 peak. This spectral shape is similar to what is expected from an H-type aggregate.[112] This second component is much longer lived than the J-type species, but has a much lower amplitude, so that the overall photoluminescence decay in Figure 4.4 still reflects the rapid decay of the J-type emission. At 4 K, the situation again changes. In all three time windows, the spectra appear to be J-type, with the peak wavelength and 0-0/0-1 ratios steadily changing with time. In the first 500 ps, however, there is a rapid shift of the photoluminescence from 528 nm to 535 nm. This rapid 200 cm^{-1} shift was also observed by Voigt et al., and they ascribed the two different peaks to two different species, denoted F and F', that both had similar spectral shapes and sub-ns decay times.[87] Our data also show the F→F' transition, but these two species are located at slightly higher energies. We think this difference in energies reflects the different samples used in the experiments. Viogt et al. prepared ultrathin (7 nm) films on HOPG substrates, while our samples are thicker (20-30 nm) on glass or fused silica substrates. The more polarizable graphitic substrate used by Voigt et al. may result in a solvatochromic shift relative to the SiO_2 surface. But even after the F→F' transition is complete within the first nanosecond, the emission spectrum continues to evolve up to 100 ns. Figure 4.8 shows how both the peak position and the 0-0/0-1 peak ratio change with time as the photoluminescence

decays. This continuous shift suggests that we are seeing lower energy sites in the crystal with decreasing delocalization lengths as time progresses.

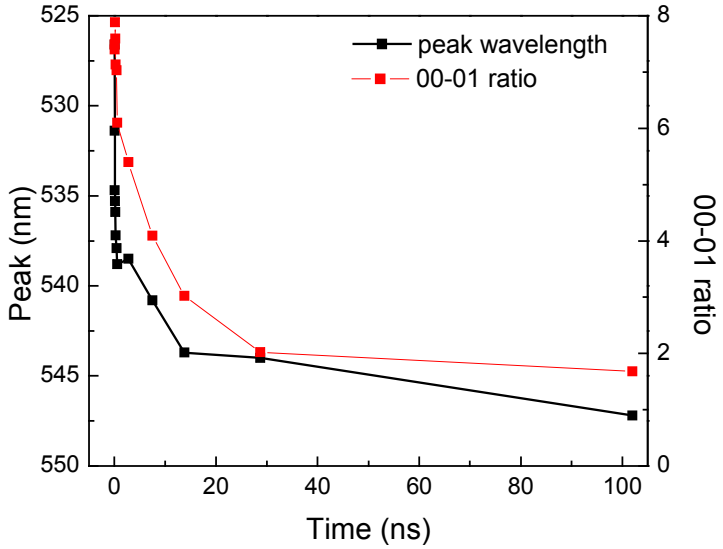

Figure 4.8 The peak wavelength of the photoluminescence spectrum of a vacuum evaporated tetracene film at 4 K, extracted from the time resolved photoluminescence, is shown in black. The 00-01 ratio of the photoluminescence spectrum at different times after excitation is shown in red.

4.2.3 Global fitting of temperature dependent photoluminescence decays and discussion of possible mechanism

The multiple emitting species observed at 77 K and 4 K could arise from two distinct mechanisms. One possibility is that in all cases a single initial state is populated by the excitation pulse, which then relaxes either by relaxation into dark states (e.g. SF) or by energy transfer to lower energy bright states. Structural defects in tetracene single crystals have been shown to give rise to a variety of different emissions, and it is likely that such defects are the origin of the different spectra seen in the 77 K and 4 K data.[87,113] If the new emissive states seen at 77 K and 4 K are populated by energy transfer from the

high energy J-type exciton, then we would expect to see the decay of the high energy spectral components to be accompanied by a rise in the low energy spectral region. Although we can try to fit the integrated photoluminescence decay using a combination of rise times and decay times[87], in general it is difficult to obtain unique solutions from a single time trace. A more robust approach is to simultaneously fit time traces at multiple wavelengths using a global linear least squares algorithm.[114,115] We performed global analysis fits for the photoluminescence signal at ten different detection wavelengths simultaneously in the 1 ns time window. The signals in all 10 windows are fit using a biexponential function where the fast decay time is fixed by the τ_1 values in Table 4.1, and the slower time is allowed to vary. Note that the long-time component is different from the long-time components given in Table 4.1. This difference is due to the different time windows analyzed for the different fits. The multi-wavelength fits and residuals can be found in Appendix 2.[105] We are mainly interested in whether the short-time fit components have both positive amplitudes (indicating population decay) and negative amplitudes (indicating population growth due to energy transfer). Figure 4.9 shows that, at all three temperatures, the global analysis finds no significant negative amplitudes at any wavelength, which indicates that the emitting species decay independently of one another. Note that at 298 K the wavelength-dependent amplitudes of the long and short time components are identical, as expected for delayed fluorescence. The lack of evidence for the low energy species gaining population from the high energy species helps rule out energy transfer as a mechanism for populating these states at 77 K. Therefore, we think that the second mechanism, formation of defect states that are

directly populated by photoexcitation and decay independently, is the dominant mechanism that explains the additional photoluminescence at 77 K and 4 K.

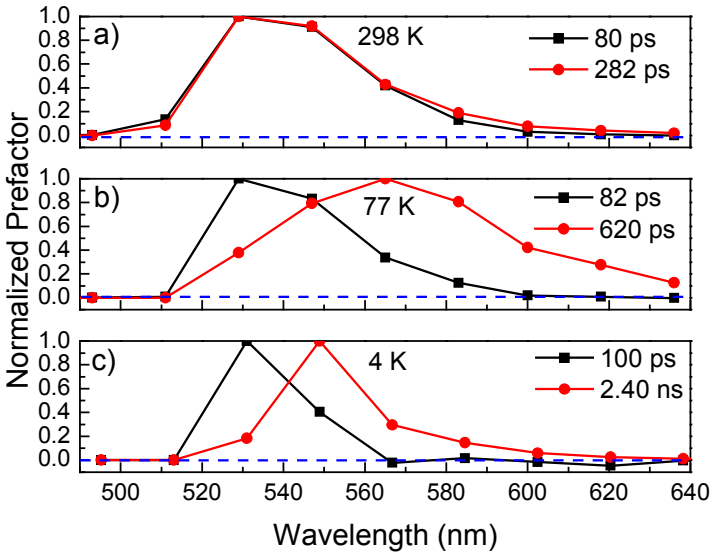

Figure 4.9 a) Normalized prefactors for a global analysis fit to the 298 K photoluminescence with lifetimes of 80.0 ps (black) and 282 ps (red). **b)** Normalized prefactors for a global analysis fit to the 77 K photoluminescence with lifetimes of 82.0 ps (black) and 620 ps (red). **c)** Normalized prefactors for a global analysis fit to the 4 K photoluminescence with lifetimes of 100 ps (black) and 2.40 ns (red).

The 0-100 ps spectra in Figures 4.7a, 4.7b and 4.7c show that the same delocalized exciton is responsible for the early-time emission at all temperatures. The decays in Figure 4.4 show that the rapid initial decay of this species is also present at all temperatures. In order to make sure that our photoluminescence measurements are not overlooking some new species being formed at low temperatures, we also examined the transient absorption data at 77 K. The presence of a rapid singlet decay channel at 77 K is confirmed by our pump-probe data. We have found that higher pump energies affect only the exciton-exciton annihilation rate and not the overall spectral shape. To obtain good signal-to-noise transient spectra, we measure them using 2×10^{-4} J cm^{-2}, a factor of

30 higher than the threshold for exciton-exciton annihilation. In Figure 4.10 we present the early (100 fs) and later (1.75 ns) time spectra for tetracene thin films at both 298 K and 77 K. The two sets of spectra are remarkably similar, with the same pattern of peaks at both temperatures. As with the early time photoluminescence spectra in Figure 4.7, the 0-0 vibronic peak of the stimulated emission becomes more pronounced at 77 K as the effective cross section increases due to the exciton's larger coherence length. This enhanced TA signal at lower temperature is basically a signature of the superradiant singlet exciton deduced previously based on temperature-dependent absorption[88] and photoluminescence measurements.[42,87,108] Due to the high fluence and possible complications from overlapping excited state absorption, we have not attempted to perform a global analysis of the TA kinetics. The key point of Figure 4.10 is that there is no significant change in the TA spectrum, despite the assumption that at 77 K the SF pathway is quenched.

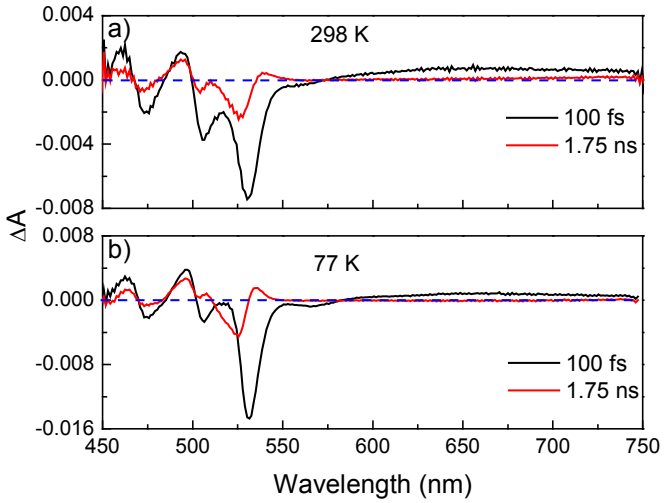

Figure 4.10 a) Broadband transient absorption at 298 K at 100 fs (black) and 1.75 ns (red) delays. **b)** Broadband transient absorption at 77 K at the same delays. The pump pulse fluence was $2x10^{-4}$ J cm^{-2} at 400 nm, corresponding to an excitation density of $6x10^{18}$ cm^{-3}, which is above the threshold of exciton-exciton annihilation.

Thus far we have used only 400 nm excitation pulses, and we now consider the possibility that the excess energy at this wavelength overcomes the activation barrier for SF at all temperatures. If this is the case, then the similarity between the initial singlet decays at the different temperatures would not be surprising, since the hot singlet would decay by SF even at low temperatures. Early studies of the photoluminescence action spectrum suggested that at least some SF could occur via unrelaxed vibronic states[49,116], and Thormsølle et al. identified two different singlet relaxation rates that they ascribed to two different SF pathways from hot and relaxed states.[51] A mechanism based on nonequilibrium vibronic states might also help explain recent results on enhanced triplet formation using shaped femtosecond pulses.[50] But if this excess excitation energy is an important factor for the ability of the singlet exciton to undergo SF, then we would expect that its decay rate should be quite sensitive to the wavelength used to excite the sample. The energy of the singlet state is generally fixed at ~18680 cm^{-1} (535 nm), while the energy of the triplet pair, taken as twice the energy of a free triplet, is 20200 cm^{-1} (498 nm).[117] This energy level spacing results in an activation energy for SF of 1520 cm^{-1}, although other estimates range from 1000-2000 cm^{-1}.[23,48,74,118] In any case, based on these energies we would expect to see a threshold for the SF decay channel at around an excitation wavelength λ_{ex} = 500 nm. This threshold should be more pronounced at lower temperatures, where there is less thermal energy to convolve with the excess energy from photoexcitation. In Figure 4.11a we show the 298 K photoluminescence decays for λ_{ex} = 400 nm (25000 cm^{-1}), 480 nm (20800 cm^{-1}) and 510 nm (19500 cm^{-1}). In Figure 4.11b we show the same decays at 77 K. All the decays are rapid, on the order of 100 ps at

both temperatures and there is no dependence on λ_{ex} to within the experimental noise. We see no sign of the expected threshold behavior for the fast SF decay at either temperature. The conclusion is that the kinetics observed after excitation at 400 nm are identical to those obtained using other excitation energies much closer to the band edge. Excess photon energy does not explain the observation of a fast singlet decay at low temperature where the SF mechanism had been assumed to be inoperative. This measurement establishes that the singlet decay does not depend on excitation energy, in contrast to the expectation based on a simple model of SF as an activated rate process.

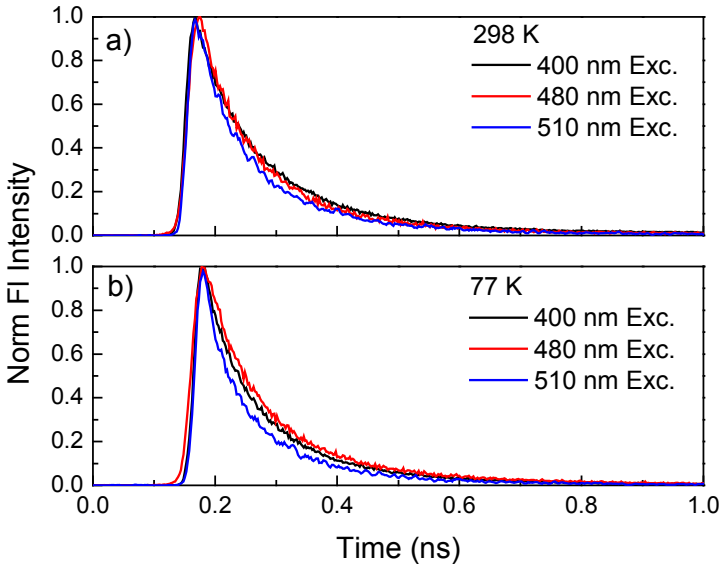

Figure 4.11 a) The time resolved photoluminescence of a vacuum evaporated tetracene film at 298 K with the excitation wavelength at 400 nm (black), 480 nm (red), and 510 nm (blue). **b)** The time resolved photoluminescence of the same film at 77 K, also using 400 nm (black), 480 nm (red), and 510 nm (blue) excitation wavelengths. The 510 nm excitation photoluminescence is integrated from 525-640 nm instead of 500-640 nm to minimize distortions from the scattered excitation while still maintaining acceptable signal-to-noise levels.

The crystallinity of tetracene thin films has been confirmed by x-ray diffraction and electron microscopy studies.[24,119] The similarity of the photoluminescence spectra to

those of single crystal samples[108,120,121] provides additional evidence that there are not significant differences in crystal packing or the electronic states between single crystal samples and evaporated polycrystalline thin films. Thus we are confident that our spectroscopic measurements are representative of the dynamics of the singlet exciton in crystalline tetracene, and not an artifact of our preparation method. Our analysis of the temperature-dependent photoluminescence dynamics of polycrystalline tetracene thin films leads to two main conclusions. The first point is that any interpretation of the photoluminescence intensities must take into account the different species that contribute to the photoluminescence signal at lower temperatures. At 77 K, the long-lived species appear to have H-type character, as judged from the small 0-0/0-1 vibronic peak ratio. It is possible that these emitters are associated with disordered sites within a crystal that has not yet completed its phase transition. If some tetracene molecules become parallel in isolated regions of the crystal as it undergoes its phase transition, the exciton character could switch from J-type to H-type. Such switching has been observed previously in anthracene pairs[122], so there is precedence for both types of emission from aggregated polyacenes. At 4 K, all emission is J-type, possibly because at this temperature all the sites that give rise to H-type emission at 77 K have presumably settled into the low-temperature polymorph structure. The interesting thing about the 4 K data is that only the high energy, delocalized J-type emitters decay via the 100 ps channel. The lower energy species can be much longer lived, like the H-type emitters at 77 K. The heterogeneous nature of the tetracene photoluminescence at lower temperatures, possibly resulting from disorder induced by the solid-state phase transition, means that earlier assumptions that

the low temperature "prompt" photoluminescence originates from the same singlet exciton that dominates the high temperature photoluminescence may need to be revisited. We do find higher yields of "prompt" photoluminescence at lower temperatures, but this additional photoluminescence originates from the appearance of additional independent emitters, and not the closure of the ~100 ps decay channel that is ascribed to SF at room temperature. This observation leads to the second main point: that the initially excited J-type singlet exciton decays on the ~100 ps timescale at all temperatures. Since it is reasonably well-established that triplets are the dominant products of the singlet decay at room temperature, the question is why the ~100 ps singlet decay, even where other types of experiments seem to show that SF is not occurring. One possibility is that as the temperature is lowered, another relaxation mechanism turns on as SF turns off, but the identity of this relaxation channel, the origin of its anomalous temperature dependence, and its fortuitous ability to exactly balance the decrease in the SF rate are all unclear. The existence of the long-time bleach at 77 K rules out internal conversion to the ground state, for example.

A more reasonable alternative is that the same process is occurring at all temperatures that causes the rapid singlet decay. This process eventually leads to free triplet excitons at room temperature but not at lower temperatures. In fact, the standard reaction scheme that has been used previously to interpret the magnetic field dependent experiments postulates a two-step process[117,123-125]

$$S_1 \underset{k_2}{\overset{k_{-2}}{\rightleftarrows}} (T_1T_1) \underset{k_1}{\overset{k_{-1}}{\rightleftarrows}} T_1 + T_1 \tag{4.2}$$

where the rates are labeled to be consistent with earlier notation.[117] In this model, the initial creation of a delocalized S_1 exciton is followed by rapid (~100 ps) relaxation into a dark state consisting of a bound triplet pair (T_1T_1). The existence of such a state has been suggested by several theoretical calculations on pentacene[29,39]. The computational evidence for such states in a closely related system suggests that they could also exist in tetracene, although the triplet-singlet energy gap is quite different in the two systems. The production of coherently coupled triplet pairs has also been inferred from the observation of oscillations in the delayed fluorescence.[55,56] An alternate candidate for a dark intermediate state would be a charge-transfer state that has been postulated to play a role in SF.[14,126] The charge-transfer states of tetracene that have been identified through electroabsorption spectroscopy are higher in energy than the Frenkel exciton[127,128], but it is possible that rapid lattice distortion after singlet excitation leads to a dark state with charge-transfer character.[28] However, there is no sign of this state at 77 K as either a long-lived induced absorption in the transient absorption or in the form of excimer emission. In either case, if formation of the intermediate state is the origin of the ~100 ps singlet decay, then it would have to be formed through a barrierless pathway in order to explain the lack of temperature dependence. Once this dark intermediate state is formed, the SF process is still not complete, since this bound pair must still dissociate into free triplet excitons. If this dissociation is thermally activated, then the production of free triplets is curtailed at low temperatures, but not the initial formation of the bound pair. The picture that emerges is that the intermediate state must be lower in energy than S_1 and also the free triplet pair T_1+T_1.

4.3 Conclusions

After analysis of the pump-probe decay dynamics over two orders of magnitude of pump energy, we have revised the conclusions of Chapter 3 as to the role of photoluminescent defect states. At excitation densities below the threshold for exciton-exciton annihilation, we find that the pump-probe and photoluminescence decay rates are in quantitative agreement. The disagreement between the two experiments in Chapter 3 resulted from the use of very different pump fluences, and not from the presence of rapidly formed emissive defect states. This result simplifies the interpretation of the room temperature dynamics, since we no longer have to invoke two different singlet species to explain the dynamics. We find that as the temperature is lowered, additional long-lived emitting species appear that increase the total amount of photoluminescence, but that the fast decay of the initially excited J-type exciton persists at all temperatures. To explain the persistence of the rapid singlet decay, combined with the disappearance of the delayed fluorescence at low temperatures, we adopt the two-step kinetic model used by earlier workers to analyze magnetic field effects. If the dissociation into free triplets is thermally activated, while formation of the intermediate state is not, we can provide at least a qualitative explanation for the persistence of the ~100 ps singlet exciton decay at all temperatures. Although we postulate that this intermediate state could be either a bound triplet pair or a charge-transfer state, its character has yet to be determined.

CHAPTER 5

Quantum Beats in Crystalline Tetracene Delayed Fluorescence due to Triplet Pair Coherences Produced by Direct Singlet Fission

5.1 Introduction

Crystalline tetracene has long served as a prototypical SF material.[18] In previous work, the observation of the triplets formed by SF in tetracene has relied on the detection of electron spin resonance signals[44-47] and magnetic field effects on both photoluminescence[22,23,43] and device performance.[129] Transient absorption experiments on crystalline tetracene and pentacene[19,27,50,51 ,52] have provided valuable information the excited state dynamics, although the assignment of various spectral features can be complicated.[26,86,130] The indirect observation of triplet dynamics using the delayed fluorescence (DF) signal can also provide a wealth of valuable information about triplet dynamics, as illustrated by the work by Chabr et al.[55,56] Their observation of quantum beats in the DF signal corresponding to the energy levels of the triplet pair provided direct proof of the formation of triplet pair superposition states through the SF process. Their work concentrated on the behavior of samples in high magnetic fields and the relatively low signal-to-noise ratio made it difficult to reliably measure quantities like damping times. Also, a model that could quantitatively describe both the excitation and decoherence of the oscillations required a density matrix treatment, which was not performed. In the current chapter, we revisit that work in an effort to clarify both the origin and the dynamics of the quantum beats observed in the DF in the absence of a magnetic field. We find that they are a general phenomenon, present in both single

crystals and evaporated thin films, and that they exhibit a strong temperature dependence. We develop a hybrid coherent-incoherent density matrix model that involves the direct creation of a coherent superposition of triplet pair states via incoherent relaxation of the initially excited singlet state. This model does a good job of reproducing both the overall photoluminescence decay shape, the relative Fourier amplitudes of the oscillations, and their damping. It does not require the existence of an intermediate state or electronic coherence between the singlet and triplet manifolds. Lastly, our modeling indicates that magnetic dipole-dipole interactions between the two triplets created by SF are small. This suggests that the triplets must either reside on non-nearest neighbor molecules, or are moving so rapidly that the dipole-dipole interaction is averaged to zero. The results in this chapter help clarify the dynamics of SF in crystalline tetracene and provide a starting point for the development of more sophisticated models for this process.

5.2 Results and discussion

5.2.1 Delayed fluorescence oscillations in single crystals and thin films

Figures 5.1a and 5.1b show the log-plots of the photoluminescence decays for both an ultrathin solution-grown single crystal and a polycrystalline thin film grown by vacuum evaporation. Both samples clearly exhibit ripples in the DF signal, although they are more pronounced in the single crystal data. In general, the visibility of the oscillations showed some variability from sample to sample, with the single crystals consistently showing higher visibility oscillations.

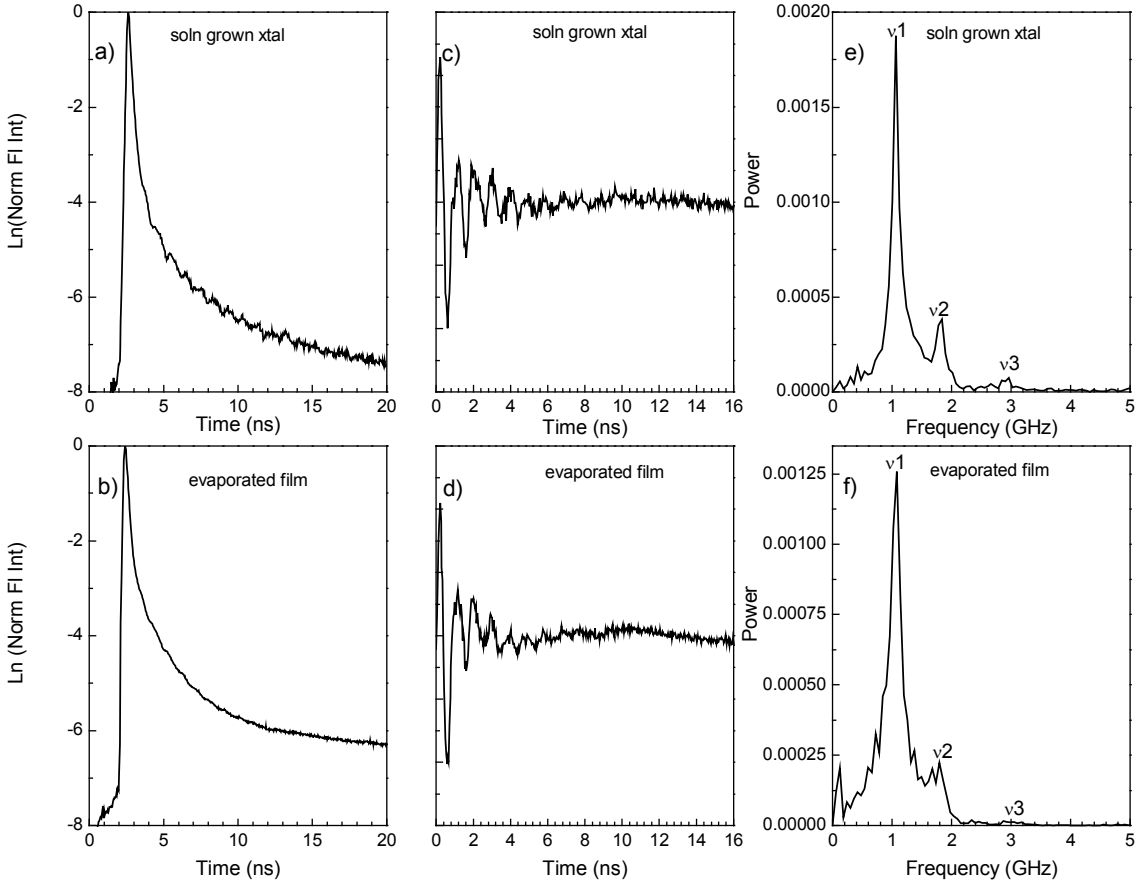

Figure 5.1 a) Time resolved photoluminescence of a solution grown single crystal of tetracene. **b)** Time resolved photoluminescence of a vacuum evaporated polycrystalline tetracene film. **c)** Oscillations extracted from the photoluminescence decay of a solution grown single crystal shown in **a)** by subtracting off an exponential fit. **d)** Oscillations extracted from the photoluminescence decay of a vacuum evaporated polycrystalline tetracene film shown in **b)** by subtracting off an exponential fit. **e)** The Fourier transform of the extracted oscillations of the single crystal from **c)** with peaks at 1.06 ± 0.05, 1.83 ± 0.05 and 2.92 ± 0.06 GHz. **f)** The Fourier transform of the extracted oscillations of the polycrystalline film from **d)** with peaks at 1.08 ± 0.05, 1.80 ± 0.05 and 2.99 ± 0.08 GHz.

When the photoluminescence background is fit to a multiexponential and subtracted from the raw data, we can isolate the oscillatory component of the signal, as shown in Figures 5.1c and 5.1d. Both types of samples show similar frequencies and

damping times. This can be seen most clearly from the Fourier power spectra of the data, which are shown in Figures 5.1e and 5.1f. In the spectrum of the single crystal in Figure 5.1e, we can discern three frequencies which we denote $\nu_1 = 1.06 \pm 0.05$ GHz, $\nu_2 = 1.82 \pm 0.05$ GHz, and $\nu_3 = 2.92 \pm 0.06$ GHz. The noisier spectrum of the film in Figure 5.1f clearly shows ν_1, but the limited signal-to-noise makes it more difficult to discern features at ν_2 and ν_3. These three characteristic frequencies ν_1, ν_2 and ν_3 were observed with the same relative amplitudes for all samples studied, although the overall oscillation visibility varied between samples. The same oscillations were observed in the DF using excitation at either 400 nm or 500 nm at room temperature. This lack of sensitivity to excess excitation energy is consistent with our previous results on the photoluminescence decay dynamics of these samples.[131]

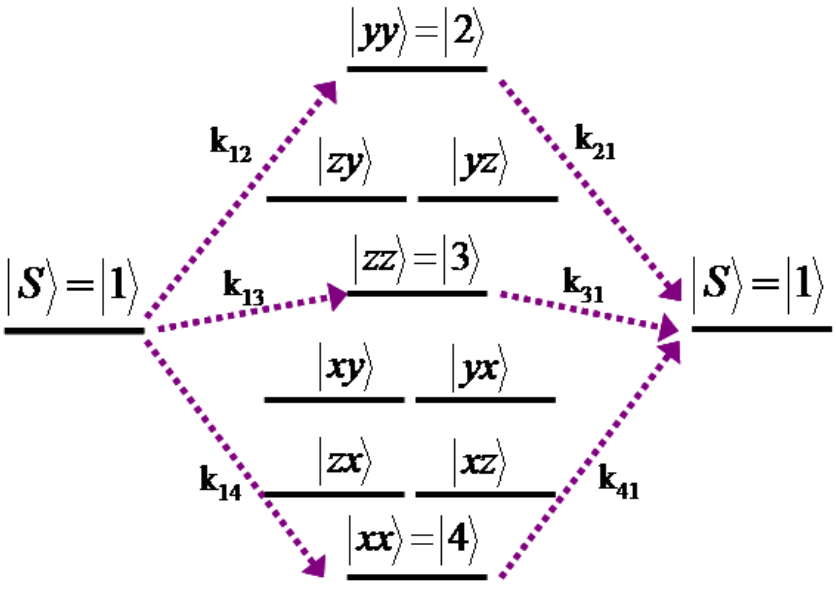

Figure 5.2 Schematic diagram illustrating the fission (k_{1n}) and fusion (k_{n1}) between the singlet state and the 9 triplet pair states, which is the basis of the density matrix treatment described in the text.

5.2.2 Simulation of delayed fluorescence dynamics using density matrix approach

In order to quantitatively understand the origin of the dynamics seen in Figure 5.1, we first develop a model based on the density matrix description. In accordance with previous workers, we assume that the initially excited singlet state directly couples to the 9-state basis of triplet pair states. This is shown schematically in Figure 5.2. We use the zero-field basis $|x\rangle_A$, $|y\rangle_A$, and $|z\rangle_A$ that are the eigenstates for the zero-field Hamiltonian for an isolated triplet on site A.[132] In the 4-electron system, the singlet state can be written as a superposition of the triplet pair states in the zero-field basis.[117,123]

$$|S\rangle = \frac{1}{\sqrt{3}}\left(|xx\rangle + |yy\rangle + |zz\rangle\right) \tag{5.1}$$

This nonstationary superposition state is expected to give rise to quantum beats at frequencies corresponding to the energy differences between the states. If there is no interaction between the triplets, the Hamiltonian is already diagonal in the zero-field basis and the stationary states are just the simple product states energies $|xx\rangle$, $|xy\rangle$, etc. The energies of the three states with singlet character, as deduced from Equation (5.1), are

$$E_{xx} = 2E_x = 2\left(\tfrac{1}{3}D^* - E^*\right) \tag{5.2a}$$

$$E_{yy} = 2E_y = 2\left(\tfrac{1}{3}D^* + E^*\right) \tag{5.2b}$$

$$E_{zz} = 2E_z = 2\left(-\tfrac{2}{3}D^*\right) \tag{5.2c}$$

where D* and E* are the zero-field parameters for the crystal that can be obtained from EPR measurements.[47] The three possible energy differences, xx-yy, xx-zz, and yy-zz

provide the possible quantum beat frequencies. Using D*= -0.0062 cm^{-1} and E*= 0.0248 cm^{-1}, we find

$$E_{xx}\text{-}E_{yy} = 0.0992\ cm^{-1} = 2.98\ GHz \quad (5.3a)$$

$$E_{xx}\text{-}E_{zz} = 0.0620\ cm^{-1} = 1.86\ GHz \quad (5.3b)$$

$$E_{yy}\text{-}E_{zz} = 0.0372\ cm^{-1} = 1.12\ GHz \quad (5.3c)$$

The calculated difference frequencies given in Equations (5.3a-c) are all slightly higher than the frequencies extracted from the experimental Fourier transforms, but the close correspondence suggests that this analysis is on the right track.

While a simple analysis of the state energies allows us to predict the quantum beat frequencies, a full density matrix treatment is required to understand the relative amplitudes and damping of the oscillations. In principle, such an analysis must describe the dynamics of the 10 coupled states (9 triplet pair plus one singlet). The simplifying assumption in all theories of SF and DF is that the transition rate from the singlet to the triplet manifold is proportional to the overlap of the stationary triplet pair states and the singlet wavefunction given in Equation (5.1). Thus we can assume that only the stationary triplet pair states with singlet character can participate in the SF/DF process. Typically there are only 3 such states, which we denote as 2, 3, and 4 with the singlet state denoted as state 1. From Equation (5.1), in the absence of the triplet-triplet interaction terms, states 2-4 correspond to $|xx\rangle$, $|yy\rangle$ and $|zz\rangle$, as shown in Figure 5.2. We then write a Hamiltonian that includes an explicit coupling between states 1 and states 2-4:

$$\hat{H} = \sum_{n=2}^{4} |n\rangle \varepsilon_n \langle n| + |n\rangle M_{n1} \langle 1| + |1\rangle M_{1n} \langle n| \tag{5.4}$$

The energy of the initial singlet state $|1\rangle$ is set to 0, and the M_{1n} elements represent transition matrix elements that couple this state to the triplet pair states. In the following analysis, we will assume that the M_{1n}'s are real numbers, i.e. M_{1n}=M_{n1}. Setting $\hbar$=1 and solving the Liouville equation with this Hamiltonian gives rise to first order differential equations of the form

$$i\frac{\partial \rho_{11}}{\partial t} = -k_{rad}\rho_{11} + M_{12}\rho_{21} + M_{13}\rho_{31} + M_{14}\rho_{41} - M_{21}\rho_{12} + M_{31}\rho_{13} + M_{41}\rho_{14} \tag{5.5a}$$

$$i\frac{\partial \rho_{12}}{\partial t} = M_{12}\rho_{22} + M_{13}\rho_{32} + M_{14}\rho_{42} - M_{12}\rho_{11} - \varepsilon_2\rho_{12} - \frac{i}{T_{2TS}}\rho_{12} \tag{5.5b}$$

$$i\frac{\partial \rho_{22}}{\partial t} = -k_{trip}\rho_{22} + M_{21}\rho_{12} - M_{12}\rho_{21} \tag{5.5c}$$

$$i\frac{\partial \rho_{33}}{\partial t} = (\varepsilon_2 - \varepsilon_3)\rho_{33} + M_{21}\rho_{13} - M_{13}\rho_{21} - \frac{i}{T_{2TT}}\rho_{23} \tag{5.5d}$$

Equations (5.5a-d) give representative examples of the relevant terms: ρ_{11} represents the population in singlet state $|1\rangle$, ρ_{nn} represents the population in triplet pair state $|n\rangle$, and ρ_{1n} and ρ_{nm} represent coherences between $|1\rangle$ and $|n\rangle$ and $|n\rangle$ and $|m\rangle$ states, respectively. Note that in Equations (5.5a-d) we have added four phenomenological relaxation rates: k_{trip} is the population relaxation out of the triplet pair state that does not go back to the singlet; k_{rad} is the radiative decay rate of the singlet state, T_{2TS} describes the electronic dephasing between the states in the triplet manifold and the singlet state,

and T_{2TT} describes the dephasing between triplet pair states. Consideration of all four states leads to a system of 16 coupled differential equations. The situation can be simplified somewhat if we assume that the singlet-triplet dephasing time T_{2TS} is much shorter than any other timescale in the problem. In this case, we can explicitly write the solution of the off-diagonal coherence terms like ρ_{12} as

$$\rho_{12}(t) = \int_{-\infty}^{t} dt' \exp\left[\left(i\varepsilon_2 - \frac{1}{T_{2TS}}\right)(t-t')\right] i\left(M_{12}\rho_{11}(t') - M_{12}\rho_{22}(t') - M_{13}\rho_{32}(t') - M_{14}\rho_{42}(t')\right) \tag{5.6}$$

As T_{2TS} becomes very small, we can take the limit

$$\lim_{T_{2TS}\to 0} \frac{1}{2T_{2TS}} \exp\left[\frac{-t}{T_2}\right] = \delta(t) \tag{5.7}$$

We find that

$$\rho_{12}(t) = iT_{2TS}\left(M_{12}\rho_{11}(t) - M_{12}\rho_{22}(t) - M_{13}\rho_{32}(t) - M_{14}\rho_{42}(t)\right) \tag{5.8}$$

The technique of letting $T_{2TS}\rightarrow 0$ to eliminate electronic coherences has been used previously to generate rate equations from the density matrix to describe rate processes in optical processes.[133,134] Physically, it means that the electronic coherences follow the population differences exactly and go immediately to zero in the absence of such a difference. Note that by taking this limit of rapid electronic dephasing between the singlet and triplet manifolds, we are considering SF to be an incoherent process with respect to the singlet→triplet transition. This is in contrast to the situation in pentacene, where recent time-resolved photoemission experiments have indicated the existence of an

electronic coherence between the singlet and a multiple exciton state.[135] But it should be emphasized that our incoherent rate process can still generate electronic coherences between the triplet pair states. This type of phenomenon, where rapid electronic relaxation processes generate spin coherences, has been observed previously for both intersystem crossing and chemically reactive systems.[136,137] The validity of this approximation can be judged by whether the resulting calculations provide an accurate description of the data. We plug this new expression for ρ_{12}(t) back into the other differential equations for ρ_{11} and ρ_{nm} in order to obtain a new system of 10 coupled differential equations:

$$\frac{\partial \rho_{11}}{\partial t} = -\left(k_{rad} + k_{12} + k_{13} + k_{14}\right)\rho_{11} + k_{12}\rho_{22} + k_{13}\rho_{33} + k_{14}\rho_{44} + \sqrt{k_{12}k_{13}}\left(\rho_{23} + \rho_{32}\right) + \sqrt{k_{12}k_{14}}\left(\rho_{24} + \rho_{42}\right) + \sqrt{k_{14}k_{13}}\left(\rho_{34} + \rho_{43}\right) \tag{5.9a}$$

$$\frac{\partial \rho_{22}}{\partial t} = k_{12}\rho_{11} - k_{trip}\rho_{22} - k_{12}\rho_{22} - \tfrac{1}{2}\sqrt{k_{12}k_{13}}\left(\rho_{23} + \rho_{32}\right) - \tfrac{1}{2}\sqrt{k_{12}k_{14}}\left(\rho_{24} + \rho_{42}\right) \tag{5.9b}$$

$$\frac{\partial \rho_{23}}{\partial t} = \left(i\varepsilon_{32} - \frac{1}{T_{2TT}} - \frac{k_{12}}{2} - \frac{k_{13}}{2}\right)\rho_{23} + \tfrac{1}{2}\sqrt{k_{13}k_{12}}\left(2\rho_{11} - \rho_{22} - \rho_{33}\right) - \tfrac{1}{2}\sqrt{k_{13}k_{14}}\rho_{42} - \tfrac{1}{2}\sqrt{k_{12}k_{14}}\rho_{34} \tag{5.9c}$$

where the population transfer rates k_{1n} are given by

$$k_{12} = 2T_{2TS}M_{12}^2 \tag{5.10a}$$

$$k_{13} = 2T_{2TS}M_{13}^2 \tag{5.10b}$$

$$k_{14} = 2T_{2TS}M_{14}^2 \tag{5.10c}$$

From a physical standpoint, the problem with Equations (5.9a-c) is that the rate of transfer forward (fission) is equal to the rate of transfer backward (fusion), which is not consistent with our physical observations. To fix this problem, we make an *ad hoc* assumption that the population decay rates from 1→n and n→1 are not equal. Furthermore, we assume that the population dephasing of the ρ_{nm} terms arises only from population loss, rather than gain. We now have

$$\frac{\partial \rho_{11}}{\partial t} = -\left(k_{rad} + k_{12} + k_{13} + k_{14}\right)\rho_{11} + k_{21}\rho_{22} + k_{31}\rho_{33} + k_{41}\rho_{44} + \sqrt{k_{21}k_{31}}\left(\rho_{23} + \rho_{32}\right) + \sqrt{k_{21}k_{41}}\left(\rho_{24} + \rho_{42}\right) + \sqrt{k_{41}k_{31}}\left(\rho_{34} + \rho_{43}\right) \tag{5.11a}$$

$$\frac{\partial \rho_{22}}{\partial t} = k_{12}\rho_{11} - \left(k_{21} + k_{trip}\right)\rho_{22} - \tfrac{1}{2}\sqrt{k_{21}k_{31}}\left(\rho_{23} + \rho_{32}\right) - \tfrac{1}{2}\sqrt{k_{21}k_{41}}\left(\rho_{24} + \rho_{42}\right) \tag{5.11b}$$

$$\frac{\partial \rho_{23}}{\partial t} = \left(i\varepsilon_{32} - \frac{1}{T_2^{(23)}}\right)\rho_{23} + \sqrt{k_{13}k_{12}}\,\rho_{11} - \tfrac{1}{2}\sqrt{k_{31}k_{21}}\left(\rho_{22} + \rho_{33}\right) - \tfrac{1}{2}\sqrt{k_{31}k_{41}}\,\rho_{42} - \tfrac{1}{2}\sqrt{k_{21}k_{41}}\,\rho_{34} \tag{5.11c}$$

where

$$\frac{1}{T_2^{(23)}} = \frac{1}{T_{2TT}} + \frac{k_{21}}{2} + \frac{k_{31}}{2} \tag{5.12}$$

is now the effective dephasing rate for the ρ_{23} coherence that takes population relaxation into account. Note that the only difference between Equations (5.9a-c) and Equations (5.11a-c) is the change in subscripts on the rate constants for population transfer into versus out of a given state, i.e. $k_{1n} \neq k_{n1}$. We can now solve this system of equations given the initial conditions $\rho_{11}(t=0)=1$ and $\rho_{nm}(t=0)=0$. The time evolution of the singlet

state population $\rho_{11}(t)$ should be reflected in the time-dependent photoluminescence, which is the experimental observable. For our simulations, the energy differences ε_{nm} are given by the energy differences between triplet pair energy levels, as obtained from either the unperturbed zero-field Hamiltonian from Equations (5.2a-c) or by diagonalization of the Hamiltonian given in Equations (5.13-15).

Although Equations (5.11a-c) contain multiple rates as free parameters, the data analysis allows us to fix them with reasonable accuracy. The radiative decay rate of the singlet exciton is fixed by our previous measurements on superradiant tetracene thin films to be $k_{rad} = 0.08$ ns^{-1}, about twice that of molecular tetracene.[42] The initial decay of the singlet state is dominated by the sum of the k_{1n} rates, and for the single crystal we found the prompt fluorescence decay time to be 202 ps. Then we have $k_{12} = k_{13} = k_{14} = \frac{1}{3} \times \frac{1}{0.202\,ns} = 1.65$ ns^{-1}, assuming equal transition probabilities to the three triplet pair states with singlet character. We note that this initial singlet decay time is significantly longer than what was observed in our previous experiments on polycrystalline evaporated thin films[131] but is within the range of what previous workers have observed in single crystal tetracene samples.[53,73,106,138] The triplet fusion rates back to the singlet state determine the level of the DF signal relative to the peak of the prompt fluorescence signal (larger k_{n1} values lead to greater DF). We find that $k_{n1} = 0.1$ ns^{-1} gives a DF level close to what is observed experimentally. Note that in our model, these k_{n1} rates also contribute to the dephasing of the triplet pair state coherences and thus lead to damping of the oscillations. But we found that $k_{n1} = 0.1$ ns^{-1} was insufficient to account for all the

damping, and we added a T_{2TT} = 10 ns in order to adequately reproduce the data. Last, we set the triplet population relaxation term k_{trip} = 0.4 ns^{-1} in order to describe the rapid initial decay of the SF seen in the 20 ns time window. The use of single k_{trip} value to describe the DF decay in the 2-20 ns time regime is clearly not sufficient, and it is likely that this decay is due at least in part to triplet diffusion and recombination, rather than simple relaxation to the ground state. Nevertheless, this k_{trip} value is similar to that used to describe the intermediate time photoluminescence decay in our previous experiments on tetracene thin films[131] and provides a way to parameterize our data.

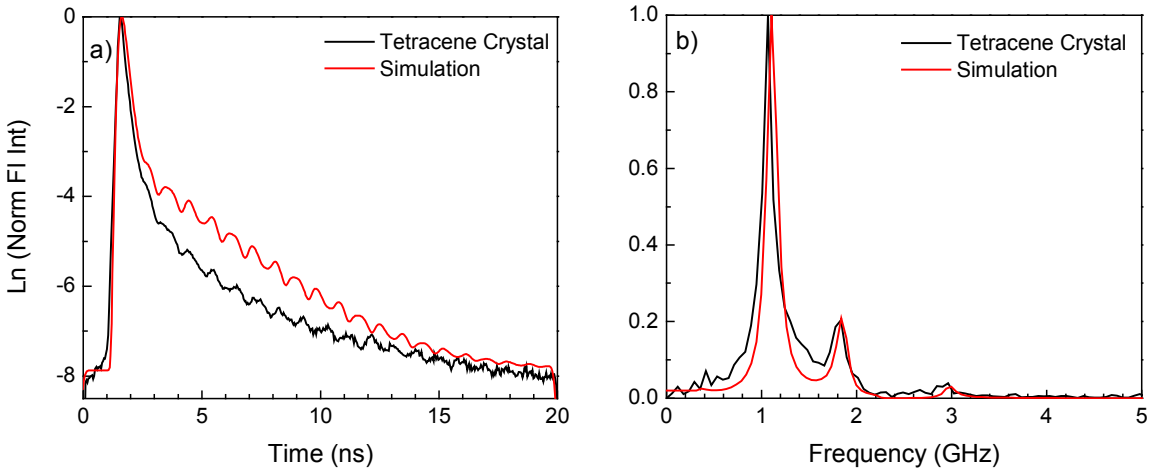

Figure 5.3 a) Time resolved photoluminescence of a solution grown single crystal of tetracene (black) along with simulated data convolved with an instrument response (red), where k_{1n} = 1.65 ns^{-1}, k_{n1} = 0.1 ns^{-1}, k_{rad} = 0.08 ns^{-1}, T_{2TT} = 10 ns, k_{trip} = 0.4 ns^{-1}, D* = -0.186 ns^{-1} and E^* = 0.744 ns^{-1}. **b)** Normalized Fourier transforms of the extracted frequencies from solution grown single crystal of tetracene (black) along with simulated data convolved with an instrument response (red) with the same parameters as **a)**.

In Figure 5.3a we compare a simulation of the entire photoluminescence signal, from the rising edge to the DF over 20 ns, with the experimental data. For the simulation, we convolved the calculated decay with a 15 ps full-width-half-maximum instrument response. The simulated data does a decent job of reproducing the overall signal shape as

well as the amplitude and damping of the oscillations for the single crystal. These calculated oscillations are significantly larger than those observed in an evaporated film, as shown in Figure 5.1. This suggests that sample preparation plays a role in determining the oscillation visibility. We suspect that structural disorder in the polycrystalline film leads to some fraction of the triplet pairs that undergo dephasing of their spin states very rapidly. Triplet pairs that have collapsed into their constituent $|xx\rangle$, $|yy\rangle$ and $|zz\rangle$ pair states can still undergo fusion and contribute to the DF signal, but such states will not lead to the quantum beats that are the signature of the superposition states. A second point is that the FT peaks in Figure 5.5b from the simulation data using the energy difference given in Equations (5.3a-c) are all shifted slightly to lower frequency due to the strong damping. Taking into account the error ranges in the D* and E* values obtained by Yarmus et al.[47], the FT peaks in the simulations are calculated to appear at frequencies ranging from 1.07-1.17 GHz, 1.76-1.90 GHz, and 2.88-3.03 GHz. All three of these frequency ranges fall within the error range of our experimentally measured frequencies. Thus our measurements agree with those predicted by the zero-field Hamiltonian for a single triplet exciton to within the experimental error.

5.2.3 Dependence of oscillations on singlet fission rate

The relative amplitudes of the three beat frequencies are quite sensitive to the SF rate as given by k_{1n}. To understand this phenomenon, we can consider two limits: very fast SF and very slow SF. In the limit of very rapid SF, the process acts like an ultrafast pulse that impulsively excites the triplet manifold, creating a narrow wavepacket that

oscillates equally among the three states. Since all three triplet pair states have the same singlet projection, we would expect equal amplitude oscillations from all three possible coherences: xx-yy, xx-zz, and yy-zz. In the opposite limit of very slow SF, the population transfer is much slower than the oscillation frequency and there is no opportunity to create a wavepacket. In this limit, no quantum beats would be observed. In Figure 5.4, we compare simulations for different k_{1n} rates, where the k_{n1} rates have been fixed to be 0.1 ns^{-1}. As expected, very rapid SF rates lead to comparable amplitude oscillations at all three beat frequencies. As k_{1n} is decreased, not only do the overall amplitudes of all the oscillations decrease relative to the rest of the signal, as seen in Figures 5.4a-c, but in addition the amplitudes of the higher frequency oscillations decrease relative to the lowest frequency yy-zz oscillation.

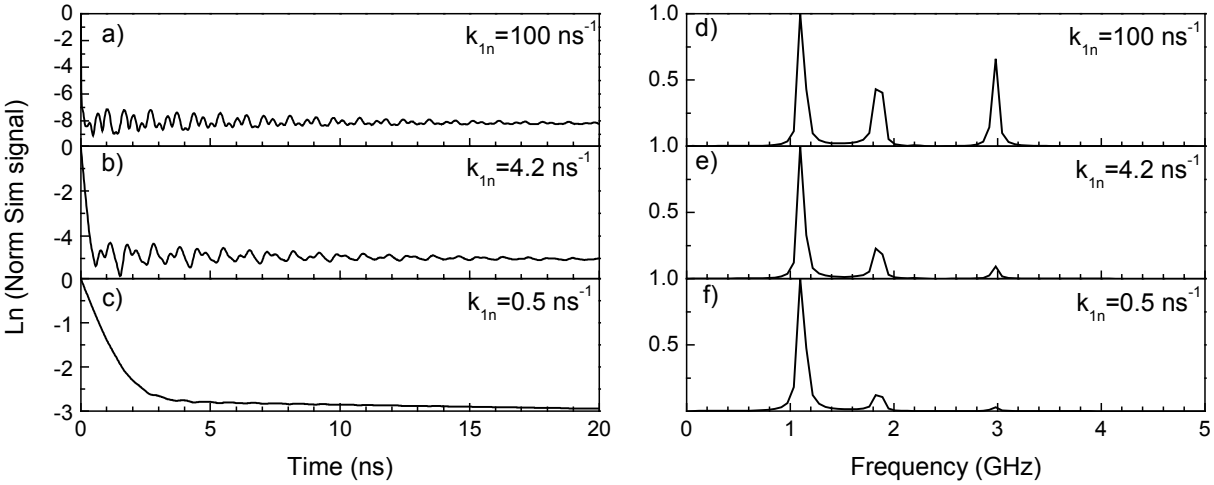

Figure 5.4 Simulated oscillations for k_{1n} = **a)** 100 ns^{-1} **b)** 4.2 ns^{-1} and **c)** 0.5 ns^{-1}, with k_{n1} = 0.1 ns^{-1}, T_{2TT} = 10 ns, D* = -0.186 ns^{-1} and E^* = 0.744 ns^{-1}. Normalized Fourier transforms of the simulated oscillations in **a)**, **b)**, and **c)** are found in **d)**, **e)**, and **f)** respectively.

For k_{1n} = 0.5 ns^{-1}, the highest frequency xx-yy oscillation peak is no longer visible. In order to obtain the FT profile observed experimentally, our k_{1n} rates must be in the intermediate regime, where the low frequency yy-zz oscillation is efficiently excited, but the high frequency xx-yy oscillation is barely excited. The data in Figure 3b show that the k_{1n} rates deduced from the decay rate of the prompt fluorescence are consistent with the Fourier amplitude analysis. In essence, two independent measurements, the FT amplitudes and the photoluminescence decay rate, give the same SF rate. A second observation from our modeling is that the damping of the oscillations results from both k_{n1} population exchange between the singlet and triplet manifolds and from pure T_{2TT} dephasing between the triplet levels themselves. Thus the DF process that allows us to detect the triplets also destroys their spin coherence. In a system where the triplet fusion leading to DF is much slower or nonexistent, e.g. crystalline pentacene, it may be possible that the triplet superposition state can persist for a longer time.

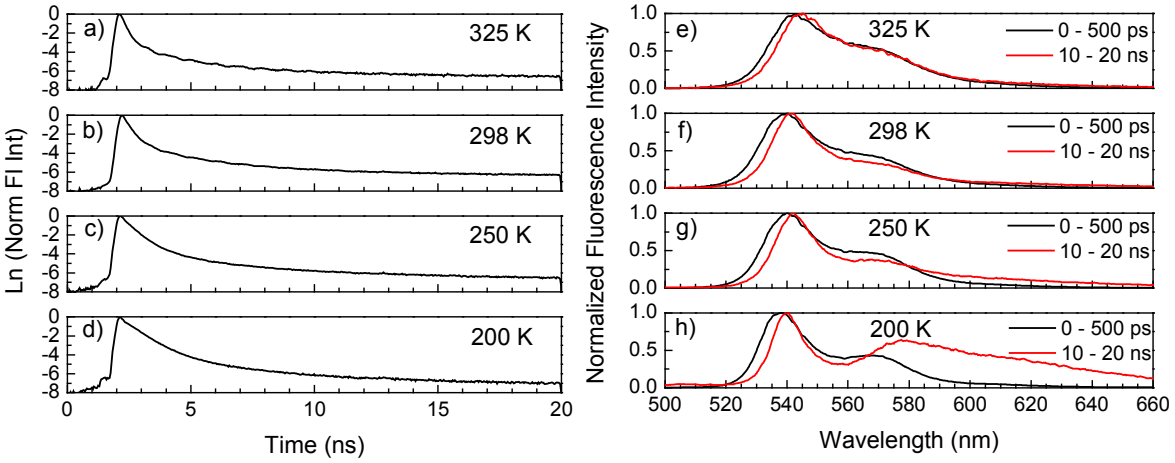

Figure 5.5 Time-resolved photoluminescence integrated from 525–545 nm of a solution grown single crystal of tetracene at **a)** 325 K, **b)** 298 K, **c)** 250 K and **d)** 200 K. The time-integrated spectra of the same crystal from 0-500 ps (black) and 10-20 ns (red) at **e)** 325 K, **f)** 298 K, **g)** 250 K and **h)** 200 K.

5.2.4 Temperature dependence of oscillations

The idea that changing the SF k_{1n} rates can change the visibility and relative amplitudes of the quantum beats can be tested by changing the temperature of the sample. Figures 5.5a-d show the wavelength-integrated photoluminescence decays for a single crystal at four different temperatures: 325 K, 298 K, 250 K, and 200 K. Two aspects of the photoluminescence signal change as the temperature is decreased. First, the rate of the initial singlet decay decreases, indicating that SF is slowing down. Analysis of the temperature dependence is complicated by the fact that the changes in photoluminescence decay dynamics are accompanied by changes in the spectral shape. Figures 5.5e-h shows the prompt (0-100 ps) and delayed (15-20 ns) photoluminescence spectra at the four temperatures. Ideally, the spectrum of the DF would mirror that of the prompt fluorescence, and this is indeed the case at 325 K and 298 K. At 250 K and 200 K, however, it appears that the true delayed fluorescence is now accompanied by a new red-shifted emitting species. Below 200 K, crystalline tetracene can undergo at least one solid-state phase transition [109-111] that leads to large changes in photoluminescence. We note that for a single crystal we found that the decay of the high energy singlet peak at 77 K was more rapid than at 200 K, similar to what we have observed in polycrystalline films.[131] At present, we have no explanation for this behavior, other than to note that temperature-dependent changes in crystal structure could lead to a complicated interplay between multiple decay channels. As in the case of tetracene thin films, the temperature dependent photoluminescence cannot be understood solely in terms of a single species. With these factors in mind, we will consider only the temperature range 325-200K, well

above the point where tetracene undergoes a solid-state phase transition, where it appears that the expected slowdown for SF as an activated process is occurring. The important observation is that as the SF rate decreases, the visibility of the oscillations decreases as well. In Figures 5.6a-d, we plot the oscillatory component of the signal from Figures 5.5a-d. The oscillations have completely disappeared by 200 K. In Figures 5.6e-h, we plot the calculated oscillations as the k_{1n} rates change from 2.07 ns^{-1} at 325 K to 0.94 ns^{-1} at 200 K, values that reflect the slowdown in the decay rate of the prompt fluorescence. This factor of 2 change in k_{1n} leads to roughly a factor of 2 decrease in the visibility of the simulated oscillations. The relative FT amplitudes are much less sensitive to small changes in the k_{1n} rates and do not change.

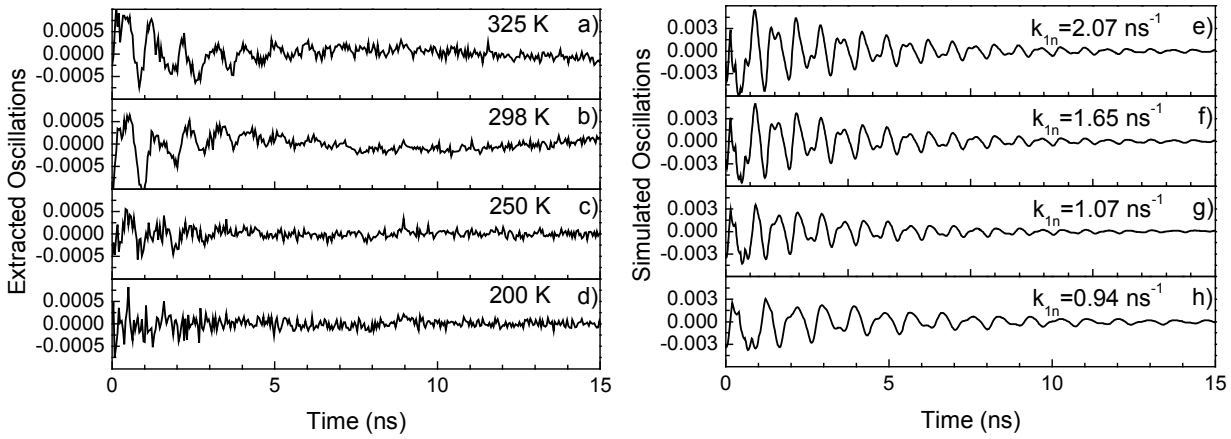

Figure 5.6 Extracted oscillations at **a)** 325 K, **b)** 298 K, **c)** 250 K, and **d)** 200 K. Simulated oscillations with the k_{1n} rate adjusted to match the fit of the experimental data for 325 K with **e)** k_{1n} = 2.07 ns^{-1}, 298 K with **f)** k_{1n} = 1.65 ns^{-1}, 250 K with **g)** k_{1n} = 1.07 ns^{-1}, and 200 K with **h)** k_{1n} = 0.94 ns^{-1}. The other values for the simulation are k_{n1} = 0.1 ns^{-1}, k_{rad} = 0.08 ns^{-1}, T_{2TT} = 10 ns, D* = -0.186 ns^{-1} and E^* = 0.744 ns^{-1}.

Both experimental and simulated data show the same trend: smaller oscillations as k_{1n} decreases, but the effect is much more pronounced in the experimental data. We

suspect that the replacement of the DF signal by the lower energy emission at 200 K may also play a role in decreasing the overall amount of DF and thus the visibility of the oscillations. The combination of a slower SF rate and reduced DF signal due to competition from lower energy trap states may explain the almost total loss of oscillations at 200 K.

5.2.5 Magnetic dipole-dipole coupling between triplet excitons

In the preceding analysis, we have assumed that the triplet-triplet interaction was negligible and that the triplet pair energies correspond to twice those of the zero-field Hamiltonian for a single triplet exciton. If the interaction term is nonnegligible, then we would expect to see shifts in the energies and in the singlet character of the stationary triplet pair states. For two interacting triplet excitons denoted *A* and *B*, we can follow the treatment of Benk and Sixl[139] and write

$$\hat{H}_{tot} = \hat{H}^{A}_{zero} + \hat{H}^{B}_{zero} + \hat{H}^{AB}_{\text{int}} \tag{5.13}$$

In the simplest limit of parallel magnetic dipoles interacting via dipole-dipole coupling,

$$\hat{H}^{AB}_{\mathbf{int}} = X\hat{S}_x^A\hat{S}_x^B + XA\hat{S}_y^A\hat{S}_y^B - X(1+A)\hat{S}_z^A\hat{S}_z^B + X\alpha\left(\hat{S}_z^A\hat{S}_y^B + \hat{S}_y^A\hat{S}_z^B\right) \tag{5.14}$$

where

$$X = \frac{g^2\mu_B^2}{R_{AB}^3} \tag{5.15a}$$

$$A = 1 - 3\,\mathbf{sin}(\phi)^2 \tag{5.15b}$$

$$\alpha = \sqrt{(1-A)(2+A)} \tag{5.15c}$$

In these equations, the EPR g-factor g = 2.002 , μ_B = 9.274x10^{-24} J/Tesla is the Bohr magneton, and ϕ is the angle of the magnetic z-axis with respect to the intermolecular distance vector $\vec{R}_{AB}$. For R_{AB} = 5.125 Å, the distance between nearest neighboring tetracenes in the crystal[92], we find that X = 0.013 cm^{-1}, comparable to the zero-field splitting energies. If the triplets are created within close proximity to each other, as would be expected in SF, then it is possible that their interaction could lead to shifts in energies and spin state coefficients. A complete analysis of the interactions between triplet excitons is beyond the scope of this chapter. Here we give a simple example of how magnetic dipole-dipole interactions could affect the oscillations observed in the DF. We consider the case of two triplets whose z-axis magnetic tensors are parallel and aligned along the $\vec{R}_{AB}$ separation vector ($\phi = 0$). Since the z* axis in crystalline tetracene is aligned close to the crystal *b*-axis [47], this situation is not physically unreasonable for a pair of triplets trapped in the *ab* plane. Here we will only consider the effect of $\hat{H}_{\mathbf{int}}^{AB}$ on the observed oscillation frequencies, since these quantities have been measured to greater precision than the relative FT amplitudes. By diagonalizing $\hat{H}_{tot}$ in the zero-field product basis for various values of X, we can find the energies of the three triplet pair states with singlet character and calculate their beat frequencies in the DF signal. As X increases, these states shift farther apart and the frequencies of all three oscillations increase, as shown in Figure 5.7. Even given the uncertainty range in the frequencies as discussed above, the data in Figure 5.7 allow us to make a conservative estimate for the upper limit of $X \leq$ 0.008 cm^{-1}.

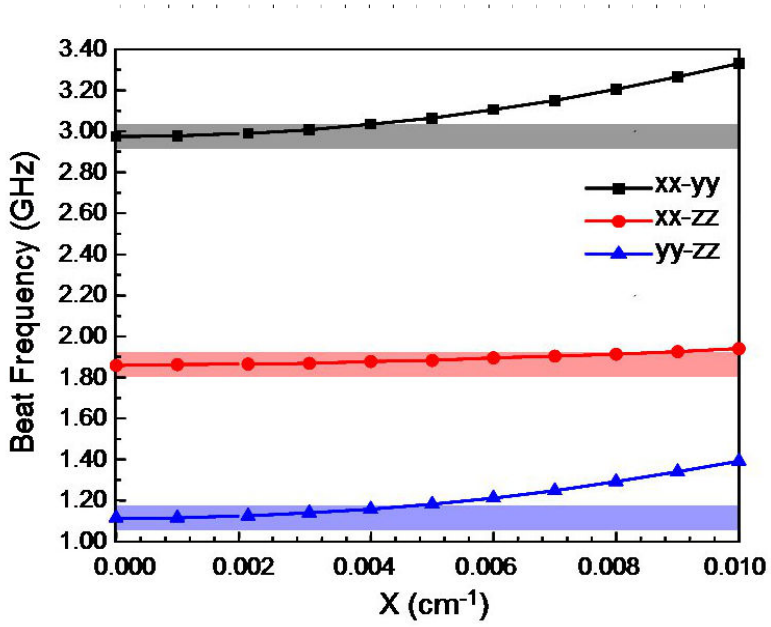

Figure 5.7 The transparent boxes indicate the experimental error in the beat frequencies and also reflect the error in the zero-field parameters from ref [47]. The lines represent the calculated energy splittings of the triplet pair states with singlet character as X, the strength of the magnetic dipole-dipole interaction between triplet excitons, is increased.

Using Equation (5.15a), we would estimate that the triplets must be at least 6 Å apart. If we assume that the small X value reflects a large R_{AB} value, it is interesting to speculate as to why the distance between the two triplets would be greater than the nearest neighbor spacing. One explanation is that this separation arises from the delocalized nature of the initial singlet exciton[42,87,108], which allows triplets to be created at larger separations than would be expected for a singlet state localized on only one molecule. Instead of being created on nearest neighbor tetracene molecules, the delocalized singlet could spawn triplets on opposite sides of a 3x3 array of tetracene molecules with a separation R_{AB}>1 nm. A second mechanism that could generate large separations is rapid spatial diffusion of the triplets. Estimates for the diffusion constant of a triplet exciton in crystalline tetracene vary[69,76,78-80], but even a low value of 10^{-5}

cm^2/s could increase their separation by a nanometer or more within the first nanosecond. The surprising thing about such an explanation is that this would require that spin coherence is maintained while the triplets randomly jump between sites in the crystal. Finally, we should emphasize that we have assumed $\phi = 0$ and that the triplets are stationary. If these assumptions are relaxed, then there may be alternative explanations for the lack of an observable effect from magnetic dipole-dipole interactions. For example, rather than a large R_{AB}, it is possible that rapid reorientation of the triplets could average the dipole-dipole interaction term to zero, in much the same way that rapid reorientation washes out the effects of magnetic dipolar effects in NMR spectroscopy.[140] In the analysis of tetracene's EPR spectroscopy, it is assumed that the triplets are hopping back and forth between molecules on a timescale rapid compared to the EPR timescale, so that the crystal field parameters actually reflect an average of the non-equivalent crystallographic sites.[47,141] Rapid changes in ϕ or other orientation angles could average the $\hat{H}_{\mathbf{int}}^{AB}$ term to zero, although more detailed modeling is required in order to prove that this is actually the case.

5.2.6 Relation of results to previous work and mechanism of singlet fission

We now try to place our results on the DF quantum beats into context with previous work by our group and others on the photophysics of crystalline tetracene. The density matrix model presented in this chapter is based on the "direct" mechanism of SF, where the transition to the triplet manifold directly creates a triplet pair superposition state. It should be noted, however, that the observation of the spin signature of triplet

superposition states in the DF does not necessarily rule out a charge-transfer intermediate, since this observation requires only that spin coherence is preserved throughout the SF process. Spin-conserving electron transfer processes are routinely observed in condensed phase systems[142-144], and it is possible that two sequential electron transfer events (as in the "indirect" mechanism) could maintain spin coherence as well. If this was the case, however, the intermediate charge-transfer state must be very short-lived, since our modeling does not indicate any delay between the decay of the singlet and the formation of the triplet. The simplest interpretation of our data is that the triplet pair superposition state is formed as a result of a direct transition from the initially excited singlet. Later, after this superposition state is dephased, two free triplet excitons are formed.

In addition to the mechanism of SF, we also need to consider the rate of this process. We were surprised to find such a large difference (more than a factor of 2) between the prompt singlet decay rates in polycrystalline versus single crystal samples. The very low optical density of our solution grown crystals helps rule out effects like reabsorption-re-emission events as an explanation for the longer decay in these samples. One possible explanation is that SF is actually more rapid in the films due to their disorder, which could lead to configurations (e.g. face-to-face) that are more favorable for SF.[126] A second explanation is that there is some other singlet decay channel in addition to SF in the films that is not present in the crystals. But it is important to note that the quantum beating that is a signature of the formation of triplet pair states via SF is present in both types of samples. Equations (5.10a-c) allow us to make a rough estimate

of the electronic coupling between the triplet pair state and the singlet. If we take the electronic dephasing time T_{2TS} to be 100 fs, a typical value for condensed phase systems, and use $k_{1n} = 1.65$ ns^{-1}, we find that M_{1n} is on the order of 5 cm^{-1}. This value is less than the width of the absorption spectrum and consequently the weak coupling between the two states would not result in any noticeable splittings or intensity redistribution in the linear spectroscopy. This estimate of M_{1n} is also a least two orders of magnitude smaller than that deduced for pentacene[135], a system that undergoes much more rapid SF.

Finally, we discuss the temperature dependence of the SF rate. In our earlier experiments on polycrystalline tetracene films described in Chapters 3 and 4, we found that a rapid decay of the J-type singlet exciton was present at 298 K, 77 K, and 4 K.[103,131] The ~100 ps SF relaxation channel that is presumed to dominate at room temperature thus did not appear to be thermally activated, despite the fact that the DF rapidly disappears as the temperature is lowered. But as discussed above, structural changes below 200 K may lead to other decay channels that result in a rapid singlet decay where free triplets cannot be produced. Our suggestion that the initial SF step is not thermally activated may need to be revised in light of the data in Figures 5.5 and 5.6. In the limited temperature range 325-200 K, the singlet decay does slow down at lower temperatures, although the decay speeds up again at even lower temperatures. Previously, we had postulated that the persistent 100 ps decay could reflect a barrierless relaxation channel into a dark intermediate whose subsequent dissociation into free triplets was thermally activated. But if we assign the dark state to a triplet pair superposition, this state would have to be lower in energy by hundreds of cm^{-1} relative to that of two free triplet excitons

in order to provide a barrierless transition from the singlet. Such a lowering of the energy would imply that the two excitons have strong electronic interactions, and it is not clear whether such a bound pair would also exhibit spin properties similar to those of unperturbed triplets, as found in this work. One would have to assume that the electronic wavefunction of such a state is effectively decoupled from its spin properties, an assertion that can only be tested by further experiments or by computation. The temperature dependence of the singlet exciton decay in tetracene continues to be somewhat of a puzzle. Our results are certainly not consistent with a simple single channel SF process that is thermally activated, as assumed by most previous workers.

5.3 Conclusions

In this work, we have revisited the earlier results by Chabr et al. where quantum beats from coherent triplet pairs were first observed. We have examined how these oscillations depend on sample morphology, temperature, and excitation energy. A density matrix model for this process has been developed that can quantitatively describe the frequencies, amplitudes, and damping of the oscillations. The damping of the oscillations on the 20 ns timescale is driven partly by population exchange between triplet and singlet manifolds and does not necessarily reflect the pure dephasing rates of the triplet pair states. The decrease in oscillation visibility at lower temperatures is consistent with the observed slowdown in the SF rate, but the effect is much stronger in the experiments than in the simulated data. Analysis of the quantum beat frequencies provides no indication that triplet-triplet interactions are important on the nanosecond

timescale in the coherent triplet pairs. This work provides strong evidence for the direct, incoherent production of triplet pair superposition states with overall singlet character, as predicted by earlier kinetic theories of SF. While it does not answer all questions about the process, in particular the precise electronic structure of the triplet superposition state that lives for ~10 ns after SF, it does clarify issues concerning the overall rate and nature of the product state.

CHAPTER 6

Conclusions

6.1 Summary and conclusions

In the Introduction, we introduced the need for alternative energy research, and how SF is a viable mechanism for improving photovoltaic efficiencies. In order to better understand SF, this dissertation has confirmed SF and clarified its rate within crystalline tetracene to be 1.25×10^{10} s^{-1}, although complications from exciton-exciton annihilation initially confused our results. Additionally, the temperature dependent photoluminescence experiments have shown that SF may not be thermally activated as the literature believes. Close examination of the delayed fluorescence of single crystals of tetracene have also revealed quantum beats that can be used to probe the various triplet levels in tetracene. These quantum beats also illustrate the speed of SF within tetracene based on the amplitudes of the different frequencies, which tells us that the direct mechanism is descriptive of how SF occurs within crystalline tetracene.

In Chapter 3, time resolved photoluminescence and transient absorption are used to compare the dynamics of tetracene in solution and in polycrystalline films. Using these experiments, the creation and spectrum of the triplet absorption in solution is verified with TA and consistent with previous work in the literature. Initial experiments on the photoluminescence of the polycrystalline films led us to look for an ~80 ps decay from the singlet state while watching for the triplet to grow in at that rate or slower, but the broadband TA experiments showed a much faster singlet decay which we originally

concluded was due to energy transfer to a photoluminescence defect state. The rate of production of the triplets could not be directly confirmed in the polycrystalline films with broadband TA because of several experimental complications. In the broadband TA of these solid samples, exciton-exciton annihilation becomes important at the fluences that are required to get adequate signal-to-noise. Another problem is that delocalization of the singlet excited state leads to superradiance of the singlet to be effectively three times stronger, making it stronger than the triplet absorption. The last difficulty with distinguishing the triplet is due to the orientation of the molecule within the polycrystalline film, where XRD confirmed that the transition dipole moment of the triplet is approximately eight times smaller than the superradiant transition dipole moment of the singlet. Although direct measurement of the triplet population was not achieved in our experiments, monitoring the recovery of the ground state bleach recovery indirectly gives evidence for a trapping mechanism in the recombination of the triplets. The work presented in this chapter was also shown to be consistent with work in the literature. Using a simple model and parameters from the literature and our experiments, the photoluminescence decays were reproduced by simulations.

Building on the work in Chapter 3, the experiments in Chapter 4 begin by completing a study of the excitation energy dependence of the TA over two orders of magnitude, a much greater range than was possible for the broadband TA experiments. This was accomplished by focusing on a single channel 10 nm window for the TA experiment rather than the 300 nm window used for the broadband experiments in Chapter 3. At lower fluences, the TA and photoluminescence decays match, removing

the need for the existence of a photoluminescent defect to explain the room temperature data. Delving deeper into the mechanism of SF, we then extend the time resolved photoluminescence measurements to low temperatures in order to investigate the activation energy of SF within tetracene and elucidate how SF occurs. The photoluminescence shows a fast decay at all temperatures (298, 77, and 4 K), indicating that SF is not turned off at lower temperatures as the literature believes. The excitation energy dependence of SF at lower temperatures was also tested, and excess energy from the excitation was ruled out as the source of the fast decay at all temperatures. The lack of temperature dependence in the initial decay indicates that there is no barrier for SF, but the lack of delayed fluorescence shows that the reverse process is not occurring. However, at lower temperatures, we also observed photoluminescence from additional long-lived states which increase the overall photoluminescence intensity. Global analysis was also conducted on the photoluminescence data to determine the relationship between the emitting species, which shows that the emitting species all decay independently rather than the lower energy states being populated from energy transfer from the higher energy states. In order to explain this data, we consider the 2-step kinetic model put forth by the literature to analyze magnetic field effects, which can explain this data if the intermediate state creation is not thermally activated but the dissociation to free triplets is.

Although the model used in Chapter 4 can explain the temperature dependence of the photoluminescence data, it does not give any indication about the identity of the intermediate state creation. However, photoluminescence experiments on single crystals showed the same quantum beats as were previously reported by Chabr et al.[55] By

studying the dependence of these oscillations on the sample morphology, temperature, and excitation energy, a better model was created using density matrix theory, which can quantitively describe the frequencies, amplitude, and damping of the oscillations within tetracene. From the combination of experiment and theory, we have uncovered several key points about SF based on these oscillations. First of all, since the frequencies of the quantum beats correspond to the zero field splittings of the triplets, this shows that the interaction between triplets is not very strong since that should perturb the splittings between triplet levels. Additionally, the damping of the oscillations is not purely due to dephasing of the triplets and can in part be due to multiple exchanges in the population of the singlet and triplet manifolds. Finally, the temperature dependence of the oscillations and decrease in visibility is consistent with the reduced rate of SF, but the simulated data is unable to capture the strength of this effect that is found experimentally. Based on this work, Chapter 5 shows strong evidence for the direct mechanism of SF via an incoherent production of a superposition of triplet pair states of overall singlet character, which is also consistent with early work on SF.

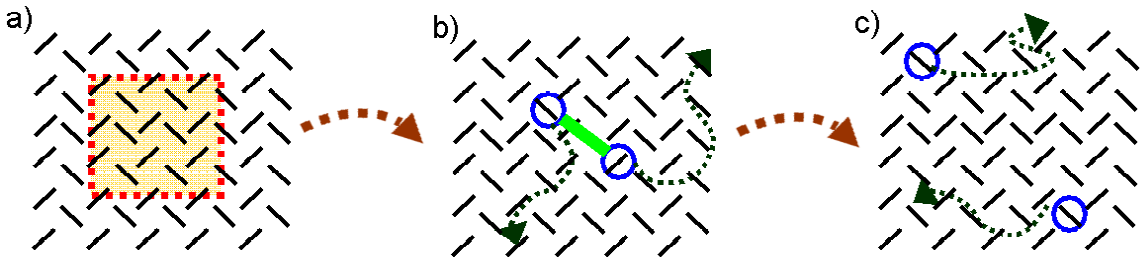

Figure 6.1 A physical illustration of the progression of SF in crystalline tetracene, where the a) delocalized S_1 parent state fissions into the b) spin-entangled, weakly interacting triplet pair state, $^1(T_1\ T_1)$, before it evolves into the c) dephased independent triplets, $T_1 + T_1$.

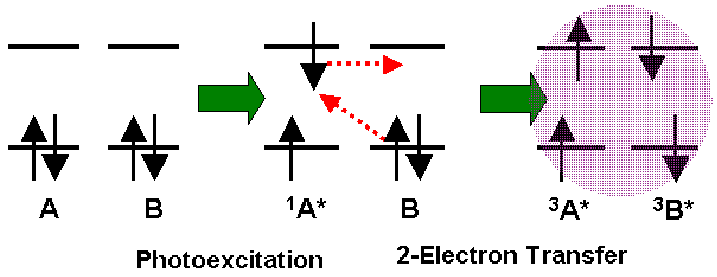

Figure 6.2 Based on the work in this dissertation, SF in crystalline tetracene according to the direct mechanism, which has a simultaneous transfer of electrons to form the two triplet states.

While many questions such as the rate and mechanism of SF in tetracene have been answered, there are several aspects of SF in tetracene that are not completely understood. The temperature dependence of fluorescence in the single crystal puts some doubt on the previous measurements of the polycrystalline films, and more work needs to be done to clarify the temperature dependence of SF within tetracene. Additionally, while the oscillations illustrate the creation of a coherent triplet pair, the role that spin coherence plays on the triplet state evolution is not currently known. While magnetic fields have been used to modulate the rate of SF, the dependence of SF on these fields has not been determined yet. Finally, while the high yield of triplets due to SF has already been demonstrated, there has been no proof that the triplets formed from SF can be effectively harnessed in a device. Although good headway has been made into the subject of SF, there are still many areas which require further study.

6.2 Future directions of this work

There are several directions of research that can follow up on the work done in this dissertation. While tetracene is a good example of SF and a viable candidate for a sensitizer in photovoltaic cells, the study of SF in other systems may be more effective for photovoltaic enhancement and should be studied. In order to apply SF more generally to photovoltaic applications, it is important to understand how the electronic energy levels and properties of the system affect SF. To do this, experiments can be done on other polyacenes in order to compare them with tetracene. Rubrene is a tetracene derivative that shares the same triplet energy levels as tetracene, and it can be grown as crystalline or amorphous solids. Another possibility is anthracene, where the triplet fusion was first discovered. In anthracene, the energy of two triplets is greater than the energy of the singlet and SF does not occur with excitation to the S_1 state. However, if SF could be turned on in crystalline anthracene by exciting it with higher energy photons, this would also be useful for understanding more about the mechanism of SF. Another direction for further research would be to study the dynamics of exciton diffusion within tetracene. Specifically, further experiments can be done to study the spread of excitation within single crystals of tetracene and the possibility of energy transfer from tetracene triplets to other molecule. Photoluminescence imaging of tetracene single crystals can be conducted in order to monitor the position of the prompt and delayed fluorescence, which will help elucidate the role of exciton diffusion within the mechanism of SF. It is also relevant to energy transfer experiments because it will show whether or not the triplets created by SF can move far away from excitation and then fluoresce after recombination with another triplet, and the study of the quantum beats in the delayed fluorescence will

also show which triplets are capable of recombining after diffusing. In order to determine if tetracene is a viable sensitizer, the photoluminescence of tetracene on Si and other photovoltaic materials can be studied to check for photoluminescence quenching in the prompt or delayed fluorescence due to energy transfer from singlet or triplet excitons to the semiconductor.

References

(1) Grätzel, M. *Nature* **2001**, *414*, 338.

(2) Spanggaard, H.; Krebs, F. C. *Solar Energy Materials & Solar Cells* **2004**, *83*, 125.

(3) Shockley, W.; Queisser, H. J. *Journal of Applied Physics* **1961**, *32*, 510.

(4) Brabec, C. J. *Solar Energy Materials & Solar Cells* **2004**, *83*, 273.

(5) Paci, I.; Johnson, J. C.; Chen, X.; Rana, G.; Popovic, D.; David, D. E.; Nozik, A. J.; Ratner, M. A.; Michl, J. *J. Am. Chem. Soc.* **2006**, *128*, 16546.

(6) Warta, W.; Stehle, R.; Karl, N. *Appl. Phys. A* **1985**, *36*, 163.

(7) Hanna, M. C.; Nozik, A. J. *J. Appl. Phys.* **2006**, *100*, 074510/1.

(8) Shpaisman, H.; Niitsoo, O.; Lubomirsky, I.; Cahen, D. *Sol. En. Mater. Sol. Cells* **2008**, *92*, 1541.

(9) Nozik, A. J. *Physica E* **2002**, *14*, 115.

(10) Schaller, R. D.; Klimov, V. I. *Phys. Rev. Lett.* **2004**, *92*, 186601/1.

(11) Sambur, J. B.; Novet, T.; Parkinson, B. A. *Science* **2010**, *330*, 63.

(12) Semonin, O. E.; Luther, J. M.; Choi, S.; Chen, H. Y.; Gao, J.; Nozik, A. J.; Beard, M. C. *Science* **2011**, *334*, 1530.

(13) Singh, S.; Jones, W. J.; Siebrand, W.; Stoicheff, B. P.; Schneider, W. G. *J. Chem. Phys.* **1965**, *42*, 330.

(14) Greyson, E. C.; Stepp, B. R.; Chen, X.; Schwerin, A. F.; Paci, I.; Smith, M. B.; Akdag, A.; Johnson, J. C.; Nozik, A. J.; Michl, J.; Ratner, M. A. *J. Phys. Chem. B* **2010**, *114*, 14223.

(15) Yoo, S.; Domercq, B.; Kippelen, B. *Appl. Phys. Lett.* **2004**, *85*, 5427.

(16) Shao, Y.; Sista, S.; Chu, C. W.; Sievers, D.; Yang, Y. *Appl. Phys. Lett.* **2007**, *90*, 103501/1.

(17) Chu, C. W.; Shao, Y.; Shrotriya, V.; Yang, Y. *Appl. Phys. Lett.* **2005**, *86*, 243506/1.

(18) Swenberg, C. E.; Stacy, W. T. *Chem. Phys. Lett.* **1968**, *2*, 327.

(19) Jundt, C.; Klein, G.; Sipp, B.; Moigne, J. L.; Joucla, M.; Villaeys, A. A. *Chem. Phys. Lett.* **1995**, *241*, 84.

(20) Avakian, P.; Abramson, E.; Kepler, R. G.; Caris, J. C. *J. Chem. Phys.* **1963**, *39*, 1127.

(21) Johnson, R. C.; Merrifield, R. E.; Avakian, P.; Flippen, R. B. *Phys. Rev. Lett.* **1967**, *19*, 285.

(22) Merrifield, R. E.; Avakian, P.; Groff, R. P. *Chem. Phys. Lett.* **1969**, *3*, 155.

(23) Geacintov, N.; Pope, M.; Vogel, F. *Phys. Rev. Lett.* **1969**, *22*, 593.

(24) Hofberger, W. *Phys. Stat. Sol. A* **1975**, *30*, 271.

(25) Lee, J.; Jadhav, P.; Baldo, M. A. *Appl. Phys. Lett.* **2009**, *95*, 033301/1.

(26) Rao, A.; Wilson, M. W. B.; Albert-Seifried, S.; Pietro, R. D.; Friend, R. H. *Phys. Rev. B* **2011**, *84*, 195411/1.

(27) Marciniak, H.; Fiebig, M.; Huth, M.; Schiefer, S.; Nickel, B.; Selmaier, F.; Lochbrunner, S. *Phys. Rev. Lett.* **2007**, *99*, 176402/1.

(28) Marciniiak, H.; Pugliesi, I.; Nickel, B.; Lochbrunner, S. *Phys. Rev. B* **2009**, *79*, 235318/1.

(29) Kuhlman, T. S.; Kongsted, J.; Mikkelsen, K. V.; Moller, K. B.; Solling, T. I. *J. Am. Chem. Soc.* **2010**, *132*, 3431.

(30) Muller, A. M.; Avlasevich, Y. S.; Mullen, K.; Bardeen, C. J. *Chem. Phys. Lett.* **2006**, *421*, 518.

(31) Muller, A. M.; Avlasevich, Y. S.; Schoeller, W. W.; Mullen, K.; Bardeen, C. J. *J. Am. Chem. Soc.* **2007**, *129*, 14240.

(32) Gabor, N. M.; Zhong, Z.; Bosnick, K.; Park, J.; McEuen, P. L. *Science* **2009**, *325*, 1367.

(33) Michl, J.; Nozik, A. J.; Chen, X.; Johnson, J. C.; Rana, G.; Akdag, A.; Schwerin, A. F. *Proc. SPIE* **2007**, *6656*, 66560E.

(34) Lanzani, G.; Cerullo, G.; Zavelani-Rossi, M.; Silvestri, S. D. *Phys. Rev. Lett.* **2001**, *87*, 187402/1.

(35) Watanabe, S.; Furube, A.; Katoh, R. *J. Phys. Chem. A* **2006**, *110*, 10173.

(36) Gradinaru, C. C.; Kennis, J. T. M.; Papgiannakis, E.; Stokkum, I. H. M. v.; Cogdell, R. J.; Fleming, G. R.; Niederman, R. A.; Grondelle, R. v. *Proc. Nat. Acad. Sci.* **2001**, *98*, 2364.

(37) Guo, J.; Ohkita, H.; Benten, H.; Ito, S. *J. Am. Chem. Soc.* **2009**, *131*, 16869.

(38) Wang, C.; Tauber, M. J. *J. Am. Chem. Soc.* **2010**, *132*, 13988.

(39) Zimmerman, P. M.; Zhang, Z.; Musgrave, C. B. *Nat. Chem.* **2010**, *2*, 648.

(40) Zimmerman, P. M.; Bell, F.; Casanova, D.; Head-Gordon, M. *J. Am. Chem. Soc.* **2011**, *133*, 19944.

(41) Ahn, T. S.; Muller, A. M.; Al-Kaysi, R. O.; Spano, F. C.; Norton, J. E.; Beljonne, D.; Bredas, J. L.; Bardeen, C. J. *J. Chem. Phys.* **2008**, *128*, 054505/1.

(42) Lim, S. H.; Bjorklund, T. G.; Spano, F. C.; Bardeen, C. J. *Phys. Rev. Lett.* **2004**, *92*, 107402/1.

(43) Bouchriha, H.; Ern, V.; Fave, J. L.; Guthmann, C.; Schott, M. *J. de Physique* **1978**, *39*, 257.

(44) Barhoumi, T.; Monge, J. L.; Mejatty, M.; Bouchriha, H. *Eur. Phys. J. B* **2007**, *59*, 167.

(45) Frankevich, E. L.; Lesin, V. I.; Pristupa, A. I. *Chem. Phys. Lett.* **1978**, *58*, 127.

(46) Swenberg, C. E.; Metter, R. V.; Ratner, M. *Chem. Phys. Lett.* **1972**, *16*, 482.

(47) Yarmus, L.; Rosenthal, J.; Chopp, M. *Chem. Phys. Lett.* **1972**, *16*, 477.

(48) Groff, R. P.; Avakian, P.; Merrifield, R. E. *Phys. Rev. B* **1970**, *1*, 815.

(49) Klein, G.; Voltz, R.; Schott, M. *Chem. Phys. Lett.* **1973**, *19*, 391.

(50) Grumstrup, E. M.; Johnson, J. C.; Damrauer, N. H. *Phys. Rev. Lett.* **2010**, *105*, 257403/1.

(51) Thorsmolle, V. K.; Averitt, R. D.; Demsar, J.; Smith, D. L.; Tretiak, S.; Martin, R. L.; Chi, X.; Crone, B. K.; Ramirez, A. P.; Taylor, A. J. *Phys. Rev. Lett.* **2009**, *102*, 017401/1.

(52) Rao, A.; Wilson, M. W. B.; Hodgkiss, J. M.; Albert-Seifried, S.; Bassler, H.; Friend, R. H. *J. Am. Chem. Soc.* **2010**, *132*, 12698.

(53) Fleming, G. R.; Millar, D. P.; Morris, G. C.; Morris, J. M.; Robinson, G. W. *Aust. J. Chem.* **1977**, *30*, 2353.

(54) Campillo, A. J.; Hyer, R. C.; Shapiro, S. L.; Swenberg, C. E. *Chem. Phys. Lett.* **1977**, *48*, 495.

(55) Chabr, M.; Wild, U. P.; Funfschilling, J.; Zschokke-Granacher, I. *Chem. Phys.* **1981**, *57*, 425.

(56) Funfschilling, J.; Zschokke-Granacher, I.; Canonica, S.; Wild, U. P. *Helv. Phys. Acta* **1985**, *58*, 347.

(57) *Model TS laser kit oscillator manual*; Labs, K.-M., Ed.

(58) *Spitfire-50 Preliminary User's Manual*; Spectra-Physics, Ed., 1995.

(59) *Integra-C Customer Service Manual Revision D*; Quantronix, Ed., 2007.

(60) *Palitra FS - Customer Care Package*; Quantronix, Ed., 2009.

(61) *Operator's Manual Libra Ultrafast Amplifier Laser System*; Coherent, Ed., 2009.

(62) Laudise, R. A.; Kloc, C.; Simpkins, P. G.; Siegrist, T. *Journal of Crystal Growth* **1998**, *187*, 449.

(63) Kim, H. Y.; Bjorklund, T. G.; Lim, S.-H.; Bardeen, C. J. *Langmuir* **2003**, *19*, 3941.

(64) Carmichael, I.; Hug, G. L. *J. Phys. Chem. Ref. Data* **1986**, *15*, 1.

(65) Hofberger, W. *Phys. Stat. Sol. A* **1976**, *34*, K55.

(66) Spano, F. C. *Acc. Chem. Res.* **2010**, *43*, 429.

(67) Burgdorff, C.; Ehrhardt, S.; Lohmannsroben, H.-G. *J. Phys. Chem.* **1991**, *95*, 4246.

(68) Murov, S. L.; Carmichael, I.; Hug, G. L. *Handbook of Photochemistry*; 2nd ed.; Marcel Dekker, Inc.: New York, 1993.

(69) Kalinowski, J. *J. Luminesc.* **1976**, *11*, 393.

(70) Vaubel, G.; Baessler, H. *Phys. Stat. Sol.* **1970**, *37*, K31.

(71) Delannoy, P.; Schott, M. *Phys. Stat. Sol. B* **1975**, *70*, 119.

(72) Ern, V.; Saint-Clair, J. L.; Schott, M.; Delacote, G. *Chem. Phys. Lett.* **1971**, *10*, 287.

(73) Arnold, S.; Alfano, R. R.; Pope, M.; Yu, W.; Ho, P.; Selsby, R.; Tharrats, J.; Swenberg, C. E. *J. Chem. Phys.* **1976**, *64*, 5104.

(74) Arnold, S.; Whitten, W. B. *J. Chem. Phys.* **1981**, *75*, 1166.

(75) Klein, G. *Chem. Phys. Lett.* **1978**, *57*, 202.

(76) Pope, M.; Geacintov, N. E.; Saperstein, D.; Vogel, F. *J. Luminesc.* **1970**, *1,2*, 224.

(77) Arden, W.; Kotani, M.; Peter, L. M. *Phys. Stat. Sol. B* **1976**, *75*, 621.

(78) Vaubel, G.; Kallmann, H. *Phys. Stat. Sol.* **1969**, *35*, 789.

(79) Bizzaro, W.; Yarmus, L.; Rosenthal, J.; Berk, N. F. *Phys. Rev. B* **1981**, *23*, 5673.

(80) Aladekomo, J. B.; Arnold, S.; Pope, M. *Phys. Stat. Sol. B* **1977**, *80*, 333.

(81) Schug, J. C.; Brewer, D. A. *J. Phys. Chem.* **1977**, *81*, 167.

(82) Kadantsev, E. S.; Stott, M. J.; Rubio, A. *J. Chem. Phys.* **2006**, *124*, 134901/1.

(83) Kawashima, Y.; Hashimoto, T.; Nakano, H.; Hirao, K. *Theor. Chem. Acc.* **1999**, *102*, 49.

(84) Pariser, R. *J. Chem. Phys.* **1956**, *24*, 250.

(85) Bensasson, R.; Land, E. J. *Trans. Farad. Soc.* **1971**, *67*, 1904.

(86) Frolov, S. V.; Kloc, C.; Schon, J. H.; Batlogg, B. *Chem. Phys. Lett.* **2001**, *334*, 65.

(87) Voigt, M.; Langner, A.; Schouwink, P.; Lupton, J. M.; Mahrt, R. F.; Sokolowski, M. *J. Chem. Phys.* **2007**, *127*, 114705/1.

(88) West, B. A.; Womick, J. M.; McNeil, L. E.; Tian, K. J.; Moran, A. M. *J. Phys. Chem. C* **2010**, *114*, 10580.

(89) Tiberghien, A.; Delacote, G. *Chem. Phys. Lett.* **1971**, *8*, 88.

(90) Philpott, M. R. *J. Chem. Phys.* **1969**, *50*, 5117.

(91) Robertson, J. M.; Sinclair, V. C.; Trotter, J. *Acta Cryst.* **1961**, *14*, 697.

(92) Holmes, D.; Kumaraswamy, S.; Matzger, A. J.; Vollhardt, K. P. C. *Chem. Eur. J.* **1999**, *5*, 3399.

(93) Schwieger, T.; Liu, X.; Olligs, D.; Knupfer, M.; Schmidt, T. *J. Appl. Phys.* **2004**, *96*, 5596.

(94) Milita, S.; Santato, C.; Cicoira, F. *Appl. Surf. Sci.* **2006**, *252*, 8022.

(95) Sakurai, T.; Hayakawa, S. *Jap. J. Appl. Phys.* **1974**, *13*, 1733.

(96) Abthagir, P. S.; Ha, Y. G.; you, E. A.; Jeong, S. H.; Seo, H. S.; Choi, J. H. *J. Phys. Chem. B* **2005**, *109*, 23918.

(97) Webber, S. E.; Avots-Avotins, P. E. *J. Chem. Phys.* **1980**, *72*, 3773.

(98) Burkhart, R. D. *Macromolecules* **1983**, *16*, 820.

(99) Dreger, Z.; Kalinowski, J.; Kozankiewicz, B.; Prochorow, J. *J. Lum.* **1991**, *50*, 179.

(100) Siebrand, W. *J. Chem. Phys.* **1965**, *42*, 3951.

(101) Smith, G. C. *Phys. Rev.* **1968**, *166*, 839.

(102) Williams, J. O.; Zboinski, Z. *J. Chem. Soc. Farad. Trans. 2* **1978**, *74*, 618.

(103) Burdett, J. J.; Muller, A. M.; Gosztola, D.; Bardeen, C. J. *J. Chem. Phys.* **2010**, *133*, 144506/1.

(104) Greene, B. I.; Millard, R. R. *Phys. Rev. Lett.* **1985**, *55*, 1331.

(105) Burdett, J.; Gosztola, D.; Bardeen, C. J. *Supplementary Material Document Number* **2011**.

(106) Smith, A. W.; Weiss, C. *Chem. Phys. Lett.* **1972**, *14*, 507.

(107) Wappelt, A.; Bergmann, A.; Napiwotzki, A.; Eichler, H. J.; Jupner, H. J.; Kummrow, A.; Lau, A.; Woggon, S. *J. Appl. Phys.* **1995**, *78*, 5192.

(108) Camposeo, A.; Polo, M.; Tavazzi, S.; Silvestri, L.; Spearman, P.; Cingolani, R.; Pisignano, D. *Phys. Rev. B* **2010**, *81*, 033306/1.

(109) Jankowiak, R.; Kalinowski, J.; Konys, M.; Buchert, J. *Chem. Phys. Lett.* **1979**, *65*, 549.

(110) Sondermann, U.; Kutoglu, A.; Bassler, H. *J. Phys. Chem.* **1985**, *89*, 1735.

(111) Venuti, E.; Valle, R. G. D.; Farina, L.; Brillante, A.; Masino, M.; Girlando, A. *Phys. Rev. B* **2004**, *70*, 104106/1.

(112) Spano, F. C. *Ann. Rev. Phys. Chem.* **2006**, *57*, 217.

(113) Piryatinskii, Y. P.; Kurik, M. V. *Mol. Mater.* **1992**, *1*, 43.

(114) Knutson, J. R.; Beechem, J. M.; Brand, L. *Chem. Phys. Lett.* **1983**, *102*, 501.

(115) Lofroth, J. E. *J. Phys. Chem.* **1986**, *90*, 1160.

(116) Vaubel, G.; Baessler, H. *Mol. Cryst. Liq. Cryst.* **1971**, *15*, 15.

(117) Swenberg, C. E.; Geacintov, N. E. In *Organic Molecular Photophysics*; Birks, J. B., Ed.; Wiley & Sons: Bristol, 1973; Vol. 1, p 489.

(118) Tomkiewicz, Y.; Groff, R. P.; Avakian, P. *J. Chem. Phys.* **1971**, *54*, 4504.

(119) Riemer, W.; Hardy, J. V. *Phys. Stat. Sol. A* **1972**, *14*, 473.

(120) Mizuno, K.; Matsui, A.; Sloan, G. J. *J. Phys. Soc. Jap.* **1984**, *53*, 2799.

(121) Mizuno, K.; Matsui, A.; Sloan, G. J. *Chem. Phys.* **1989**, *131*, 423.

(122) Chandross, E. A.; Ferguson, J.; McRae, E. J. *J. Chem. Phys.* **1966**, *45*, 3546.

(123) Merrifield, R. E. *J. Chem. Phys.* **1968**, *48*, 4318.

(124) Johnson, R. C.; Merrifield, R. E. *Phys. Rev. B* **1970**, *1*, 896.

(125) Suna, A. *Phys. Rev. B* **1970**, *1*, 1716.

(126) Smith, M. B.; Michl, J. *Chem. Rev.* **2010**, *110*, 6891.

(127) Blinov, L. M.; Kirichenko, N. A. *Opt. Spect.* **1974**, *37*, 513.

(128) Sebastian, L.; Weiser, G.; Bassler, H. *Chem. Phys.* **1981**, *61*, 125.

(129) Jadhav, P. J.; Mohanty, A.; Sussman, J.; Lee, J.; Baldo, M. A. *Nano Lett.* **2011**, *11*, 1495.

(130) Marciniak, H.; Pugliesi, I.; Nickel, B.; Lochbrunner, S. *Phys. Rev. B* **2009**, *79*, 235318/1.

(131) Burdett, J. J.; Gosztola, D.; Bardeen, C. J. *J. Chem. Phys.* **2011**, *135*, 214508/1.

(132) McGlynn, S. P. *Molecular spectroscopy of the triplet state*; Prentice-Hall: Englewood Cliffs, NJ, 1969.

(133) Casperson, L. W. *Phys. Rev. A* **1997**, *55*, 3073.

(134) Bardeen, C. J.; Cao, J.; Brown, F. L. H.; Wilson, K. R. *Chem. Phys. Lett.* **1999**, *302*, 405.

(135) Chan, W. L.; Ligges, M.; Jailaubekov, A.; Kaake, L.; Miaja-Avila, L.; Zhu, X. Y. *Science* **2011**, *334*, 1541.

(136) Schmidt, J.; Waals, J. H. v. d. In *Time domain electron spin resonance*; Kevan, L., Schwartz, R. N., Eds.; Wiley: New York, 1979.

(137) *Chemically induced magnetic polarization*; Lepley, A. R.; Closs, G. L., Eds.; Wiley: New York, 1973.

(138) Lopez-Delgado, R.; Miehe, J. A.; Sipp, B. *Opt. Comm.* **1976**, *19*, 79.

(139) Benk, H.; Sixl, H. *Molec. Phys.* **1981**, *42*, 779.

(140) Abragam, A. *Principles of nuclear magnetism*; Clarendon: Oxford, 1961.

(141) Sternlicht, H.; McConnell, H. M. *J. Chem. Phys.* **1961**, *35*, 1793.

(142) Verhoeven, J. W. *J. Photochem. Photobio. C* **2006**, *7*, 40.

(143) Shaakov, S.; Galili, T.; Stavitski, E.; Levanon, H.; Lukas, A.; Wasielewski, M. R. *J. Am. Chem. Soc.* **2003**, *125*, 6563.

(144) Poluektov, O. G.; Paschenko, S. V.; Utschig, L. M. *Phys. Chem. Chem. Phys.* **2009**, *11*, 6750.

APPENDIX I

A1.1 Matlab code used to extract decays from time resolved photoluminescence

```
function y=timewindow(data, w_ini, w_window)
% sum the time axis element and return summed wavelength intensity
matrix
% column is wavelength, row is time sequence
% additionally smooth wavelength axis with box smoothing
b=sum(data(:,w_ini:w_ini + w_window),2);

y = b;
```

A1.2 Matlab code used to extract spectra from time resolved photoluminescence

```
function y=swindow(data, t_ini, t_window)
 % sum the wavelength axis element and return summed time intensity
matrix
% column is wavelength, row is time sequence
% additionally smooth time axis with box smoothing

b=sum(data(t_ini:t_ini + t_window,:))';

y = b;
```

A1.3 Matlab code used to correct the slope in the streak camera

```
function y = SCshift2(SCdata,b)
%
% This program shifts an array by a slope=b to line up the time=0
points
% in a SC 2D data set
% b can be positive or negative
%
% loop over array and shift elements according to line with slope b
for k=1:640
    if b >= 0
    shift=round(b*k);
    SCdata2(shift+1:480,k)=SCdata(1:480-shift,k);
    SCdata2(1:shift-1,k)=0;
    else
    shift=round(-b*k);
    SCdata2(1:480-shift,k)=SCdata(shift+1:480,k);
    SCdata2(480-shift:480)=0;
    end
end
%plot original data and shifted data .  Note that shifted data will
%have ends with zeros filled in, in order to emphasize that these are
"fake"
```

```
%points and cannot be used for fitting, etc.
figure(1);
image(SCdata)
figure(2);
image(SCdata2)
y=SCdata2;
end
```

A1.4 Simple Matlab program used to simulate fluorescence decays in Chapter 3

```
function exexdecay(n0,kfl,kee)
%
% calculates simple exciton exciton annihilation decay
%n0=initial density, in nm^-3
%kfl = fluorescence decay rate, ps^-1
%kee = ex ex annihilation rate, nm^3ps^-1
%
global time eedecn eedec
time=[0:300];
eedec=(-kee/kfl+(1/n0+kee/kfl)*exp(kfl*time)).^-1;
eedeca=eedec/max(eedec);
eedecn=eedeca';
figure(1);
plot(time,exp(-kfl*time))
hold
plot(time,eedecn,'r')
hold off
```

A1.5 Second Matlab program created to simulate fluorescence decays in Chapter 4

```
function y =
population3(kr,kic,kisc,ktrip,kee,kfiss,kTT,kTS,density,tfinal)
%
% This function calls the ODE routine "three2" to solve 2 coupled
% differential equations that describe the evolution of the S1 and T1
% populations in tetracene solids.  all units are in ns^-1 and um^3.
This program only
% calculates dynamics after an instantaneous pulse.
%
% kr = radiative rate
% kic = nonradiative internal conversion rate
% ktrip = triplet decay rate
% kisc = intersystem crossing rate
% fex = fraction of ground state placed in singlet S1 state
% kfiss = singlet fission rate; S1 -> 2 T1
% kTS = triplet fusion rate; 2 T1 -> S1
% kTT = triplet fusion rate; 2 T1 -> T1
% kee = singlet-singlet exciton annilation rate; 2 S1 -> S1 + S0
% density = initial density of excitations, nm^-3
%
global M1 M2 M3 flsig time
%
```

```
kfl=kr+kic+kisc+kfiss;
%
M1= [-kfl                0
    kisc+2*kfiss     -ktrip];
M2=[-kee                 kTS
    0                    -kTT-2*kTS];
Npopinit=[ density
        0];
%
%Note the time step is set to 2 ps = 0.002 ns
[t,Npop]=ode45('three2',[0:.002:tfinal],Npopinit);
figure(1);
plot(t,Npop(:,1),'b');%singlet
hold;
plot(t,Npop(:,2),'r');%triplet
hold off;
figure(2);
plot(t,log(Npop(:,1)/max(Npop(:,1))));% log of singlet decay
figure(3);
plot(t,log(Npop(:,2)));% log of triplet decay
%print out asymptotic values of NS0,NS1,NT1
dummy=flipud(Npop);
dummy(1,:)
time=[0:.002:tfinal]; %time axis
flsig=Npop(:,1);%observed fluorescence signal
```

A1.6 Subroutine called by population3 program

```
function F = three2(t,Npop)
%
% This function defines a differential equation that needs to be solved
for a
% two component population matrix Npop=[NS1 NT1]
% M1 and M2 are 2x2 matrices defined in the program that calls "three2"

global M1 M2
%
F=M1*Npop+M2*Npop.^2;
```

A1.7 Matlab code used to simulate the quantum beats in the delayed fluorescence

```
function y =
FourS1c(k12,k13,k14,k21,k31,k41,kfl,T2tt,ktrip,Dstar,Estar,tfinal)
%
% This function calculates the time evolution of a 3 state system where
% state 1 is coupled to states 2,3 and 4.  State 1 is assumed to have
an
% energy of 0.  The dephasing between states 1 and 2/3/4 is assumed to
be
% very fast, so 12,13 and 14 coherences can be eliminated from the
problem.
% The triplet state coherences decay due to T2tt, and ktrip gives
```

```
% population relaxation out of triplet states.
%
% k12 = transition rate 1-->2
% k13 = transition rate 1-->3
% k14 = transition rate 1-->4
% k21 = transition rate 2-->1
% k31 = transition rate 3-->1
% k41 = transition rate 4-->1
% Dstar,Estar are triplet parameters of crystal pair, in ns-1
% e2,e3,e4 =frequencies of triplet energy levels 2,3,4 in ns-1
% T2tt = pure dephasing between triplet levels
% kfl = fluorescence decay time due to non-fission events
% ktrip = population relaxation rate from triplet levels (22,33,44
density
% matrix elements)
% note that the rates are asymmetric -- the forward and reverse rates
are
% NOT equal
%
%
start=200; %point to start taking data for FFT of oscillations
global MM tcalc sigcalc freqcalcA speccalcA rhod
% calculate energies of xx, yy and zz triplet states (levels 2,3,4)
e2=2*pi*2*(Dstar/3-Estar); %Exx
e3=2*pi*2*(Dstar/3+Estar); %Eyy
e4=2*pi*2*(-2*Dstar/3);    %Ezz
%define overall dephasing rates
deph23=1/T2tt + k21/2 + k31/2 + ktrip/2;
deph24=1/T2tt + k21/2 + k41/2 + ktrip/2;
deph34=1/T2tt + k31/2 + k41/2 + ktrip/2;
%
%fill 10x10 matrix 11,22,33,44,23,32,24,42,34,43 density matrix
elements
MM=[-(k12+k13+k14+kfl)  k21                  k31                  k41
sqrt(k21*k31)       sqrt(k21*k31)       sqrt(k21*k41)
sqrt(k21*k41)       sqrt(k31*k41)       sqrt(k31*k41)
    k12                 -k21-ktrip          0                    0
-sqrt(k21*k31)/2    -sqrt(k21*k31)/2    -sqrt(k21*k41)/2    -
sqrt(k21*k41)/2    0                   0
    k13                 0                   -k31-ktrip          0
-sqrt(k21*k31)/2    -sqrt(k21*k31)/2    0                   0
-sqrt(k31*k41)/2    -sqrt(k31*k41)/2
    k14                 0                   0                   -k41-
ktrip        0                   0                   -sqrt(k21*k41)/2
-sqrt(k21*k41)/2    -sqrt(k31*k41)/2    -sqrt(k31*k41)/2
    sqrt(k12*k13)       -sqrt(k21*k31)/2    -sqrt(k21*k31)/2    0
+i*(e3-e2)-deph23   0                   -sqrt(k31*k41)/2    0
0                   -sqrt(k21*k41)/2
    sqrt(k12*k13)       -sqrt(k21*k31)/2    -sqrt(k21*k31)/2    0
0                   -i*(e3-e2)-deph23   0                   -
sqrt(k31*k41)/2    -sqrt(k21*k41)/2    0
    sqrt(k12*k14)       -sqrt(k21*k41)/2    0                   -
sqrt(k21*k41)/2  -sqrt(k31*k41)/2    0                   +i*(e4-e2)-
deph24    0                 -sqrt(k21*k31)/2    0
```

```
    sqrt(k12*k14)       -sqrt(k21*k41)/2    0                   -
sqrt(k21*k41)/2  0                   -sqrt(k31*k41)/2    0
-i*(e4-e2)-deph24   0                   -sqrt(k21*k31)/2
    sqrt(k13*k14)       0                   -sqrt(k31*k41)/2    -
sqrt(k31*k41)/2  0                   -sqrt(k21*k41)/2    -
sqrt(k21*k31)/2    0                  +i*(e4-e3)-deph34   0
    sqrt(k13*k14)       0                   -sqrt(k31*k41)/2    -
sqrt(k31*k41)/2  -sqrt(k21*k41)/2    0                   0
-sqrt(k21*k31)/2    0                   +i*(e4-e3)-deph34
    ];
%
% we will solve this 2 different ways
% first, we call the ODE solver
rhoinit=[   1
            0
            0
            0
            0
            0
            0
            0
            0
            0];
[t,rhod]=ode45('execute1',[0:.02:tfinal],rhoinit);
%
%
tcalc=t;
sigcalc=abs(rhod(:,1));
%subtract off background for the fourier transform
sigcalcA=sigcalc-mean(sigcalc(900:1001));
sigcalcB=sigcalcA(start:1001);
tcalcA=tcalc(start:1001);
speccalcA=abs(fft(sigcalcB,1024)).^2;
freqcalcA=1/.02*1/1024*[0:1023];
%
figure(1);
plot(t,rhod(:,1));
hold;
plot(t,rhod(:,2),'r');
plot(t,rhod(:,3),'g');
plot(t,rhod(:,4),'m');
hold off;
figure(2);
plot(t,log(rhod(:,1)));
figure(3);
plot(freqcalcA(1:100),speccalcA(1:100));
```

A1.8 Subroutine called by FourS1c to solve the differential equations

```
function F = execute1(t,rhod)
%
% This function defines a differential equation that needs to be solved
for a
```

```
% N component population matrix.
% MM is a NxN matrix defined in the program that calls "execute1"

global MM
%
F=MM*rhod;
```

APPENDIX II

Figure A2.1 Global Fits and residuals on photoluminescence decays in a 1 ns window, which Figure 7 is made from. Short time decays were held constant while the longer lifetime decay was allowed to vary.

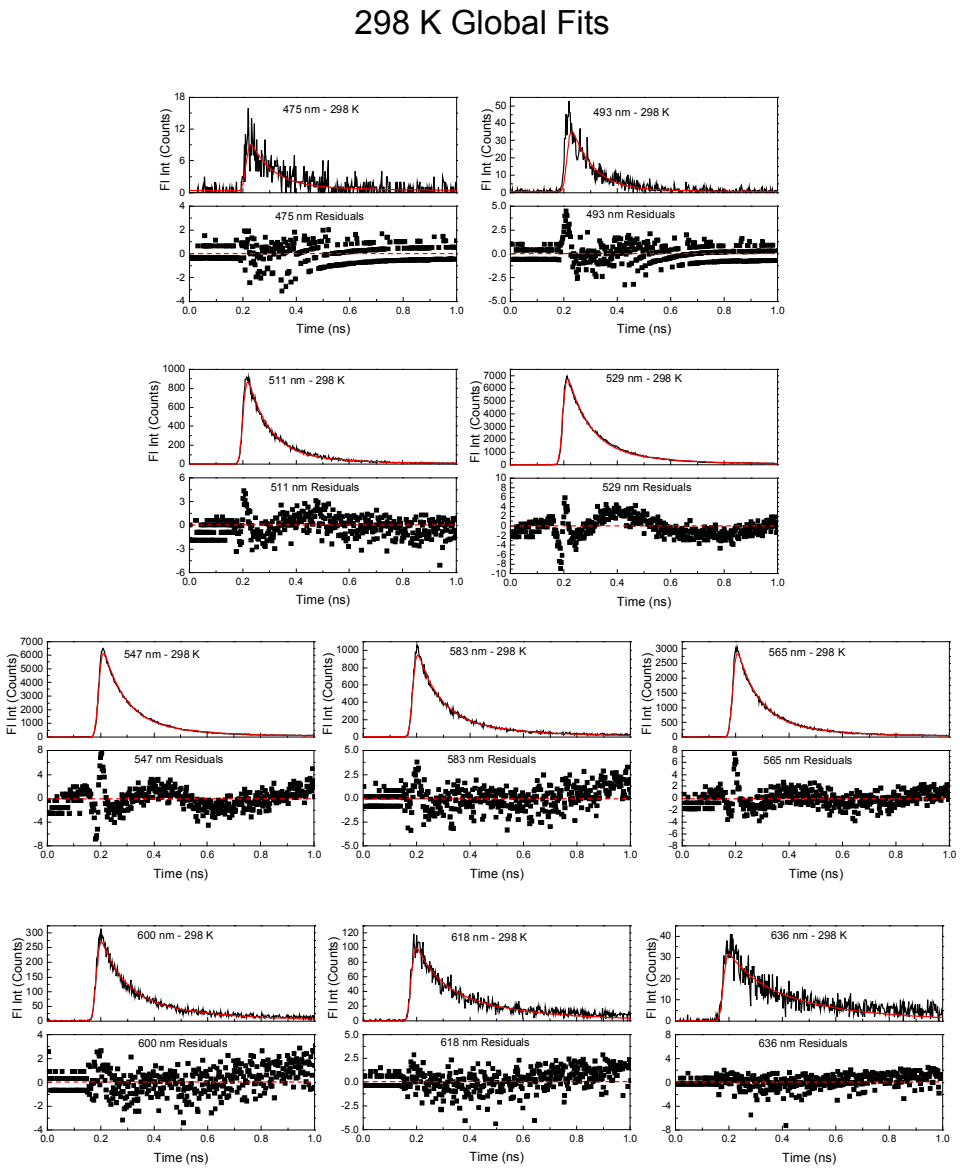

77 K Global Fits

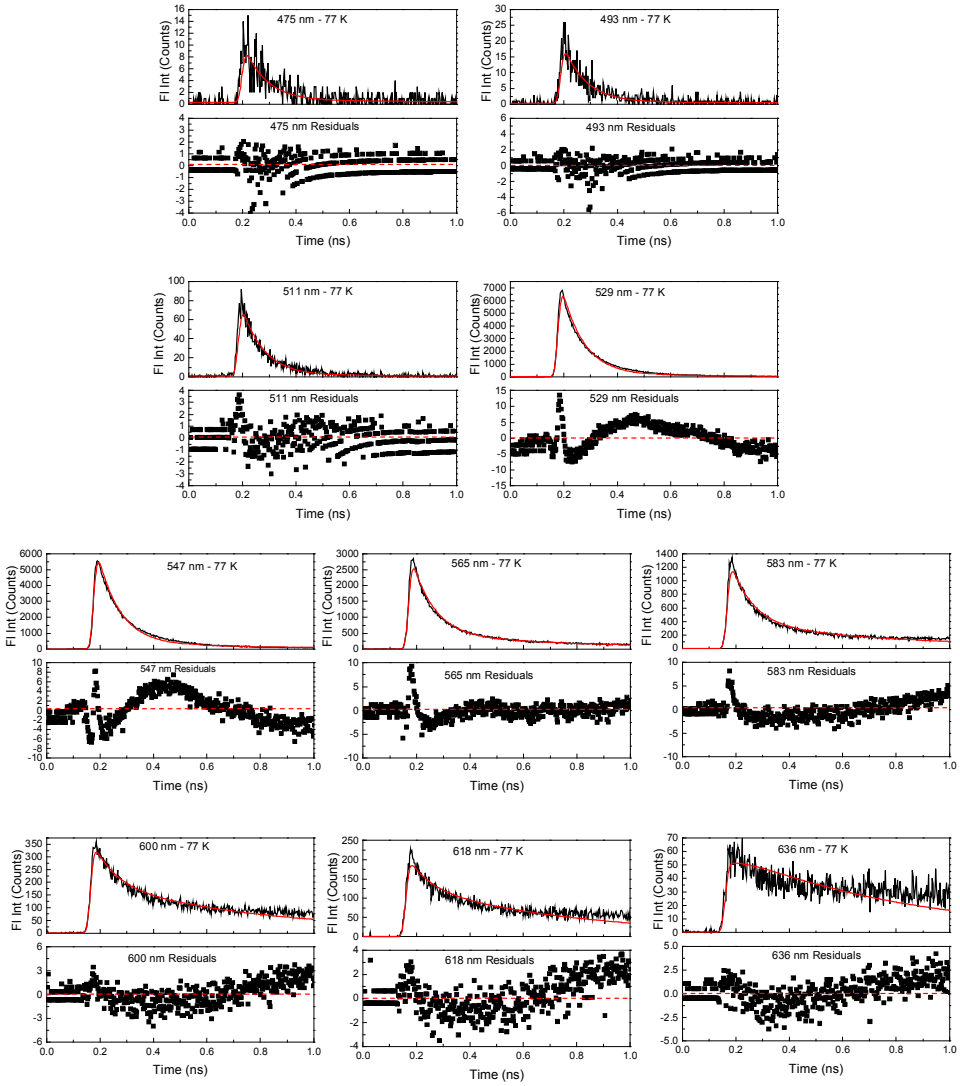

4 K Global Fits